Combining Stationary Ocean Models and Mean Dynamic Topography Data

DISSERTATION
zur
Erlangung des Grades
Doktor der Naturwissenschaften
– Dr. rer. nat. –

dem Fachbereich I (Physik/Elektrotechnik) der

vorgelegt von

Grit Freiwald

April 2012

1. Gutachter: Prof. Dr. Peter Lemke
2. Gutachter: Prof. Dr. Thomas Jung

Alfred-Wegener-Institut für Polar- und Meeresforschung

Meinem Papa.

Abstract

In this study, a new estimate for the Mean Dynamic Topography (MDT) and its error description is analysed in terms of its impact on the performance of ocean models. This MDT estimate is primarily designed for the combination with ocean models. For the first time, a full error covariance matrix is available whose inverse can readily be used as weighting matrix in the optimization.

Two different steady-state inverse ocean models are analysed in terms of their response to the new MDT data set. The 2D model FEMSECT is a section model which is applied to the SR3 hydrographic section in the Southern Ocean in this study. The 3D model IFEOM is a finite element model for the North Atlantic. The output of each of these ocean models in turn provides a combined satellite-ocean model MDT. This combined MDT contains information from satellites, physical principles, hydrographic atlas data and the prior knowledge that is assumed for the model setup.

This study investigates whether the inverse ocean models benefit from the new MDT data set and its error covariance. It is verified that the resulting combined MDT is more realistic than both the pure model MDT and the pure observational MDT. It is examined whether oceanographic features such as the ocean current structure, the overturning circulation and heat transports are also improved by the assimilated MDT data set. Special focus is given to the MDT error covariance estimate as it is crucial in the optimization. Its impact on the result is studied in detail.

In the FEMSECT model optimization, three commonly known problems were identified, two of which could be solved by the application of Kimura's method for estimating surface velocities from sea ice drift data. The issue of resolution of the satellite geoid data could not be solved due to lack of small-scale data for the model region.

A series of solutions was computed with the IFEOM model. The assimilation of the new combined MDT data improved the circulation estimate considerably. More details of the ocean currents are revealed and increased velocities and temperature gradients appear that had not been visible in previous model runs. The formal error estimate for the new MDT data set is too small to be utilized by the IFEOM model to its full extent of possible accuracy. Therefore it must be downweighted in the optimization process. Different downweighting approaches for extracting the most suitable amount of information from the data are proposed. It was found that the MDT error covariances are of overall importance for smoothness and for the mean diagonal weight in the optimization. It was shown that a decomposition of the covariance matrix and subsequent reinterpretation of the geodetic normal equations and the cost function is possible. The resulting optimized model solution is the best IFEOM solution in terms of selected oceanographic features.

Most improvements regarding the IFEOM model output were observed by refining the omission error model and by increasing the model resolution. It is suggested to further explore the MDT error covariance structure and to use more complex ocean models to fully exploit the value of the new space-borne data.

Contents

Acronyms

AABW Antarctic Bottom Water

ACC Antarctic Circumpolar Current

AMOC Atlantic Meridional Overturning Circulation

BFGS algorithm Broyden-Fletcher-Goldfarb-Shanno algorithm

CLS09 MDT CNES-CLS09_v1.0 MDT, Rio et al. (2011)

DFG Deutsche Forschungsgemeinschaft

DVC Deep velocity constraint

ECCO Estimating the Circulation and Climate of the Ocean

ECCO-GODAE ECCO - Global Ocean Data Assimilation Experiment

EGM08 Earth Gravitational Model 2008, Pavlis et al. (2008)

EGM96 Earth Gravitational Model 1996, Lemoine et al. (1997)

FEMSECT Finite Element Method Section Model

GECCO German ECCO

GOCE Gravity field and steady-state Ocean Circulation Explorer

GRACE Gravity Recovery and Climate Experiment

IFEOM Inverse Finite Element Ocean Model

INTERMOD Consistent integration of global gravity field information into Earth process models

ITG Institute for Theoretical Geodesy

MDT Mean Dynamic Topography η

MME Maximum model entropy

MMME Minimum model MDT error

MOC Meridional Overturning Circulation

MPV Minimum penalty variance

NADW North Atlantic Deep Water

NCEP National Centers for Environmental Prediction

OGCM Ocean General Circulation Model

PF Polar front

PSU Practical Salinity Unit, as derived from the Practical Salinity Scale (PSS-78)

Rifugio Rigorous Fusion of Gravity Field into Stationary Ocean Models

RIO05 MDT Predecessor of CLS09 MDT, Rio and Hernandez (2004)

SAF Subantarctic front

SR3 section WOCE Southern Ocean Repeat section 3

Sv Sverdrup

WOCE World Ocean Circulation Experiment

Model solutions

Reference Original FEMSECT without any MDT information, see section 3.1

EGM96 FEMSECT using EGM96 error covariance information, see section 3.2.1

Transition FEMSECT with error covariance including transition zone, see section 3.2.1

CompleteITG FEMSECT with error covariance including omission error model, see section 3.2.1

CLS09 FEMSECT incorporating CLS09 MDT, see section 3.2.1

SAT FEMSECT incorporating only satellite MDT information, see section 3.2.1

Rifugio MDT MDT computed as described in chapter 2.4, see also 2.4.4

Rif01 IFEOM using special omission error model, see section 4.2.3 and table 4.1

Rif02 IFEOM using another omission error model, see section 4.2.3 and table 4.1

Rif03 Rif02 but with higher resolution ($1 \times 1^\circ$ grid), see section 4.2.4 and table 4.1

Rif04 Rif03 but including 2 months of GOCE data, see section 4.2.5 and table 4.1

Rif05 Rif03 but including 7 months of GOCE data, see section 4.2.5 and table 4.1

RifCov1 Rif05, but with weighting matrix inv(diag(inv($\mathbb{P}$))) instead of $\mathbb{P}$, see section 4.3.2.1 and table 4.6

RifCov2 Rif05, but with weighting matrix diag($\mathbb{P}$), see section 4.3.2.1 and table 4.6

RifCov3 Rif05, but with weighting matrix $\mathbb{D}$, see section 4.3.2.3 and table 4.6

RifCov3-7 same as RifCov3 (weighting factor $\alpha = 7$), used for better distinction from RifCov3-45

RifCov3-45 RifCov3 with weighting factor $\alpha = 45$

Introduction

The world ocean is an important part of the Earth's climate system. For understanding and predicting this system, understanding the large-scale ocean circulation is essential (Olbers, 1988). Our current knowledge of the ocean circulation is based on observations and on modelling efforts.

On the one hand, in-situ observations are sparse, and even with dedicated efforts such as the World Ocean Circulation Experiment (WOCE), the ocean is still severely undersampled (Wunsch and Heimbach, 2009). Satellite observations provide additional valuable information. However, these observations are integrated over a more or less widespread "footprint" of the satellites (see e.g. Robinson, 2010) and are limited to the surface of the ocean (except when measuring gravity). In summary, the current data coverage is not sufficient to provide comprehensive understanding of the complex ocean dynamics.

On the other hand, numerical ocean models are also used towards understanding the ocean circulation. Although these models are continuously improved, also with the help of advances in computer technology, a number of physical processes are still not resolved by them and need to be parametrized. The large amount of required simplifying assumptions may render a numerical ocean model far from a reliable representation of the real ocean.

A potential way out of this dilemma is offered by inverse methods, see e.g. Wunsch (1996). These approaches try to combine numerical models and observations. Therefore they account for the information of the raw data and still benefit from the dynamic consistency of the model. A compromise between data and model is sought, guided by a priori information on data and model errors and, possibly, additional constraints.

Inverse models of the ocean strongly depend on observational data which are generally sparse (Anderson et al., 1996 and Malanotte-Rizzoli and Tziperman, 1996). However, in recent years, the amount of available satellite data has increased tremendously (Malanotte-Rizzoli and Tziperman, 1996 and Rio, 2010) and together with it the wish to combine these data sets with ocean models. For physical ocean modelling, the Mean Dynamic Topography (MDT) is of particular interest (e.g. Vossepoel, 2007 and Farrell et al., 2012) as it is directly linked to the surface velocity in the ocean (Pedlosky, 1987). Therefore using satellite MDT data offers a great possibility for ocean modelers wanting to improve the accuracy and reliability of their ocean models by velocity information.

However, obtaining MDT information from satellite data is not straightforward (Rio, 2010 and Bingham et al., 2008). Two fundamentally different observations are needed: Altimetry data and geoid data. These are not only provided by different satellites, but also carry signals on different spatial scales and are usually represented by different basis functions. This circumstance causes several problems, among those the filtering that must be introduced in order to make the different data sets consistent with each other. By filtering altimetry and geoid data, an unknown and to some extent arbitrary amount of information is lost (Bingham et al., 2008, 2011 and Knudsen et al., 2011).

In this study, a new estimate for the MDT and its error description (Becker et al., 2012) is analysed in terms of its impact on the performance of ocean models. This MDT estimate was developed and computed at the Institute of Geodesy and Geoinformation (IGG) at the University of Bonn and was made available to the AWI within the framework of this project. The MDT estimate is primarily designed for the combination with ocean models e.g. by least-squares minimization. For the first time, an error covariance is provided whose inverse can readily be used as weighting matrix in the optimization.

The only other data set used in the optimization is the climatology of Gouretski and Koltermann (2004). It provides temperature and salinity data for the North Atlantic model region. The `CNES-CLS09_v1.1` MDT (Rio et al., 2011) was used for comparison and validation of the inverse ocean model runs.

Two different steady-state inverse ocean models are analysed in terms of their response to the new MDT data set. The 2D model FEMSECT (Losch et al., 2005) is a section model which is applied in this study to the SR3 hydrographic section in the Southern Ocean. The 3D model IFEOM (Sidorenko, 2004) is a finite element model for the North Atlantic. The output of each of these ocean models in turn provides a combined satellite-ocean model MDT. This MDT combines information from satellites, physical principles, hydrographic atlas data and the prior knowledge that is assumed for the model setup.

This study investigates whether the inverse ocean models benefit from the new MDT data set and its error covariance information. The resulting combined MDT is expected to be more realistic than both the pure ocean model MDT and the pure observational MDT, an assumption that has to be verified. The oceanographic interest concentrates on circulation features such as the current structure, the Meridional Overturning Circulation and meridional heat transports. It is studied whether these features are also improved by the assimilated new MDT data set. The focus is on the MDT error covariance estimate as it is crucial in the optimization. Its impact on the results is analysed in detail.

The relevance of this study and some background about ocean modelling are provided in the first chapter. The second chapter gives an introduction to MDT modelling and introduces the new MDT data set. Afterwards, in chapters three and four, the new MDT is combined with the ocean models FEMSECT and IFEOM, respectively. A summary of the findings, conclusions and an outlook complete this study.

How inappropriate to call this planet Earth when it is quite clearly Ocean.

Arthur C. Clarke

Chapter 1

Ocean Circulation and Ocean Modelling

This chapter intends to give an overview of the fundamentals of physical oceanography that are relevant for this work. The circulation in the ocean regions of interest is described and an introduction to inverse ocean models is provided.

1.1 Introduction: The global ocean

Climate change is taking place on our Earth and is going to affect our lives and those of our successors (Parry et al., 2007). Although this fact is well known and accepted by now, some of the ongoing oceanic processes are still poorly understood (see e.g. Wunsch, 2001; Stewart, 2008; Rahmstorf, 2003). This is due to the complexity of the system Earth in which atmosphere, hydrosphere, lithosphere and biosphere all are important but intrinsically different subsystems. With 97%, the oceans represent the overwhelming fraction of the hydrosphere and they cover 71% of the Earth's surface (Gleick, 1996; Stewart, 2008).

The oceans are responsible for a large part of the transport of heat from low to high latitudes. Although the ocean circulation is much slower than the atmospheric circulation, the amount of heat transported polewards by both systems is comparable due to the very high heat capacity of water (Bryden and Imawaki, 2001). This has a large impact on regional climates, the most remarkable example being Northern Europe influenced by the Gulf Stream system. The latter is only one component of the "Great Ocean Conveyor Belt" (Broecker, 1991), a metaphor sketching a much simplified ocean circulation scheme, shown in figure 1.1. It shows the relatively warm large-scale surface circulation in red and the relatively cold and deep circulation in blue. In the Northern North Atlantic, surface water is transformed into deep water (see also next section). The main connection between the Atlantic, Indic and Pacific Ocean is via the Southern Ocean circumpolar flow (see also next section). It may take up to 1600 years for a water parcel to travel the conveyor once (Primeau, 2005). This sluggish movement leads to long response time scales of the ocean affecting climate change and also delaying mitigation policies (Irvine et al., 2012).

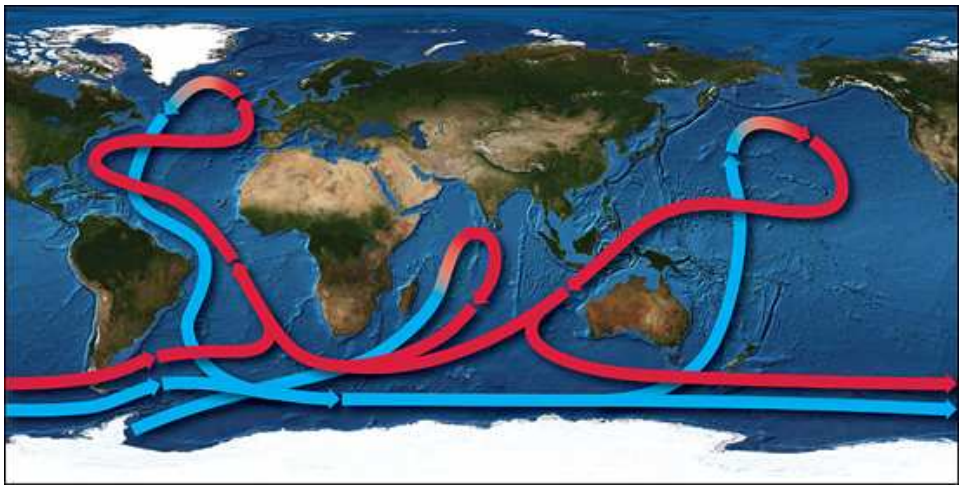

Fig. 1.1: Great Ocean Conveyor Belt. Illustration by Jack Cook, Woods Hole Oceanographic Institution.

The ocean by itself is damping climate change by the uptake of excess (anthropogenic) CO_2. A biological[1] and a physical pump are transporting carbon into the ocean interior and therefore acting as a buffer for greenhouse gas emissions. The main regions where this takes place are the North Atlantic (see e.g. Sabine et al., 2004) and the Southern Ocean (Caldeira and Duffy, 2000). Whereas the largest CO_2 fluxes into the ocean occur in the Southern Ocean region, the CO_2 is not stored there but transported northwards along isopycnals. In the North Atlantic, however, the anthropogenic CO_2 is convected deeply through the water column such that the highest column inventories are found here (Caldeira and Duffy, 2000).

These are only some of the climate related reasons why the oceans are important for humans. Other reasons are the food we get from the ocean and the use of the ocean in terms of transportation, use of the coastal regions, geological exploitation of the seabed and use for recreation. For these reasons, we take the effort and try to contribute to the understanding of the ocean circulation. In the following sections, the reader is introduced to the regions of interest for this study, the North Atlantic Ocean and the Southern Ocean.

[1]For natural carbon only. The biological pump is assumed not to be affected by anthropogenic CO_2 (Caldeira and Duffy, 2000).

The Pacific is an ocean ... the Atlantic is a bloody bowling alley.

John Edmond

1.2 Regional aspects

Regional details are important for understanding the ocean circulation. For running and evaluating inverse ocean models, a priori information about the circulation is also helpful. Therefore this section provides an introduction to the regions of interest in this work, the North Atlantic and the Southern Ocean.

1.2.1 North Atlantic Ocean

Due to its location between Europe and North America, the North Atlantic is the best explored of all oceans (Tomczak and Godfrey, 1994). As illustrated in figure 1.2, the low latitudes are dominated by the Subtropical Gyre with a broad and slow Eastern return current and the prominent western intensification, the Gulf Stream. This narrow and deep-reaching current is meandering and shedding eddies permanently (Tomczak and Godfrey, 1994). A large persistent feature was discovered by Mann (1967). The Mann Eddy is located in the vicinity of 41°N, 42°W, a branching point of the current system (not indicated on figure 1.2).

The Gulf Stream separates from the American coastline near Cape Hatteras and eventually splits up into the North Atlantic Current and the Azores Current east of 50°W (Tomczak and Godfrey, 1994). The latter eventually closes the large Subtropical Gyre, and the former represents the eastern part of the Subpolar Gyre. This heart-shaped cyclonic circulation pattern near Greenland comprises also the East Greenland Current, the West Greenland Current and a southward western boundary current, the Labrador Current (Treguier et al., 2005).

The presence of the Labrador Current forces the North Atlantic Current to change direction from northwards to further eastwards (Krauss et al., 1987). The extension of the North Atlantic Current, named North Atlantic Drift Current, continues its way northeastwards, and a fraction of water manages to cross the system of submarine ridges between Iceland and Scotland. The resulting Norwegian Current is part of a cyclonic circulation pattern in the Nordic Seas eventually forming the East Greenland Current (Hansen and Østerhus, 2000).

The circulation scheme of the Great Ocean Conveyor Belt described above is influenced by formation of very dense water masses (Wunsch, 2002). This happens only in a few places in the world, two of which are in the Northern North Atlantic. It is in the Labrador Sea and in the Nordic or GIN (Greenland-Iceland-Norwegian) Seas where conditions promote the production of very cold and salty and therefore very dense water. As these water masses sink down, they spread southwards into the North Atlantic (Ganachaud and Wunsch, 2000), representing the two main contributors to the formation of North Atlantic Deep Water (NADW) (Kuhlbrodt et al., 2007). An enhanced surface flow eventually closes the scheme of the so-called (Atlantic) Meridional Overturning Circulation, usually abbreviated as (A)MOC, see figure 1.3.

In chapter 4, the ocean model IFEOM will be applied to the North Atlantic to investigate its circulation patterns and Meridional Overturning Circulation (MOC).

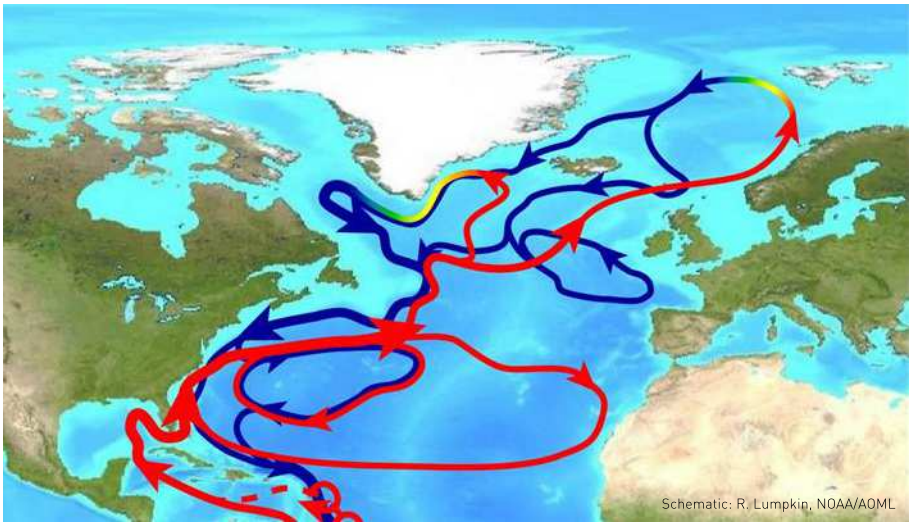

Fig. 1.2: Schematic of the North Atlantic circulation. Detail of an illustration by Rick Lumpkin, NOAA/AOML[2].

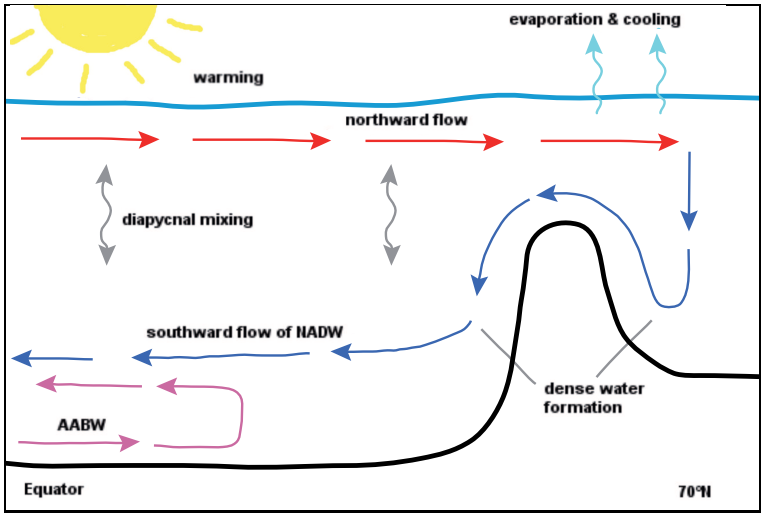

Fig. 1.3: Schematic of Atlantic Meridional Overturning Circulation (AMOC), after Kuhlbrodt et al. (2007) and Natural Environment Research Council (2007, `http://www.noc.soton.ac.uk/rapid/rw/images/diagrams/moc_revised_strong.jpg`), NADW: North Atlantic Deep Water, AABW: AntArctic Bottom Water

[2]The illustration was published on `http://www.bio.gc.ca/science/research-recherche/ocean/variability-variabilite/labrador/images/AMOC-shematic.jpg` by the Government of Canada. This reproduction has not been produced in affiliation with, or with the endorsement of the Government of Canada.

1.2.2 Southern Ocean

In the southern hemisphere, deep water formation happens in various locations around the Antarctic continent (Rintoul et al., 2001). The resulting Antarctic Bottom Water (AABW) is very cold and relatively fresh compared to the Nord Atlantic Deep Water. Different varieties of AABW exist, all of which contribute to the densest waters in the main basins of the global ocean (Johnson, 2008). The so formed water masses play an important role in the global ocean circulation (Rintoul et al., 2001).

The southern parts of the "official"[3] oceans, the Atlantic, the Indian and the Pacific ocean, are usually summarized by the expression "Southern Ocean". This region of the world ocean is unique in many aspects (Tomczak and Godfrey, 1994). The circulation can continue all around the globe as indicated in figures 1.1 and 1.4. This circumpolar flow is called Antarctic Circumpolar Current (ACC) and is an important feature of the ocean's circulation (Stewart, 2008).

The Antarctic Circumpolar Current is driven by strong westerly winds (in tight combination with buoyancy forcing). The winds reach their maximum speed near 50°S and constantly transfer momentum to the ACC. This is balanced by form drag at the bottom topography, in particular at Drake passage (Munk and Palmen, 1951; Olbers, 1998). However, also in other areas, bottom topography strongly influences the flow and its variability (Nowlin Jr. and Klinck, 1986).

The ACC mixes water from the Atlantic, Pacific and Indian Ocean and redistributes it back to each ocean (see figure 1.4). Three fronts are continuous around Antarctica: the Subantarctic Front, the Polar Front and the Southern ACC Front (Orsi et al., 1995). On their way around Antarctica, three "chokepoints" have to be passed (see also figure 1.1): Drake Passage, the section between the Cape of Good Hope and Antarctica, also referred to as "Greenwich meridian" section, and the North-South section between Tasmania and Antarctica. As these chokepoints represent natural fixed boundaries for the ACC, transports of volume, heat and biogeochemical tracers across these three sections can be estimated without the subjective determination of a northern end point of an arbitrary longitudinal section.

The transports within the ACC are large, because the currents are wide and extend to the bottom, with typical current speeds of $10\,\mathrm{cm\,s^{-1}}$ to $50\,\mathrm{cm\,s^{-1}}$ (Stewart, 2008). For example Whitworth and Petersen (1985) estimated the average volume transport through Drake passage to be $125\pm11\,\mathrm{Sv}$ ($10^6\,\mathrm{m^3\,s^{-1}}$), with variations from 95 Sv to 158 Sv. For comparison, the total transport of all rivers on Earth amounts to approximately 1 Sv.

In applying the section model FEMSECT, chapter 3 of this study focuses on the North-South section at approximately 140°E (see figure 1.5). In the following, this section will be referred to as the "SR3 section" which is the standard abbreviation for the third "Southern Repeat" section . The SR3 section was occupied with hydrographic measurements repeatedly as part of the measurement programme of the World Ocean Circulation Experiment (WOCE) (Gouretski and Koltermann, 2004). Transports at the SR3 section are generally larger than at Drake passage due to the inclusion of additional Indonesian throughflow water (e.g. Georgi and Toole, 1982).

[3] meaning named by the International Hydrographic Bureau

Typical values will be given later in chapter 3.2.4.

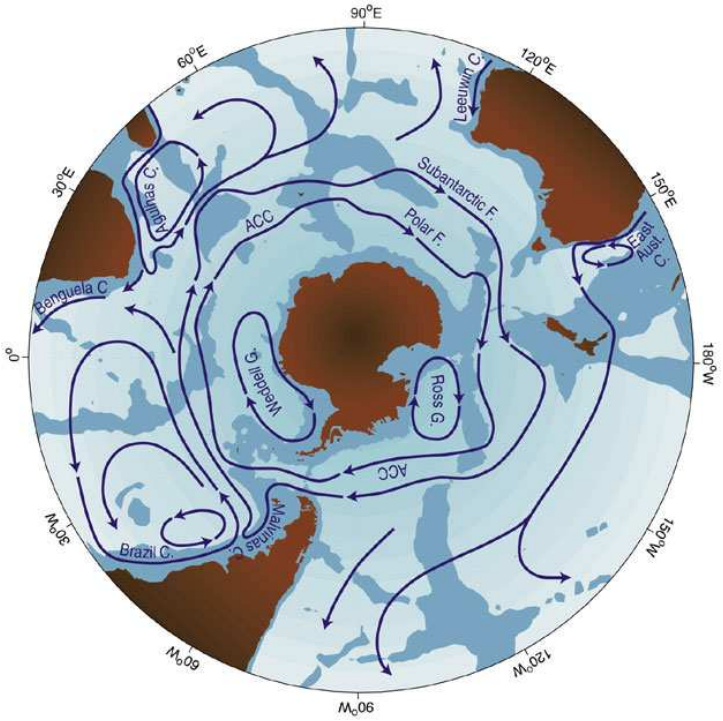

Fig. 1.4: Schematic map of major currents in the Southern Ocean. "F." stands for Front, "C." for Current and "G." for Gyre. The Southern ACC Front is not indicated on this sketch. From `http://www.science-in-salamanca.tas.csiro.au/themes/climate.htm`

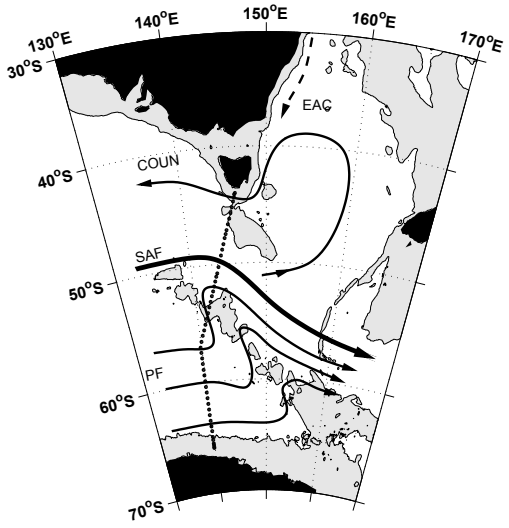

Fig. 1.5: Geometry of SR3 section between Tasmania (south of Australia) and Antarctica. "PF" denotes the Polar Front, "SAF" the Subantarctic Front, "EAC" the East Australian Current and "COUN" the westward countercurrent south of Tasmania, also called Tasman outflow. From Losch and Schröter (2004).

Numerical models can be regarded as a summary of our imperfect knowledge of the ocean circulation ...

Carl Wunsch and Detlev Stammer

1.3 Ocean modelling

In order to better understand the ocean circulation, numerical models of the ocean's physics are constructed. An large variety of different models exists, starting from very simple "toy" models to highly complex coupled Earth system models.

1.3.1 Steady-state models

Many modelling attempts aim at temporal variability studies because variability is easier to assess than mean values (e.g. in terms of sea surface height, ocean bottom pressure or current speeds). In this study, the focus is on the difference of the sea-surface height data to a particular reference surface (see chapter 2). The absolute value of this difference is much harder to assess than its temporal variability. The variability of the sea surface can be determined easily and leads in combination with a time invariable reference surface directly to the variability of this difference. However, for validating the results of these models and for benefiting most from them, a mean state of the difference is required. This is not straightforward as the time invariable reference surface is not well-known.

Providing such a mean state of the ocean is the aim of this work. The steady-state

models used here, FEMSECT (chapter 3) and IFEOM (chapter 4), describe a mean state of the ocean over a fixed time period. Therefore they do not include variability and provide no development in time. Hence many processes cannot be represented, but the models are much simpler and less expensive than their time-dependent counterpart.

Thinking backwards
Most people, if you describe a train of events to them will tell you what the result will be. There are few people, however that if you told them a result, would be able to evolve from their own inner consciousness what the steps were that led to that result. This power is what I mean when I talk of reasoning backward.

Sir Arthur Conan Doyle

1.3.2 Inverse models

A physical model only contains information about the interaction between physical processes which are included in the model equations, and the solutions are in general determined from poorly known boundary conditions and forcing fields. However, for many physical systems, additional information from measurements may also be available and this information should be used to improve the solutions. On the other hand, a set of measurements is normally sparse in space and time and does not resolve all the physical scales of interest. Therefore, to find a best possible estimate of the true state of the physical system it is necessary to use all available information both from model and measurement in an integrated system (Evensen, 1994). This integration of measurement data into models is called "data assimilation" and the models that are able to incorporate these data are called "inverse models". A sketch of the general problem is provided in figure 1.6.

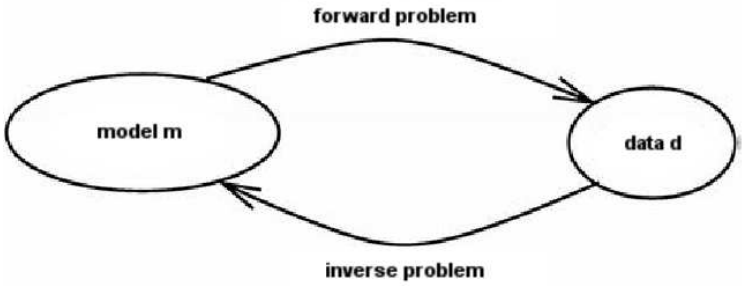

Fig. 1.6: The conventional view of inverse problems: find the model solution that predicts the measurements (data).

For assimilation into an inverse model, all types of measurements or data are possible. Therefore the following section gives a short overview on inverse ocean models in general. The focus of this work is on Mean Dynamic Topography (MDT) assimilation. An overview on ocean models incorporating MDT data will be provided in section 2.3 after the introduction of the MDT in chapter 2.

1.3.2.1 Inverse ocean models

For a long time, all estimates of the large-scale ocean circulation rested ultimately on the dynamic method and with a few exceptions were based upon a simple level-of-no-motion assumption. The requirement of a level-of-no-motion meant that the resulting schemes were essentially qualitative ones and that it is extremely difficult to attach quantitative error bounds to the results (Wunsch and Grant, 1982).

Wunsch (1977) suggested combining the thermal wind equations with additional information (data as well as prior knowledge) in a least squares sense in order to constrain the reference velocities. In this way, the classical oceanographic problem of the "level of no motion" was treated as a geophysical inverse problem.

His approach became known as "Wunsch's method" and was originally applied to a region of the ocean close to the coast of Florida. Subsequently, various models were formulated, based on similar principles but exploiting different geometries and sets of constraints. They can be classified into box models and section models (Sidorenko, 2004).

A general overview on the large diversity of inverse box models is given in Sidorenko (2004). As an example, the work of Sloyan and Rintoul (2000), based on Wunsch (1978), shall be mentioned here.

Models of single sections based on the thermal wind balance can be used to estimate geostrophic transports through these sections. Among the first approaches of this kind were Nechaev and Yaremchuk (1995) and Losch et al. (2002a). The major advantage of the section models is their simple structure and ease of use (Sidorenko, 2004). Section models are particularly useful when applied at interesting throughflow regions of the ocean with well-defined boundaries, e.g. Fram Strait (Losch et al., 2005) or the choke points of the Antarctic Circumpolar Current (ACC, see section 1.2.2). In this study, the section model FEMSECT (Losch et al., 2005) is applied to the SR3 section across the ACC (see sections 1.2.2 and 3).

Among the first attempts to invert complex Ocean General Circulation Models (OGCMs) were those realized by Tziperman and Thacker (1989); Tziperman et al. (1992a,b). A list of other modelling experiments followed, on which a review is given in Sidorenko (2004) and, from another viewpoint, in Malanotte-Rizzoli and Tziperman (1996). The approaches go as far as estimating the four dimensional ocean flow and providing initial conditions for ocean circulation forecasting (within the framework of the ECCO - Estimating the Circulation and Climate of the Ocean - project, Stammer et al., 2002, 2003).

However different the respective models and datasets are, one problem is present in each of these approaches: The choice of the error covariance matrices, that is the weighting coefficients which determine the relative influence of the observations within the optimization. This is also true for the inverse OGCM used in this study, the IFEOM (Sidorenko (2004), see chapter 4). A novel strategy for tackling the weights issue is provided in section 4.2.1.

Chapter 2

Mean Dynamic Topography

Mean dynamic topography (MDT) is the difference between the sea surface height and the geoid, as is outlined in figure 2.1. (In this text, the MDT will be marked by the Greek letter η.) The geoid is an equipotential surface of the Earth's gravity field, and thus the MDT is not directly accessible by measurements. However, it is linked to the ocean circulation via the geostrophic principle (equation 3.5 in the following chapter) and is therefore a valuable source of information for oceanography.

The following chapter gives an introduction to the fundamentals of mean dynamic topography modelling. An overview on existing satellite MDT estimates is provided and the complete MDT models are introduced.

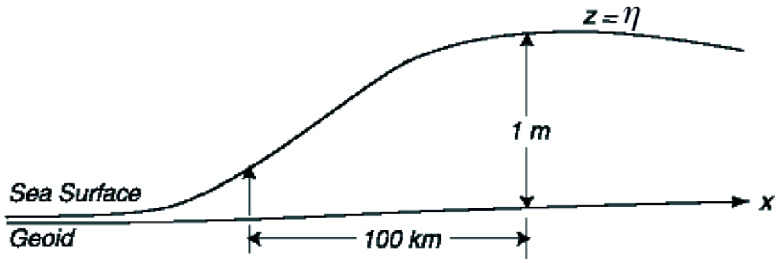

Fig. 2.1: Mean dynamic topography (MDT) η, illustration after Stewart (2008).

2.1 From outer space to frequency space

The large-scale gravity information required for this study is obtained from satellite observations. It is a long way however from the pure satellite data to the equipotential surface we are interested in. Therefore, after a short introduction to the gravity measuring satellites, an overview is given on geoid modelling and the problems arising.

2.1.1 The satellites

Altimetric information is obtained from satellites such as TOPEX/Poseidon and Jason-1, the latter launched in 2001 (figure 2.2). These satellites carry a radar altimeter measuring transit time, so the sea surface height can be retrieved if the orbit is known precisely (Peng and Wu, 2009) and appropriate corrections are made (Wunsch and Stammer, 1998).

Fig. 2.2: Jason-1 altimetric satellite, picture courtesy of NASA.

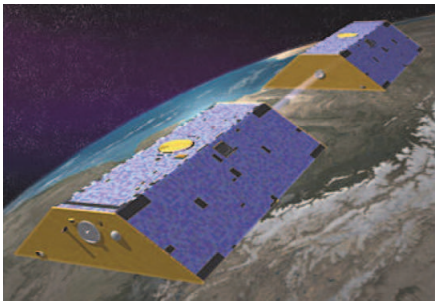

Fig. 2.3: GRACE tandem satellites, picture courtesy of NASA Earth observatory.

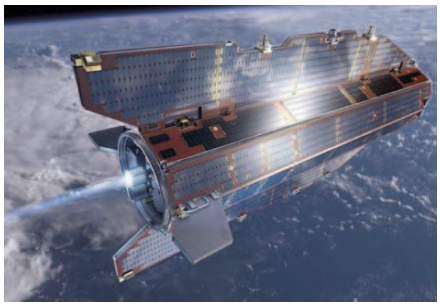

Fig. 2.4: GOCE satellite, picture courtesy of European Space Agency.

Gravity field data can be gained from tandem satellites, a method called Satellite to Satellite Tracking (SST). The only mission of this kind so far is named "GRACE" - Gravity Recovery and Climate Experiment, launched in 2002 (figure 2.3). Two satellites follow each other on the same orbit and are accelerated or decelerated by changes in the gravity field. Thus their distance between each other is modified slightly, and this change is measured "with an accuracy of some microns − about one-tenth the width of a human hair − over a distance of 220 km!" (GeoForschungsZentrum, 2006).

Another very recent and still ongoing gravity field mission is the "GOCE" - Gravity field and steady-state Ocean Circulation Explorer satellite (figure 2.4). For the first time, an Electrostatic Gravity Gradiometer consisting of three pairs of identical accelerometers is carried by a satellite. GOCE was launched in 2009 and is flying exceptionally low at an orbit altitude of about 250 km to detect the strongest possible gravity field signal (Rummel and Gruber, 2010).

2.1.2 Geoid modelling

The geoid was already described by Carl Friedrich Gauß (Torge, 2003). It is defined as the equipotential surface of the Earth's gravity field that coincides best with mean sea level (in a least squares sense, see e.g. Wahr, 1996). (Another possible definition for the geoid is the theoretical sea level of the ocean at rest (Stewart, 2008).) For oceanographers, the actual geoid height is not as important as the slope of this theoretical surface. As described at the beginning of this chapter, in combination with sea surface height data, the MDT can be derived and provides valuable information about the ocean surface currents.

The geoid is usually described in terms of spherical harmonic functions (Hughes and Bingham, 2008; Becker et al., 2012; National Research Council, 1998):

$$\begin{aligned} N(\theta,\phi) &= \frac{GM}{r\cdot\gamma(B)}\sum_{\ell=0}^{\infty}\sum_{m=0}^{\ell}\left(\frac{R}{r}\right)^{\ell}\bar{P}_{\ell m}(\cos(\theta))(\bar{C}_{\ell m}\cos(m\phi)+\bar{S}_{\ell m}\sin(m\phi)) \\ &= \frac{GM}{r\cdot\gamma(B)}\sum_{\ell=0}^{\infty}\sum_{m=0}^{\ell}\left(\frac{R}{r}\right)^{\ell}(\bar{C}_{\ell m}Y^{c}_{\ell m}(\theta,\phi)+\bar{S}_{\ell m}Y^{s}_{\ell m}(\theta,\phi)) \end{aligned} \tag{2.1}$$

with the radius vector $r = r(\theta)$ depending only on latitude θ, the Earth's radius R, the gravitational constant times the Earth's mass GM, the geodetic latitude[1] B, the normal gravity γ, the fully normalized Legendre functions $\bar{P}_{lm}(\cos(\phi))$ and the Stokes coefficients $\bar{C}_{lm}$, $\bar{S}_{lm}$. The Stokes coefficients $\bar{C}_{lm}$, $\bar{S}_{lm}$ are summarized in a vector named $\boldsymbol{x}_{cs}$ in the following.

The spherical harmonic functions are explained in more detail in appendix G.1. Geodesists use satellite gravity measurements to calculate a set of spherical harmonic coefficients $\bar{C}_{lm}$, $\bar{S}_{lm}$ up to a certain degree ℓ and order m. Often ground based techniques supplement the space data, leading to models such as the EGM96 (Lemoine et al., 1997) shown in figure 2.5. Note that here the term "model" is used in a different sense than in oceanography. In the geodetic community, a "gravitational model" refers to a set of spherical harmonic coefficients with implied rules for calculating the equipotential surface (equation 2.1).

2.1.3 The omission error problem

The spherical harmonics are a complete set of orthonormal functions and thus they form an orthonormal basis of the Hilbert space of square-integrable functions. On the unit sphere, any square-integrable function can thus be expanded as a linear combination of these:

$$f(\theta,\phi)=\sum_{\ell=0}^{\infty}\sum_{m=-\ell}^{\ell}x_{cs}^{\ell m}\,Y_{\ell m}^{cs}(\theta,\phi). \tag{2.2}$$

[1]The geodetic latitude is the angle between the normal on the earth ellipsoid and the equatorial plane. Usually, "latitude" without any specification refers to the geodetic latitude. In contrast, the geocentric latitude is the angle between the radius and the equatorial plane. On a sphere, both definitions are equivalent (Torge, 2003).

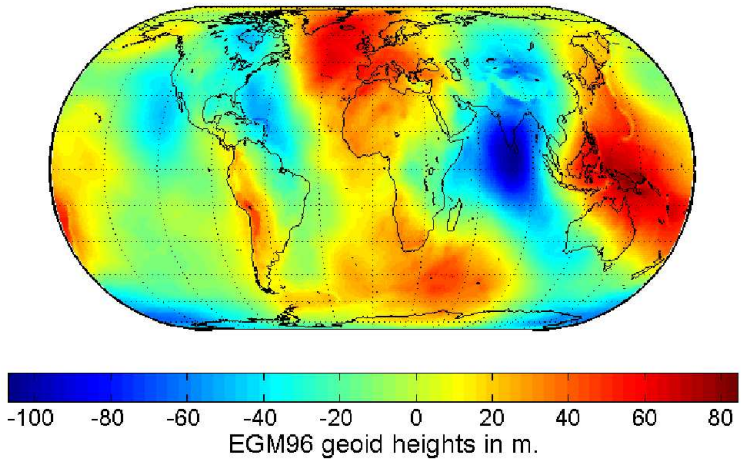

Fig. 2.5: Earth Gravitational Model 1996 (EGM96)

In practice, this series has to be truncated at a finite $\ell = \ell_{\max}$, so we get

$$f(\theta,\phi) = f_C + f_O = \sum_{\ell=0}^{\ell_{\max}} \sum_{m=-\ell}^{\ell} x_{cs}^{\ell m}\, Y_{\ell m}^{cs}(\theta,\phi) + \sum_{\ell=\ell_{\max}+1}^{\infty} \sum_{m=-\ell}^{\ell} x_{cs}^{\ell m}\, Y_{\ell m}^{cs}(\theta,\phi). \quad (2.3)$$

with an error $e = e_C + e_O$. The commission error e_C is derived by standard error propagation, whereas the omission error e_O remains unknown. Generally, it was assumed to be negligible. However, Losch et al. (2002b) showed that it does affect the commission part of the model.

This can be understood by considering the following example (Losch et al., 2002b). Assuming isotropic and homogeneous error covariances, the geoid error covariance can be written as

$$C(\psi) = \sum_{\ell}^{\ell_{\max}} p_\ell P_\ell(\cos\psi) \quad (2.4)$$

with spherical distance ψ between two points on the Earth's surface and Legendre polynomials P_ℓ. Losch et al. (2002b) derive that

$$C(\psi) = \sum_{k=0}^{\ell_{\max}} c_k \cos(k\psi) \quad \text{holds with coefficients} \quad (2.5)$$

$$c_k = \sum_{\ell=k}^{\ell_{\max}} p_\ell a_{\ell k}. \quad (2.6)$$

So a spectral coefficient c_k contains contributions from degrees $\ell = k$ up to $\ell_{\max}$, meaning modifications in the higher degrees $\ell > k$ also influence the power of the entire Fourier spectrum. In the upper right quarter of figure 2.6, the exemplary values of the $a_{\ell k}$ can be seen for large spherical harmonic degrees ℓ but low wavenumber k. This is

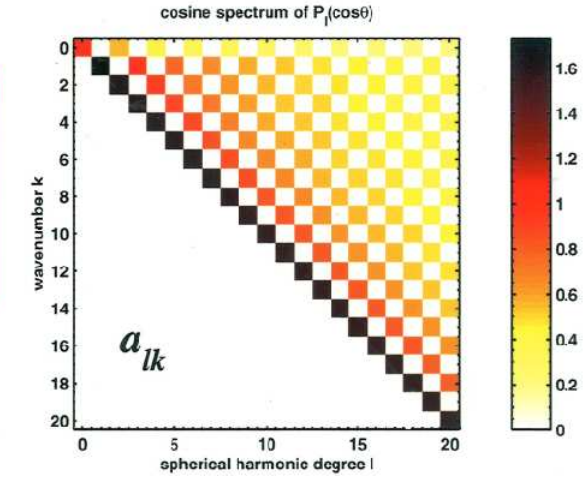

Fig. 2.6: The omission error problem, picture courtesy of Nico Sneeuw.

a typical phenomenon when changing basis sets of orthogonal functions. Additionally, any ocean model domain is only a fraction of a sphere, and therefore the spherical harmonics are not even orthogonal on this domain. For more details see Losch et al. (2002b) or Hwang (1991).

2.1.4 Filtering

Two datasets are necessary for deriving the MDT: altimetric sea surface height and the geoid. These two datasets are intrinsically different: they are expressed in different basis functions and their spatial resolution is not equal (Becker et al., 2012). Therefore, for forming the difference of the two data sets, a filter must be applied to both of them. This spectral filtering of the MDT can lead to an omission error effect (section 2.1.3) of uncertain magnitude (Losch et al., 2002b).

There are various approaches for choosing the filter (Jekeli, 1981; Bingham et al., 2008; Jayne, 2006); a common one is a Gaussian filter with a half width that is chosen in accordance with the maximum spherical harmonics degree. The special structure, particularly of the GRACE data, requires investigation of error correlation, see e.g. Swenson and Wahr (2006) and Kusche (2007). Bosch and Savcenko (2009) focus on a consistent filtering of both altimetric and geodetic data and promote an along-track filtering approach for the altimetric data evoked by their spatial distribution. However, it is not clear which filtering is most appropriate for the MDT.

2.2 Overview of recent satellite MDT estimates

Rio and Hernandez (2004) used the altimetric Mean Sea Surface (MSS) CLS01 (Hernandez et al., 2001) and the EIGEN-2 geoid (Reigber et al., 2003) for the computation of the Rio-05 MDT. The MDT was constructed with the help of the Levitus hydrographic climatology (Levitus et al., 2001), hydrographic profiles distributed via Système d'Informations Scientifiques pour la Mer (SISMER) from Institut Français de Recherche pour l'Exploitation de la MER (IFREMER) and surface drifter velocities deployed as part of the WOCE (World Ocean Circulation Experiment) and TOGA (Tropical Ocean and Global Atmosphere) Surface Velocity Program (SVP). A "synthetic" method was developed for the combination of the different data sets on a 1/2 degree global grid and a Gaussian filter with a half width of 400 km was applied (Rio and Hernandez, 2004).

A similar method was used for deriving the more recent CNES-CLS09 MDT (Rio et al., 2011). Updated data sets were used for the computation on 1/4 degree global grid, including the geoid model EIGEN-GRGS.RL02 (Bruinsma et al., 2010) based on 4 1/2 years of GRACE data. An "optimal" filtering method was developed which weights the observations by the inverse error covariances. The latter however, are determined by the help of the Global Ocean ReanalYsiS (GLORYS) (Rio et al., 2011). This MDT will be used for comparison to the results of this study in chapter 4.3.3.

Maximenko et al. (2009) use the Goddard Space Flight Center Mean Sea Surface 2000 (GSFCMSS00) and the GRACE Gravity Model 2002 (GGM02C) geoid (Tapley et al., 2003). Near-surface velocities from a network of ocean drifters, hydrographic profiles and wind data are synthesized. These global data sets are used in the context of ocean surface momentum balance. A cost function is minimized on a global grid of 1/2 degree resolution and Laplacian smoothing is applied (Maximenko et al., 2009).

The DNSC08 MSS (Andersen and Knudsen, 2009) is based on data from a total of eight satellite missions, including Jason-1 and Envisat radar altimetry as well as ICESat laser altimetry. The difference to the EGM08 geoid (Pavlis et al., 2008) is computed and slightly smoothed by using a correlation length of 75 km for the final reinterpolation. The final DNSC08 MDT is provided on a global grid with $1'$ resolution (Andersen and Knudsen, 2009).

The DTU10MSS mean sea surface (Knudsen et al., 2011) is an update of the DNSC08MSS mean sea surface. It is combined with two months of GOCE gravity data by Knudsen et al. (2011) to give a new GOCE based MDT. A truncated Gaussian filter with a half-width radius of 140 km was used for noise removal. The authors however admit that there is always an element of subjectivity in the determination of the optimal filter radius.

Albertella et al. (2008) promote a new approach of filtering along the altimetry profiles. The altimetry data has a high resolution on the geodetic satellite tracks, and to avoid initial gridding, the necessary computations are done on these profiles. A one-dimensional filter for altimetry data on profiles is designed. However, there are systematic differences between 2D filtering and 1D filtering, and to compensate for these differences, a filter correction was developed. Eventually, data of Jason-1 and TOPEX-EM are combined with the EGM08 geoid model (Pavlis et al., 2008) to give

a new DOT (Dynamic Ocean Topography). While the filtering is essential for all of the MDT calculation methods, it is put into the centre of attention in this "profile approach".

In summary, the different MDT estimates demonstrate the insufficiency of the satellite data. Filtering and often also in-situ hydrographic data are required to complement the satellite observations. In general, error estimates for the MDT are crude and no standardized method exists for an evaluation of the quality of the MDT estimates. In this work, an MDT estimate will be investigated that is not subject to in-situ data or additional posterior filtering.

2.3 Ocean models incorporating MDT data

Many traditional ocean data assimilation systems only use sea surface elevation anomalies without the geoid as a reference surface (e.g. Oke et al., 2008; Vidard et al., 2009; Mellor and Ezer, 1991). This is useful in variability studies; however, for estimating a mean state of the ocean circulation, information about the geoid is required.

Prior to the release of satellite gravity data from the GRACE and GOCE missions (see section 2.1.1), the quality of the available data for MDT computation was not sufficient to recover the details of the general ocean circulation (Haines et al., 2011). Only the very large scales (> 5000 km) of the dynamic topography could be recovered and compared with the early oceanographic results obtained from hydrographic data, e.g. Levitus and Boyer (1994). The recent satellite missions then started to provide a more accurate and higher resolution global picture of the Earth's gravity field than ever before (Johannessen et al., 2003).

That encouraged a large variety of MDT assimilation studies into ocean circulation models. For example, Birol et al. (2005) assimilated CHAMP and GRACE data into the HYCOM model, and Castruccio et al. (2008) used GRACE data within the OPA OGCM. The ECCO (Estimating the Circulation and Climate of the Ocean) consortium, including the follow-up projects ECCO-GODAE, ECCO2 and the German partner project GECCO, used GRACE data among many other data sets for assimilation mainly into the MITgcm (e.g. Wunsch et al., 2009; Wunsch and Heimbach, 2006; Stammer et al., 2007). The GOCINO project used specific scenarios for the integration of GOCE data products into four major operational oceanography systems, notably MERCATOR, MFS, FOAM and TOPAZ, and into the seasonal forecasting system at ECMWF (Knudsen, 2010).

The DFG Priority Programme "Mass transport and Mass distribution in the System Earth" (see also `www.massentransporte.de`) aimed at analysing the contribution of the new generation of satellite gravity and altimetry missions to geosciences. Ocean mass and also ocean circulation were among the foci of this programme (Ilk et al., 2005), as illustrated in figure 2.7. Within the project GEOTOP (Sea Surface Topography and Mass Transport of the Antarctic Circumpolar Current), the "profile approach" (Bosch and Savcenko, 2010) was developed for the computation of a new GRACE MDT data set. GRACE data were also used by Janjić et al. (2011) for assimilation into the FEOM (Finite Element Ocean Model). The projects INTERMOD

(Consistent integration of global gravity field information into earth process models, [2]) and RIFUGIO (Rigorous Fusion of Gravity Field into Stationary Ocean Models, [3]) provided the basis for this work.

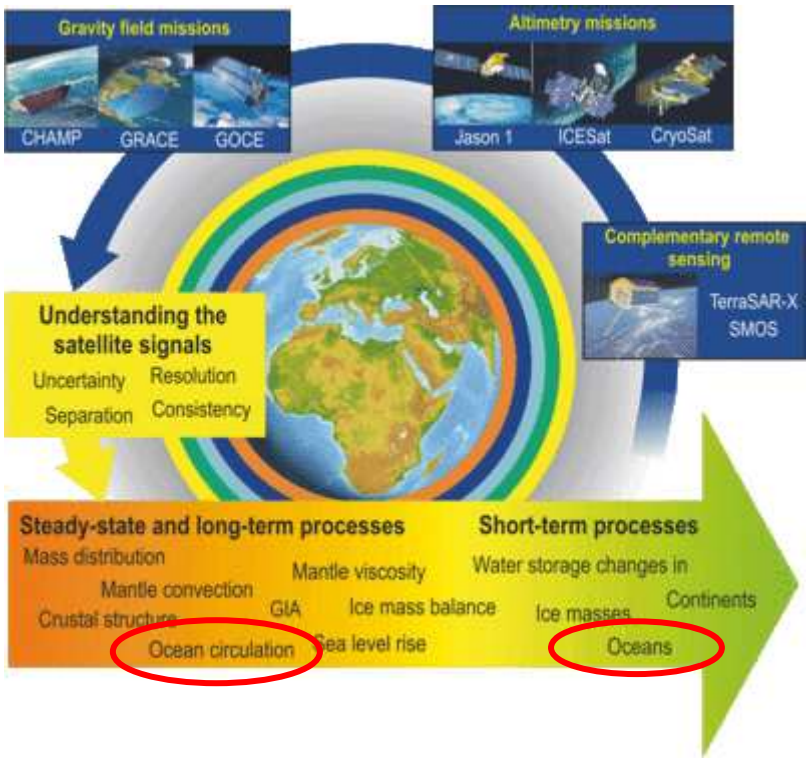

Fig. 2.7: Scheme of the framework of the DFG Priority Programme "Mass transport and Mass distribution in the System Earth"

[2] http://www.massentransporte.de/index.php?id=201&L=0%2F%2Fadminbereich%2Fdesignconfig.php%3F

[3] http://www.massentransporte.de/index.php?id=217&L=0%2F%2Fadminbereich%2Fdesignconfig.php%3F

2.4 Complete MDT models

This section explains the so-called complete models for gravity and Mean Dynamic Topography. For the computation of the complete MDT model, the geodetic normal equations are treated in a special way. The model space is "completed" by prior stochastic information. Eventually, the complete "Rifugio MDT" is presented.

2.4.1 Complete gravity field models

The reconstruction of the Earth's gravity field from satellite observations is an ill-posed problem. A finite number of satellite measurements at discrete points at high altitude are used to reconstruct the detailed structure of the gravity field on the Earth's surface. This ill-posed problem needs some kind of regularization which is usually achieved by truncation of the spherical harmonics series expansion. The restriction to a sub-domain of the frequency space leads to incomplete models, introducing errors into the derived Earth process parameters. The omission error arising from this band-limitation of the available information was already introduced in section 2.1.3.

To tackle this problem, Schuh and Becker (2008) developed a complete gravity field model within the project INTERMOD (Consistent integration of global gravity field information into Earth process models). The corresponding MDT is called "INTERMOD MDT" in the following. A summary is given here on the use of the smoothness characteristics of the potential field for the construction of the gravity field model. The formulation in the Hilbert space $\mathcal{H}_\Gamma^1$ of square integrable functions u on a sphere

$$\Gamma(\|u\|^2_{\mathcal{H}_\Gamma} = \iint_\Gamma u^2 d\sigma < \infty) \text{ with norm } \|u\|_{\mathcal{H}_\Gamma^1} = \|u\|_{\mathcal{H}_\Gamma} + \|Du\|_{\mathcal{H}_\Gamma}$$

results in restrictions with respect to the degree variances[4]. These restrictions are used to establish stochastic processes on the sphere which are used as a background information for the whole modelling process. In principle, deterministic as well as stochastic approaches are possible for the construction of the background model. Here, stochastic processes are chosen because they can be defined such that they exactly reflect the smoothness conditions of the potential field (Schuh, W.-D. and Becker, S., 2009, pers. comm.).

The Hilbert space $\mathcal{H}_\Gamma^1$ can be split into three subdomains that are named commission, transition and omission domain, see figure 2.8. The commission subdomain is mainly determined by the real measurements whereas in the transition zone, this information is supported by the a priori knowledge about the smoothness of the potential field. In the omission subspace,the signal-to-noise ratio is too small and sufficient data are not available. Hence, the omission domain is fixed by the background model up to infinity providing the completeness of the model (Schuh, W.-D. and Becker, S., 2009, pers. comm.).

[4]The Hilbert space $\mathcal{H}_\Gamma^1$ is not a Sobolev space. The latter would require the norm to be defined as $\|u\|_{\mathcal{W}^{1,2}} = \sqrt{\|u\|^2_{\mathcal{H}_\Gamma} + \|Du\|^2_{\mathcal{H}_\Gamma}}$.

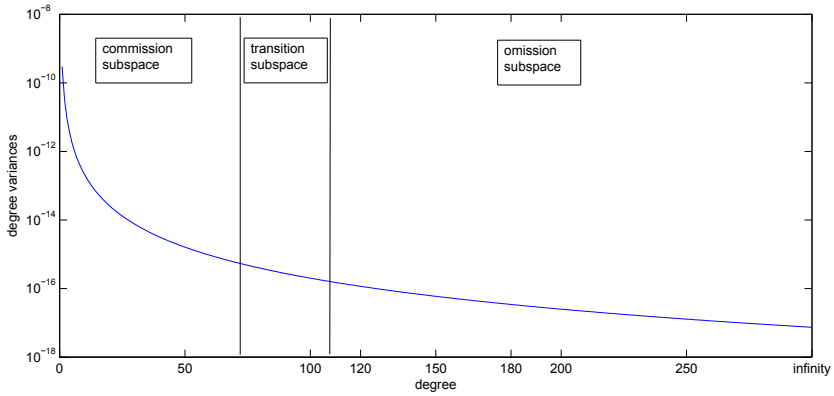

Fig. 2.8: Separation of the model space (Schuh and Becker, 2008)

The signal-to-noise ratio of the satellite measurements decreases dramatically with increasing spherical harmonic degree. Hence the data are not sufficient in the transition and omission subdomain and must be supported by prior knowledge. For this purpose, two stochastic processes are defined that are both stationary and isotropic.

The first (type I) process is established by regarding the spherical harmonic coefficients as random variables with expectation 0 and covariance

$$\mathrm{Cov}(u,v) = \sum_{\ell=0}^{\infty} \Sigma\{\mathcal{S}_\ell\} P_\ell(\cos\psi).$$

Here, $\mathcal{S}_\ell$ is the random variable for the degree variance σ_ℓ, and the Legendre polynomial P_ℓ depends only on the spherical distance ψ between two points on the surface u and v. This is an a priori assumption about the smoothness characteristics of the gravity potential (Schuh, W.-D. and Becker, S., 2009, pers. comm.). The stochastic process of type I is applied to support the observations in the transition domain. The variances of the spherical harmonic coefficients are defined according to Kaulas rule of thumb (see appendix G.2, Kaula, 1966) as

$$\Sigma\{\bar{C}_{\ell m}\} = \Sigma\{\bar{S}_{\ell m}\} = \frac{10^{-10}(2\ell+1)}{\ell^4}, \quad \ell = \ell_{t_{\min}}, ..., \ell_{t_{\max}}, \quad m = 0, ..., \ell$$

for the degrees ℓ in the transition zone.

The second (type II) process results from an amplitude-phase description of the basis functions. The amplitudes are kept constant depending on degree ℓ and degree variances σ_ℓ:

$$A_{\ell m}^2 = \frac{2}{2\ell+1}\sigma_\ell^2$$

while the phases are uniformly distributed with expectation 0 and covariance

$$\sum_{\ell=0}^{\infty} \sigma_\ell^2 P_\ell(\cos\psi) = \mathrm{cov}(\psi, \sigma_\ell^2)$$

(Schuh, W.-D. and Becker, S., 2009, pers. comm.). A stochastic process of type II is utilized to replace the lacking measurements in the omission subdomain. The constant degree variances are therefore set to

$$\sigma_\ell^2 = \frac{10^{-10}(2\ell+1)}{\ell^4}, \;\; \ell = \ell_{o_{\min}}, ..., \ell_{o_{\max}}.$$

The resulting model forms a complete base in the entire space which can be represented in both frequency (spherical harmonics) and space domain (data grids). The derived variance/covariance information is invertible and therefore the gridded gravity field information can directly be integrated into ocean circulation models (Schuh and Becker, 2008).

2.4.2 Combined MDT model

This section (2.4.2) and the following one (2.4.3) summarize the work of Becker et al. (2012) within the framework of the project RIFUGIO (RIgorous FUsion of Gravity field Into stationary Ocean models). Correspondingly, the MDT resulting from this effort will be called "Rifugio MDT". The corresponding figures are redrawn from Becker et al. (2012).

This MDT modelling approach is tailored to the subsequent use of the MDT within ocean models. These ocean models are usually present on a two- or three-dimensional grid and the corresponding model equations are solved on the grid by methods like the Finite Element (FE) method. We take on this perspective to produce a data set that is given on the same grid as the ocean model and therefore can be directly assimilated.

The geoid is represented in the usual way as a sum of spherical harmonic functions as in equation 2.1. In contrast, the mean dynamic topography is represented by a linear combination of finite element base functions $b_j(\phi, \lambda)$:

$$MDT(\phi, \lambda) = \sum_{j \in J} \boldsymbol{x}_{FE}(j) b_j(\phi, \lambda) \tag{2.7}$$

where the basis functions b_j are defined on the ocean model grid.

The unknown coefficients for the MDT are collected in the vector $\begin{bmatrix} \boldsymbol{x}_{cs} \\ \boldsymbol{x}_{FE} \end{bmatrix}$ and the observation equations for the altimetric information $\boldsymbol{l}_{MSS}$ can be written as

$$\boldsymbol{l}_{MSS} + \boldsymbol{v}_{MSS} = \begin{bmatrix} \boldsymbol{A}_{cs} & \boldsymbol{A}_{FE} \end{bmatrix} \cdot \begin{bmatrix} \boldsymbol{x}_{cs} \\ \boldsymbol{x}_{FE} \end{bmatrix} \tag{2.8}$$

with the coefficient matrices $\boldsymbol{A}_{cs}$ and $\boldsymbol{A}_{FE}$ and a stochastic model $\boldsymbol{\Sigma}_{MSS}$ for the errors $\boldsymbol{v}_{MSS}$ (Becker et al., 2012). The normal equations for the altimetry are constructed as in Becker et al. (2012):

$$\begin{bmatrix} \boldsymbol{A}_{cs}^T \boldsymbol{\Sigma}_{MSS}^{-1} \boldsymbol{A}_{cs} & \boldsymbol{A}_{cs}^T \boldsymbol{\Sigma}_{MSS}^{-1} \boldsymbol{A}_{FE} \\ \boldsymbol{A}_{FE}^T \boldsymbol{\Sigma}_{MSS}^{-1} \boldsymbol{A}_{cs} & \boldsymbol{A}_{FE}^T \boldsymbol{\Sigma}_{MSS}^{-1} \boldsymbol{A}_{FE} \end{bmatrix} \cdot \begin{bmatrix} \boldsymbol{x}_{cs} \\ \boldsymbol{x}_{FE} \end{bmatrix} = \begin{bmatrix} \boldsymbol{A}_{cs}^T \boldsymbol{\Sigma}_{MSS}^{-1} \boldsymbol{l}_{Mss} \\ \boldsymbol{A}_{FE}^T \boldsymbol{\Sigma}_{MSS}^{-1} \boldsymbol{l}_{MSS} \end{bmatrix} \tag{2.9}$$

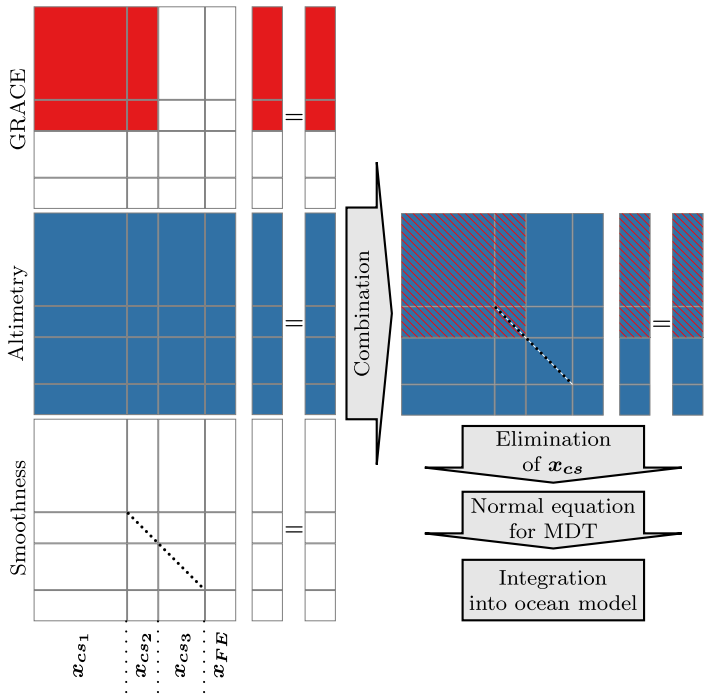

Fig. 2.9: Scheme of normal equations and combination model (Becker et al., 2012)

and for brevity renamed to

$$\begin{bmatrix} \boldsymbol{N}_{cs}^{MSS} & \boldsymbol{N}_{cs,FE}^{MSS} \\ \boldsymbol{N}_{FE,cs}^{MSS} & \boldsymbol{N}_{FE}^{MSS} \end{bmatrix} \cdot \begin{bmatrix} \boldsymbol{x}_{cs} \\ \boldsymbol{x}_{FE} \end{bmatrix} = \begin{bmatrix} \boldsymbol{n}_{cs}^{MSS} \\ \boldsymbol{n}_{FE}^{MSS} \end{bmatrix} \tag{2.10}$$

In our case, for the gravity field also the full variance/covariance information is available in terms of the normal equations:

$$\boldsymbol{N}_{cs}^{G}\boldsymbol{x}_{cs} = \boldsymbol{n}_{cs}^{G} \tag{2.11}$$

Both sets of normal equations 2.10 and 2.11 result from independent observation groups so that the addition theorem for normal equations applies (Becker et al., 2012):

$$\begin{bmatrix} \boldsymbol{N}_{cs}^{MSS} + \boldsymbol{N}_{cs}^{G} & \boldsymbol{N}_{cs,FE}^{MSS} \\ \boldsymbol{N}_{FE,cs}^{MSS} & \boldsymbol{N}_{FE}^{MSS} \end{bmatrix} \cdot \begin{bmatrix} \boldsymbol{x}_{cs} \\ \boldsymbol{x}_{FE} \end{bmatrix} = \begin{bmatrix} \boldsymbol{n}_{cs}^{MSS} + \boldsymbol{n}_{cs}^{G} \\ \boldsymbol{n}_{FE}^{MSS} \end{bmatrix} \tag{2.12}$$

This approach is sketched in figure 2.9.

The matrix $\boldsymbol{N}_{cs}^{MSS} + \boldsymbol{N}_{cs}^{G}$ is designed such that it is invertible, and therefore the gravity field parameters $\boldsymbol{x}_{cs}$ can be eliminated from the system. We get an estimate

of the normal equation for the MDT on the Finite Elements:

$$\underbrace{\left(\boldsymbol{N}_{FE}^{MSS} - \boldsymbol{N}_{FE,cs}^{MSS}\left(\boldsymbol{N}_{cs}^{MSS} + \boldsymbol{N}_{cs}^{G}\right)^{-1}\boldsymbol{N}_{cs,FE}^{MSS}\right)}_{=:\boldsymbol{N}_{FE}}\boldsymbol{x}_{FE}$$
$$= \underbrace{\boldsymbol{n}_{FE}^{MSS} - \boldsymbol{N}_{FE,cs}^{MSS}\left(\boldsymbol{N}_{cs}^{MSS} + \boldsymbol{N}_{cs}^{G}\right)^{-1}\left(\boldsymbol{n}_{cs}^{MSS} + \boldsymbol{n}_{cs}^{G}\right)}_{=:\boldsymbol{n}_{FE}} \quad (2.13)$$

or in brief,

$$\boldsymbol{N}_{FE}\boldsymbol{x}_{FE} = \boldsymbol{n}_{FE}. \quad (2.14)$$

This system of equations can be solved for $\boldsymbol{x}_{FE}$ and the normal equation matrix $\boldsymbol{N}_{FE}$ represents the inverse error covariance of the resulting MDT on the Finite Elements.

This method derived by Becker et al. (2012) does not require any explicit filtering for the calculation of the MDT. Therefore, no unknown amount of signal is lost due to an additional filtering procedure and the available data can be exploited to the largest possible extent.

2.4.3 Stochastic modelling

According to the available information about the data and errors, the vector of unknowns is separated into different domains: $\boldsymbol{x}_{cs} = \left[\begin{array}{ccccc}\boldsymbol{x}_{cs1}^T & \boldsymbol{x}_{cs2}^T & \boldsymbol{x}_{cs3}^T & \boldsymbol{x}_{cs4}^T & \boldsymbol{x}_{FE}^T\end{array}\right]^T$. Using the example of the GRACE-only gravity field model ITG-Grace2010s, figure 2.10 gives an overview over the frequency domains. The ITG-Grace2010s and its full error covariance matrix are computed up to degree and order 180, so its signal content covers the frequency domains $\boldsymbol{x}_{cs1}$ and $\boldsymbol{x}_{cs2}$. Up to degree and order 150, it has an accuracy of 1 cm in terms of geoid heights ($\boldsymbol{x}_{cs1}$), beyond it is less accurate ($\boldsymbol{x}_{cs2}$). Assuming that GRACE measurements do not contribute any signal content beyond degree and order 180, the coefficients $\boldsymbol{x}_{cs3}$ and $\boldsymbol{x}_{cs4}$ are determined by altimetry only. The altimetric measurements are not globally distributed and therefore do not contain enough information to determine all the coefficients. As in section 2.4.1, additional prior information about the smoothness of the potential is introduced and thus the following pseudo-observation equations are constructed (Schuh and Becker, 2010):

$$\left[\begin{array}{c}\boldsymbol{0}\\ \boldsymbol{0}\\ \boldsymbol{0}\end{array}\right] + \left[\begin{array}{c}\boldsymbol{v}_1^{\text{smooth}}\\ \boldsymbol{v}_2^{\text{smooth}}\\ \boldsymbol{v}_3^{\text{smooth}}\end{array}\right] = \left[\begin{array}{ccc}\boldsymbol{I} & \boldsymbol{0} & \boldsymbol{0}\\ \boldsymbol{0} & \boldsymbol{I} & \boldsymbol{0}\\ \boldsymbol{0} & \boldsymbol{0} & \boldsymbol{I}\end{array}\right] \cdot \left[\begin{array}{c}\boldsymbol{x}_{cs2}\\ \boldsymbol{x}_{cs3}\\ \boldsymbol{x}_{cs4}\end{array}\right] \quad (2.15)$$

The Stokes coefficients are interpreted as random variables: $\boldsymbol{\mathcal{X}}_{cs}^{\text{smooth}} \sim \boldsymbol{\mathcal{N}}(\boldsymbol{0}, \boldsymbol{\Sigma}_{cs}^{\text{smooth}})$. Kaulas rule of thumb (see G.2, Kaula, 1966) yields the degree variances σ_ℓ^2 for a degree ℓ and describes the signal content per degree of the gravitational potential coefficients. It also provides the variance of individual coefficients $\sigma_{\ell m}^2$ of degree ℓ:

$$\sigma_\ell^2 = 10^{-10}\frac{2\ell+1}{\ell^4} \quad (2.16)$$

$$\sigma_{\ell m}^2 = \frac{10^{-10}}{\ell^4} \quad (2.17)$$

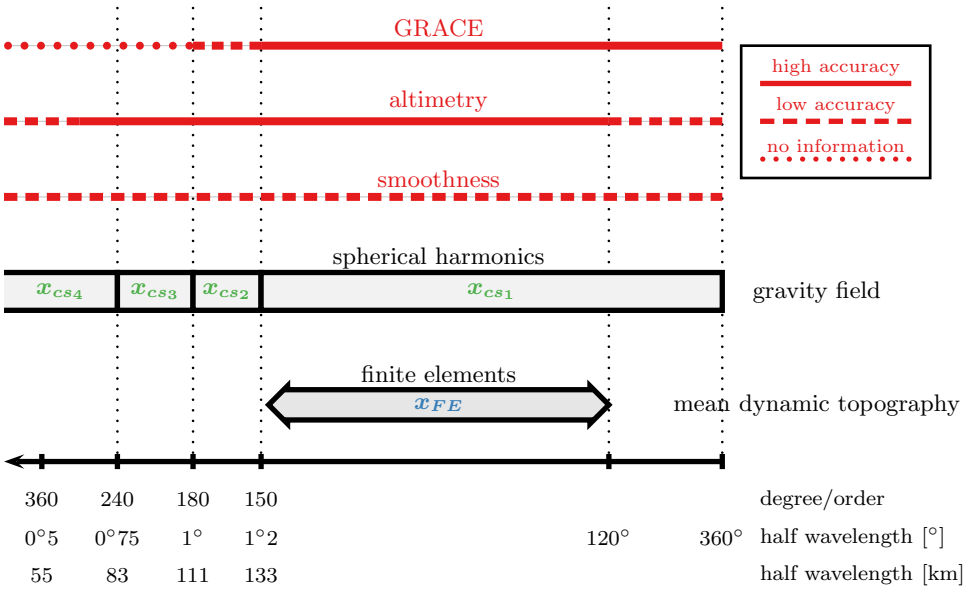

Fig. 2.10: Frequency domains of observations, parametrization and accuracy, (Becker et al., 2012)

Altogether, the stochastic model reads:

$$\boldsymbol{\Sigma}_{cs}^{\text{smooth}} = \begin{bmatrix} \boldsymbol{\Sigma}_{cs2}^{\text{smooth}} & \mathbf{0} & \mathbf{0} \\ \mathbf{0} & \boldsymbol{\Sigma}_{cs3}^{\text{smooth}} & \mathbf{0} \\ \mathbf{0} & \mathbf{0} & \boldsymbol{\Sigma}_{cs4}^{\text{smooth}} \end{bmatrix} \tag{2.18}$$

$$= \begin{bmatrix} \text{diag}(\boldsymbol{\sigma}_{\ell m2}^2) & \mathbf{0} & \mathbf{0} \\ \mathbf{0} & \text{diag}(\boldsymbol{\sigma}_{\ell m3}^2) & \mathbf{0} \\ \mathbf{0} & \mathbf{0} & \text{diag}(\boldsymbol{\sigma}_{\ell m4}^2) \end{bmatrix} \tag{2.19}$$

The altimetric measurements contain frequencies beyond degree and order 240. The corresponding spherical harmonics coefficients are summarized in the parameter vector $\boldsymbol{x}_{cs4}$ and treated separately:

$$\boldsymbol{l}_{MSS} + \boldsymbol{v}_{MSS} = \begin{bmatrix} \boldsymbol{A}_{cs1} & \boldsymbol{A}_{cs2} & \boldsymbol{A}_{cs3} & \boldsymbol{A}_{FE} \end{bmatrix} \cdot \begin{bmatrix} \boldsymbol{x}_{cs1} \\ \boldsymbol{x}_{cs2} \\ \boldsymbol{x}_{cs3} \\ \boldsymbol{x}_{FE} \end{bmatrix} + \boldsymbol{A}_{cs4} \cdot \boldsymbol{x}_{cs4} \tag{2.20}$$

Expressing the last term as a random variable, $\boldsymbol{A}_{cs4} \cdot \boldsymbol{\mathcal{X}}_{cs} = \boldsymbol{\mathcal{S}}$, it can be defined by its first two moments, the expectation $\boldsymbol{E}\{\boldsymbol{\mathcal{S}}\}$ and the covariances $\boldsymbol{\Sigma}\{\boldsymbol{\mathcal{S}}\}$. Later on in section 4.2.3, we will apply two different approaches regarding the stochastic characteristics of $\boldsymbol{\mathcal{S}}$.

2.4.4 Final geodetic MDT

The calculation method described above and in more detail in Becker et al. (2012) is referred to as the "Rifugio approach" and the resulting geodetic MDT computed this way is named "Rifugio MDT" in the following. This MDT estimate was developed and computed at the Institute of Geodesy and Geoinformation (IGG) at the University of Bonn and was made available to the AWI within the framework of this project. The Rifugio MDT contains many physical structures, but especially at small scales noise dominates (see figure 2.11a). However, the Rifugio MDT cannot be regarded by itself without considering its associated covariance information which is partly shown in figure 2.11b (Becker, S., 2009, pers. comm.). Ideally, the error covariance information reflects the "unrealistic" features of the MDT in such a way that they undo each other whilst assimilated into an ocean model. That of course complicates the comparison of the geodetic Rifugio MDT to those of other authors, and therefore we directly proceed to the evaluation of the MDT via its effect on the ocean models in the following chapters.

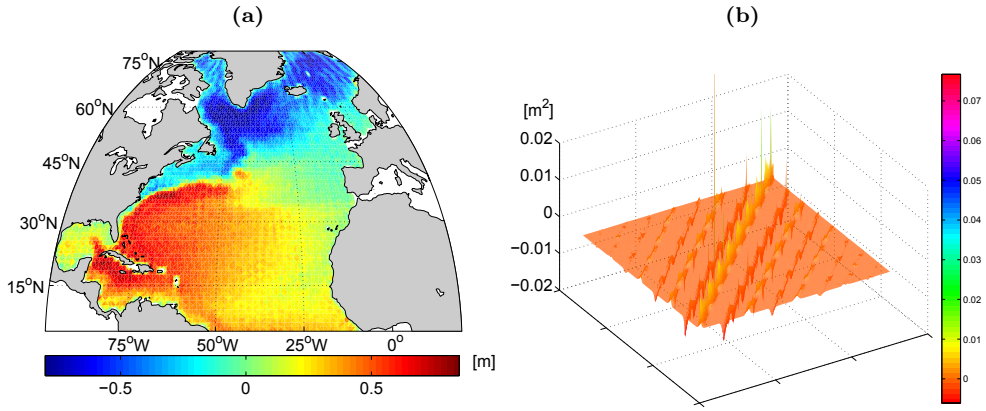

Fig. 2.11: Rifugio MDT and its associate error description: (a) Rifugio MDT x_{data} without smoothing, usually not shown this way, (b) Detail of the corresponding Rifugio error covariance matrix, refering to the inner surface nodes between 45.5°W-53.5°W and between 4.5°N-65.5°N. (The numbering of the mesh nodes is along longitudes from South to North and from West to East.)

Two stationary ocean models are used for MDT assimilation in this study. First, the two-dimensional FEMSECT model is applied to a section in the Southern Ocean in the following chapter. Afterwards in chapter 4, the three-dimension IFEOM for the North Atlantic is investigated under the influence of the new Rifugio MDT.

Chapter 3

Combination of Ocean and MDT: FEMSECT

To understand the system,
you need simpler models.

Dirk Olbers

3.1 The 2D model FEMSECT

The **F**inite **E**lement **M**ethod **Sect**ion model FEMSECT (Losch et al., 2005) is a simple model for analysing hydrographic measurements of temperature and salinity together with velocity measurements. It can theoretically be applied to any two dimensional section in the ocean.

The principle of FEMSECT is to compute velocity from the density and the thermal wind equations. With this approach, only the shear of the velocity field can be calculated, thus assumptions about the absolute velocities are required. This is called the "reference velocity problem" or "level-of-no-motion-problem" of oceanography (Wunsch, 1996). In FEMSECT, this problem may be solved by using additional observations such as velocity measurements or the gradients of dynamic topography.

On a merry-go-round in the night,
Coriolis was shaken with fright.
Despite how he walked,
'Twas like he was stalked,
By some fiend always pushing him right.

David Morin, Eric Zaslow, E'beth Haley,
John Golden, Nathan Salwen

3.1.1 Thermal wind

The geostrophic balance is defined by

$$f\boldsymbol{k} \times \boldsymbol{u} + \frac{1}{\rho}\nabla p = 0 \tag{3.1}$$

with the Coriolis parameter f, vertical unit vector $\boldsymbol{k}$, velocities $\boldsymbol{u} = (u, v, w)$, density ρ and pressure p, see e.g. Marshall and Plumb (2008). The smallness of the Rossby number ($R_0 \sim 0.01$) for large-scale motion in the ocean allows the application of this balance. The pressure gradient is balanced by the Coriolis force, so that the geostrophic current velocities are given by

$$\begin{pmatrix} u_g \\ v_g \end{pmatrix} = \frac{1}{\rho_{\text{ref}} f} \begin{pmatrix} -\frac{\partial p}{\partial y} \\ \frac{\partial p}{\partial x} \end{pmatrix} \tag{3.2}$$

Taking the z-derivative and replacing $\frac{\partial p}{\partial z}$ by the hydrostatic balance $\frac{\partial p}{\partial z} = -\rho g$ leads to the thermal wind equations

$$\begin{pmatrix} \frac{\partial u}{\partial z} \\ \frac{\partial v}{\partial z} \end{pmatrix} = \frac{g}{\rho_{\text{ref}} f} \begin{pmatrix} \frac{\partial \rho}{\partial y} \\ -\frac{\partial \rho}{\partial x} \end{pmatrix} \tag{3.3}$$

The second equation of (3.3) is integrated in the vertical to produce an expression for the across-section velocity v:

$$v = v_{\text{ref}} - \frac{g}{\rho_{\text{ref}} f} \left(\int_{-h}^{z} \frac{\partial \rho}{\partial x} dz \right) \tag{3.4}$$

with unknown reference velocity v_{ref}.

The FEMSECT model solves for fluxes across a two dimensional section, thus only the second equation is considered. Vertical or along section velocity components are not taken into account. In this study, FEMSECT is applied to the WOCE SR3 section (see section 1.2.2) between Tasmania and Antarctica. The model grid is displayed in figure 3.1. Note that the SR3 section is not exactly north-south oriented, so that it is not accurate to talk about east-west velocities. However, as the SR3 section spans all across the Southern Ocean, the across-section mass transport is equal to the ACC transport.

3.1.2 Sea surface topography

The geostrophic relationship is now applied to the sea surface. Consider a level surface slightly below the sea surface, e.g. at $z = -r$ as in Stewart (2008). Pressure at this level surface is given by $p = -g\rho_{\text{ref}}(\eta + r)$ assuming ρ and g are essentially constant in the upper few meters of the ocean. Substituting this into equations (3.2) leads to

$$\begin{pmatrix} u_g \\ v_g \end{pmatrix} = \frac{g}{f} \begin{pmatrix} \frac{-\partial \eta}{\partial y} \\ \frac{\partial \eta}{\partial x} \end{pmatrix} \tag{3.5}$$

where η is the elevation of the free ocean surface relative to the level surface. This level surface must be an equipotential surface of the Earth's gravity field. It is not

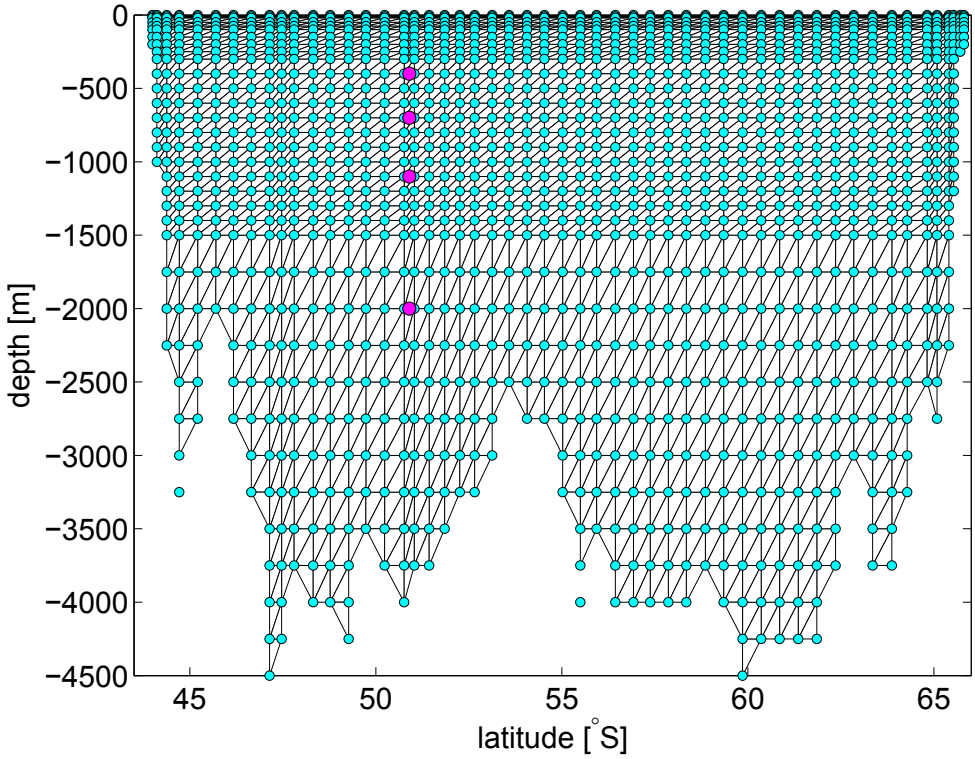

Fig. 3.1: FEMSECT model grid and triangulation for the SR3 section. Available measurements of temperature and salinity are shown in light blue and those of velocity in magenta. Some hydrographic measurements at the ocean bottom are not connected to the model grid because respective triangles would be slanted.

important which of these possible reference surfaces is chosen, but it is common to use the one that coincides best with mean sea level. This equipotential reference surface is called the geoid.

The simple scaling

$$\Delta\eta = \frac{fLU}{g}$$

for a current speed $U = 0.1\,\mathrm{m\,s^{-1}}$ over a distance $L = 1000\,\mathrm{km}$ with $f = 10^{-4}\,\mathrm{s^{-1}}$ shows that variations of η are in the order of 1 m. In this study, we try to gain information about η from satellite measurements.

3.1.3 Least squares method

Surface velocities from equation (3.5), assumed reference velocities at the ocean floor, direct velocity measurements and velocity shear from hydrographic measurements do usually not agree with each other. Therefore a search for the best fit is necessary. A quadratic cost function is defined and minimized in the sense of least squares:

$$\begin{aligned}\mathcal{J} &= \frac{1}{2}\left(T^* - \Phi_T T\right)^T \mathbb{W}_T \left(T^* - \Phi_T T\right) + \frac{1}{2}\left(S^* - \Phi_S S\right)^T \mathbb{W}_S \left(S^* - \Phi_S S\right) \\ &+ \left(T^* - \Phi_T T\right)^T \mathbb{W}_{TS} \left(S^* - \Phi_S S\right) + \frac{1}{2}\left(v^* - \Phi_v v\right)^T \mathbb{W}_v \left(v^* - \Phi_v v\right) \\ &+ \frac{1}{2}\left(v_{\mathrm{ref}} - v_{\mathrm{ref},0}\right)^T \mathbb{W}_{v_{\mathrm{ref}}} \left(v_{\mathrm{ref}} - v_{\mathrm{ref},0}\right) + \mathcal{R}, \end{aligned} \tag{3.6}$$

Here, the starred variables T^*, S^* and v^* denote the measurements of temperature, salinity and velocity, respectively. The linear interpolation operators Φ_T, Φ_S and Φ_v map the model variables temperature T, salinity S and velocity v to the corresponding data location. The third term in equation 3.6 which is actually the sum of two symmetric covariance terms, allows for correlations between temperature and salinity. The model-data misfit is weighted by the weighting matrices $\mathbb{W}_{T,S,TS,v}$ that are the inverse of the prior error covariances. Thus by defining the objective function $\mathcal{J}$, we compare the model variables T, S and v to the measurements, and at the same time weight the differences by the matrices the inverses of the individual measurement errors.

In the fifth term, the model velocity at a chosen reference level v_{ref} is compared to the prior assumption $v_{\mathrm{ref},0} = 0\,\mathrm{m\,s^{-1}}$. Here, the reference level was chosen to be the ocean bottom. This approximation is assumed to be valid within a certain error range that is reflected in the weights $\mathbb{W}_{v_{\mathrm{ref}}}$ and allows for deviations from these prescribed zero reference velocities.

The "regularization" term $\mathcal{R}$ allows for penalizing the roughness of the solution by requiring the horizontal gradients of the model variables to be small.

$$\mathcal{R} = \frac{1}{2}\left(\frac{\partial v}{\partial x}\right)^T \mathbb{W}_r^{(v)} \left(\frac{\partial v}{\partial x}\right) + \frac{1}{2}\left(\frac{\partial T}{\partial x}\right)^T \mathbb{W}_r^{(T)} \left(\frac{\partial T}{\partial x}\right) + \frac{1}{2}\left(\frac{\partial S}{\partial x}\right)^T \mathbb{W}_r^{(S)} \left(\frac{\partial S}{\partial x}\right), \tag{3.7}$$

Here, x is the horizontal space coordinate along the section (approximately meridional), and $\mathbb{W}_r^{\{(v),(T),(S)\}}$ are the smoothness weights for the respective variables. These weights are determined by the dimensionless parameters $\{T, S, v\}_{\mathrm{rough}}$ describing smoothness or roughness of the respective field. These parameters cannot be measured and are uniform on the model domain. They can only be guessed by inspection of the model result, see next section (3.1.4).

The optimal solution that minimizes (3.6) is found by a BFGS quasi-Newton algorithm as implemented by Kelley (1999), see also appendix N.1. The physical equations are optionally discretized by the finite element or finite volume method. Two different basis functions for velocity can be chosen in the case of finite elements.

FEMSECT also provides the possibility of transport calculations of volume and heat across the section, including an error estimation.

3.1.4 Choice of parameters

FEMSECT offers many possibilities, thus a lot of decisions have to be taken before running the model. Out of the three different discretization methods, the Finite Element method with piecewise constant basis functions for velocity was chosen for this study. As described in Losch et al. (2005), this method provides the most accurate results.

The number of iterations is set to 5000 as all the experiments and observations of the model's behaviour suggest that there is no further significant change in the results for larger numbers. This is true for the velocity field as well as for the decrease of the cost function.

Slanted triangles that occur due to complex bottom topography possibly disturb the correct calculation. For example roughness parameters are used only in horizontal direction which causes problems if node depths do not coincide. Therefore a routine is applied to eliminate these triangles.

Temperature and salinity data from the WOCE hydrography are used to model a 2 months mean for January/February 1994. The data can be downloaded from `http://cchdo.ucsd.edu/data_access/show_cruise?ExpoCode=09AR9407_1`. However, the data do not represent the true mean but are derived from single measurements. That needs to be accounted for in the error description.

For estimation of data variance, model output from the "cube78" run of the Ecco2 project (Menemenlis et al., 2005) is deployed. The data is freely available on (`http://ecco2.org`). The hydrographic model output is investigated for the target region and during the specified time period. However, the modelled hydrographic standard deviations are very small and include neither temporal variability on all time scales nor modelling errors. Therefore they are increased by a constant factor in the FEMSECT model run to properly account for these issues as well as for non-synopticity of the in-situ data. The vertical covariances for temperature as well as salinity are calculated directly from the measurements and horizontal roughness parameters are used as weights in equation (3.7) to account for smoothness constraints.

Direct velocity measurements are very sparse for this section. As the data are used to represent a monthly mean, a prior error estimate of $0.01\,\mathrm{m\,s^{-1}}$ is applied, although instrument accuracy is much better than that. Bottom reference velocity errors are estimated to $0.05\,\mathrm{m\,s^{-1}}$ and $0.01\,\mathrm{m\,s^{-1}}$ for comparison, because of limited knowledge and large uncertainty in the abyssal.

The choice of the optimal roughness parameters is a trade-off. Hardly punishing roughness results in a quite realistic velocity field with nicely defined fronts and subcurrents. However, the westward countercurrent around Antarctica is missing completely. With increasing roughness parameter, this current becomes more and more distinct, but smoothness of the results increases so much that fronts merge and eddies disappear. Therefore the final choice of $T_{\mathrm{rough}} = 0.004\,\mathrm{K}$ and $S_{\mathrm{rough}} = 0.004\,\mathrm{PSU}$ is a compromise that does not smooth the velocity field completely and still shows a weak westward countercurrent.

3.2 Results with FEMSECT

In this section, the results computed with the FEMSECT model are presented. The posterior transport error estimates and the impact of the MDT data set are described. An overview of volume and heat transports is given and the current structure, including bottom currents, is investigated. Eventually, a new approach of including ocean surface velocities derived from sea ice drift data is presented.

3.2.1 Rifugio versus Intermod approach

The Rifugio approach of a combined MDT as described in section 2.4.2 cannot be applied to a section such as SR3. The geodetic estimate of the combined error covariance requires a two-dimensional surface of data points to support the computation. A single oceanic section is only a one-dimensional line on the ocean surface, for which the geodetic problem is ill-posed. Thus the computation of the combined MDT as described in section 2.4.2 is not possible and we are limited in our study to an investigation of different geoid error covariance models. The analysis of the combined approach is postponed to the higher-dimensional ocean models such as IFEOM (chapter 4).

Instead, the results of the project INTERMOD (Schuh and Becker, 2008) are used here. The INTERMOD solutions were developed and computed at the Institute of Geodesy and Geoinformation (IGG) at the University of Bonn and were made available to the AWI. In this approach, the modelled geoid error covariance is simply added onto an estimate of the altimetry error. The Hilbert space of Spherical Harmonics is divided into three subspaces named commission, transition and omission subspace. The commission subspace includes degrees from 2 to 150 and is determined by the measurements. In contrast, the omission subspace ranges from degree 181 up to infinity and can only be described by prior information. The transition subspace in between, covering degrees 151 to 180, is established by both the measurements and the prior assumptions. The prior information used in the transition and omission subspace is provided by Kaula's rule of thumb which describes the degree variances for degree l as $\sigma_l^2 = \frac{2l+1}{l^4} \cdot 10^{10}$. This, including some more theoretical background information, has been explained in section 2.4.1.

In the following, the outcome of this INTERMOD approach is used. Apart from the Reference case, we distinguish three different models for the geoid error covariance: Reference, EGM96, Transition and CompleteITG.

- **Reference**: Original FEMSECT without any MDT information.
  The other three cases use MDT data including MDT error information from different sources:

- **EGM96**: The error covariance matrix represents earlier geoid height error covariance information.
  The EGM96 geoid model is a set of spherical harmonic coefficients up to degree and order 360. The geoid height was computed from the harmonic coefficients explicitly for the application with satellite altimetry. However, the model's error covariance estimate is only complete to degree and order 70, therefore a

Gaussian filter is applied to remove all scales corresponding to a spherical harmonic degree higher than 70. The omission error is entirely neglected. More details concerning the geoid model EGM96 itself and regarding its application in oceanography can be found in Lemoine et al. (1997) and Losch and Schröter (2004), respectively. The data is available at `http://cddis.gsfc.nasa.gov/926/egm96/egm96.html`. The resulting MDT error covariance is singular. The inversion needed for weighting matrix computation is done via a Moore-Penrose pseudoinverse (see appendix N.2) with a singular value tolerance of $0.001\,\mathrm{m}^2$.

- **Transition**: The MDT error covariance matrix includes the transition zone error, but not the omission error.
  For degrees smaller than 70, it is based on EGM96. Thus it represents a transition between the two cases EGM96 and CompleteITG (see next item). Investigation of the singular values of this matrix results in a tolerance of $0.02\,\mathrm{m}^2$ in the Moore-Penrose pseudoinverse computation.

- **CompleteITG**: The MDT error covariance matrix includes the transition zone as well as the omission error. The covariance matrix has a finite condition number of 82.9, therefore it is directly invertible.

Figure 3.2 shows the different covariance matrices. Error variances of the CompleteITG error model are higher than in the other two error models and the covariance structure is more pronounced. This is due to consideration of transition and omission error. Almost all singular values are larger than 10^{-2} which facilitates matrix inversion. In contrast, the EGM96 error covariance is very smooth and has a high number of negligibly small singular values which make direct matrix inversion impossible.

These different error models are applied to an MDT estimate based on the static GRACE solution ITG-Grace03s (Mayer-Gürr, 2007) and altimetric data from Jason-1. The altimetry data set covers the years from 2002 to 2009 and was processed by Silvia Becker at the IGG. This MDT estimate is called "SAT" (Satellite-only) in the following. For comparison purposes, the INTERMOD MDT error estimate is also applied to the `CNES-CLS09_v1.0` MDT data. `MDT_CNES-CLS09` was produced by CLS Space Oceanography Division and distributed by Aviso, with support from Cnes[1] (http://www.aviso.oceanobs.com/). CNES-CLS09 already incorporates hydrographic and drifter data and is therefore very smooth. However, contributions from satellite and hydrographic data are not separable any more and an error covariance estimate is not provided. It is called "CLS09" MDT in the following.

[1]Centre National d'Etudes Spatiales, Paris, France

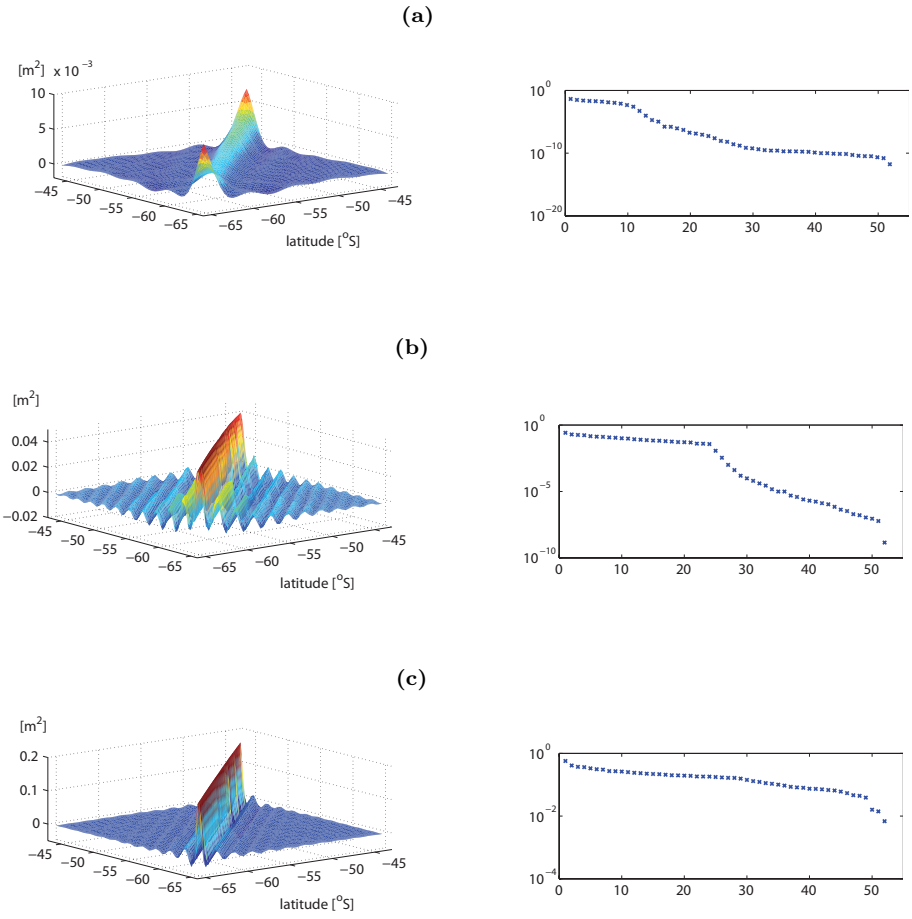

Fig. 3.2: Different geoid error covariance estimates and corresponding singular values in m^2: (a) EGM96 geoid model, (b) Transition model, (c) CompleteITG model. Note the different scales of the axes.

3.2.2 Posterior transport errors

The FEMSECT Reference run without any MDT data assimilation already results in good estimates of volume (159 Sv) and heat[2] (1.94 PW) transport across the SR3 section (see table 3.1). The FEMSECT model also provides formal posterior transport error estimates by an inversion of the Hessian matrix of the cost function $\mathcal{J}$ (Thacker, 1989, see also appendix N.3). These transport error estimates of 18 Sv and 0.27 PW, respectively, are very large in the Reference run. They are expected to decrease by the assimilation of additional information, e.g. MDT data, that renders the final estimate more accurate.

This is confirmed by all model runs that incorporate MDT data: without exception, all error estimates become smaller than the one of the Reference run (see table 3.1). The EGM96 model has no information about the error content beyond spherical harmonic degree 70 and therefore the corresponding error estimate is quite small. Adding information about the error structure successively by proceeding to the models Transition and CompleteITG, the posterior error increases again. This is shown in table 3.1 for two different MDT data sets and visualized in figure 3.3. We conclude that neglecting the omission error severely underestimates the true error. (Of course the latter is not accurately known, but believed to be better estimated by an approximation than by neglect.) This agrees with the findings of Losch et al. (2002b) concerning the error reduction achieved by adding variably accurate MDT information.

	Volume transport [Sv]	Heat transport [PW]	
Reference	159 ± 18	1.94 ± 0.27	
EGM96	148 ± 14	1.57 ± 0.21	SAT
Transition	156 ± 16	1.84 ± 0.25	
CompleteITG	159 ± 17	1.91 ± 0.26	
EGM96	169 ± 14	2.05 ± 0.21	CLS09
Transition	162 ± 16	1.97 ± 0.25	
CompleteITG	161 ± 17	1.96 ± 0.26	

Table 3.1: FEMSECT transports of volume in Sv and heat in PW across the WOCE SR3 section between Tasmania and Antarctica, including error estimates. The computation is based on in-situ data from 1994 and satellite observations from 2002-2009. The posterior errors depend only on the prior errors and are independent of the actual MDT data used.

[2]Strictly speaking, this is temperature transport relative to a reference temperature of 0 °C as the mass balance of the SR3 section is nonzero. We stick to the jargon of relative heat transports for convenience.

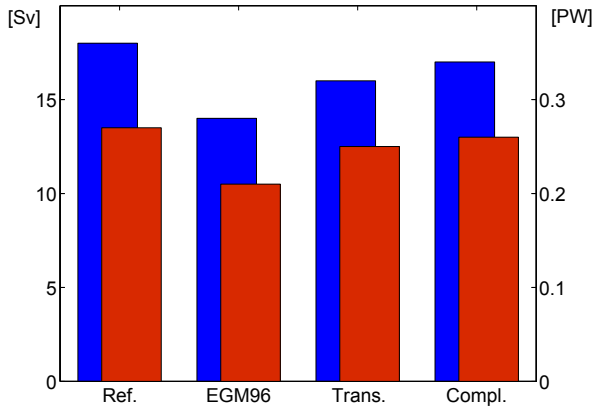

Fig. 3.3: Error estimates for FEMSECT transport of volume in Sv (blue) and heat in PW (red) across the WOCE SR3 section between Tasmania and Antarctica. The computation is based on in-situ data from 1994 and satellite observations from 2002-2009.

Although the posterior errors of the CompleteITG model are high (17 Sv and 0.26 PW), they are still below those of the Reference model run. This provides some confidence in the correctness of the model as additional information can only improve the accuracy of the estimate and therefore lead to smaller posterior errors.

3.2.3 Impact of MDT data set

Neglecting the omission error as in the EGM96 error model leads to an underestimation of the prior errors. Thus the corresponding weights are large and the model is forced to adjust closely to the MDT. Therefore we observe big differences in the transport estimates between the reference run and the two EGM96 runs. These deviations decrease as the omission error model is refined. In the CompleteITG case, the assumed prior error is larger due to consideration of the omission part. Therefore the MDT weights are smaller and the resulting transports resemble each other.

The SAT MDT leads to much lower transports of volume and heat than the combined CLS09 MDT data does. This can be explained by a very crude approximation: The transport across the section is approximately proportional to the MDT difference between the end points of the section. For the SR3 section, the CLS09 estimate and the SAT estimate result in

$$\begin{aligned} \mathrm{MDT}_{\mathrm{CLS09}}(44.0°\mathrm{S}) - \mathrm{MDT}_{\mathrm{CLS09}}(65.8°\mathrm{S}) &= 1.69\,\mathrm{m} \quad \text{and} \\ \mathrm{MDT}_{\mathrm{SAT}}(44.0°\mathrm{S}) - \mathrm{MDT}_{\mathrm{SAT}}(65.8°\mathrm{S}) &= 0.89\,\mathrm{m}. \end{aligned}$$

This explains the large difference between the transports in the EGM96 model run.

The rule of thumb for the transport difference

$$\Delta\mathrm{Transp} = \frac{g}{f}\Delta\eta\mathrm{H}$$

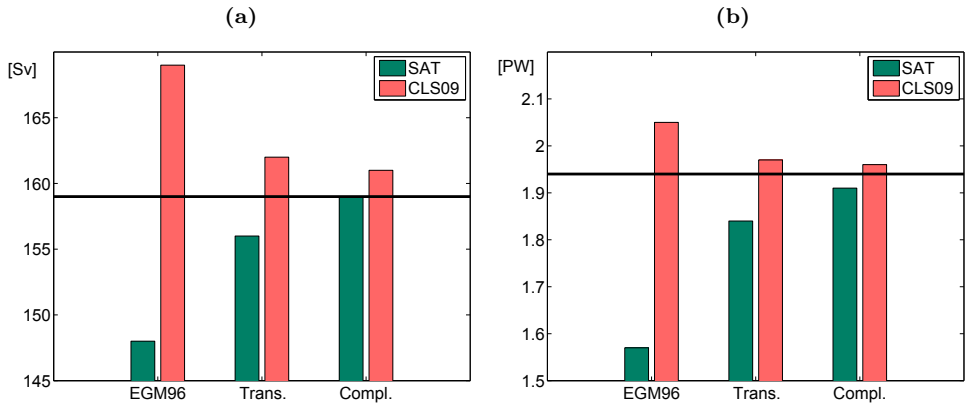

Fig. 3.4: FEMSECT transport estimates across the WOCE SR3 section between Tasmania and Antarctica for different omission error models and different altimetric data: (a) Volume transport, (b) Heat transport. The computation is based on in-situ data from 1994 and satellite observations from 2002-2009. The bold black line denotes the transport of the Reference model run without MDT.

with a representative depth H as presented in Losch (2001) is not applicable to full extent to the FEMSECT model. With H$\approx$ 2500 m, the estimated transport difference would be

$$\Delta\text{Transp} \approx \frac{10}{10^{-4}} \cdot 8 \cdot 10^{-1} \cdot 2.5 \cdot 10^{3}\,\text{m}^3\,\text{s}^{-1} = 200\,\text{Sv}.$$

This high value of transport difference is not reproduced in the FEMSECT model run which gives at most 21 Sv for the EGM96 case. This is mainly due to the reference velocity constraint that induces baroclinic velocities which are not considered in the rule of thumb.

Repeating the calculation of MDT difference between the fourth and the last but three grid points of the section results in

$$\begin{aligned} \text{MDT}_{\text{CLS09}}(44.7^\circ\text{S}) - \text{MDT}_{\text{CLS09}}(65.4^\circ\text{S}) &= 1.67\,\text{m} \quad \text{and} \\ \text{MDT}_{\text{SAT}}(44.7^\circ\text{S}) - \text{MDT}_{\text{SAT}}(65.4^\circ\text{S}) &= 1.70\,\text{m}. \end{aligned}$$

The estimated difference is now higher in the SAT approach. This might be due to boundary effects that are not adequately described by the prior errors yet, but more likely a general matter of resolution as explained in the following.

The distance between the first and the fourth grid point from the section boundaries amounts to

$$\begin{aligned} \text{distance}(44.0^\circ\text{S} - 44.7^\circ\text{S}) &= 83\,\text{km} \quad \text{and} \\ \text{distance}(65.4^\circ\text{S} - 65.8^\circ\text{S}) &= 45\,\text{km}, \end{aligned}$$

respectively. This is far below the precision of GRACE which has a footprint of about 10^6 km^2 (Wahr et al., 2006) and whose captured spatial scales are limited by roughly

$$20000\,\text{km}/\text{spherical harmonics degree} = 20000\,\text{km}/180 = 111\,\text{km}$$

(Knudsen et al., 2011). As GRACE data describe a large-scale average, we cannot trust the value of a single grid point as a point value in our sub-resolution ocean model FEMSECT. The low posterior transports presented in figure 3.4 are not reliable. This deficiency in precision has to be accounted for in the error description. In contrast, the CLS09 MDT was obtained at a resolution of 1/4° by the inclusion of in-situ data.

The different MDT data sets are compared in figure 3.5. The CLS09 MDT estimate incorporates hydrographic data and is therefore already close to the FEMSECT reference run MDT. The satellite-only MDT is less smooth as it cannot be well represented on the small-scale ocean grid. The boundary issue described above becomes obvious.

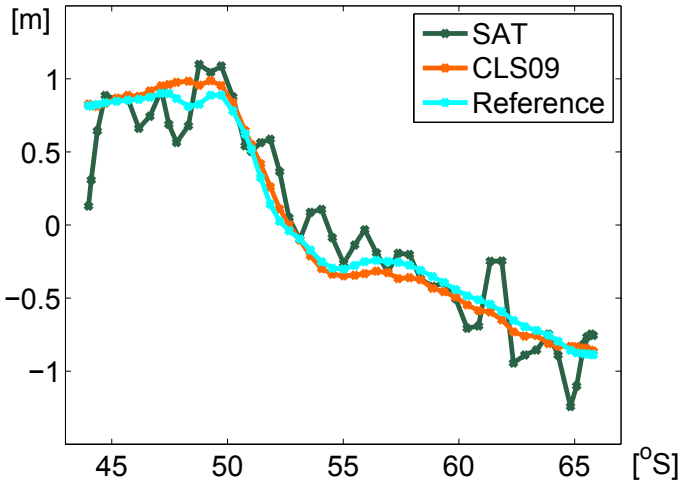

Fig. 3.5: Comparison of Reference MDT, SAT MDT and CLS09 MDT.

The scales of the geoid data and the ocean model FEMSECT do not agree. Therefore careless combination of these will lead to remarkable errors. Before assimilation into the small-scale ocean model, the small-scale part of the geoid data can be refined by the help of other data sources as was done in the CLS09 model. Otherwise the amount of information it contains for our simple ocean model is very limited. The resulting large prior error will downweight the large-scale MDT data and let other terms such as in-situ measurements, smoothness constraint and reference velocities dominate the solution.

On the other hand, FEMSECT produces a new small-scale MDT that has taken the large-scale satellite-only MDT data into account. This is an elegant way of "interpolating" the satellite MDT data set, accounting for hydrographic data as well as for physical constraints in the ocean. However, due to the large errors in the MDT data, the FEMSECT reference MDT hardly experiences any changes if a rea-

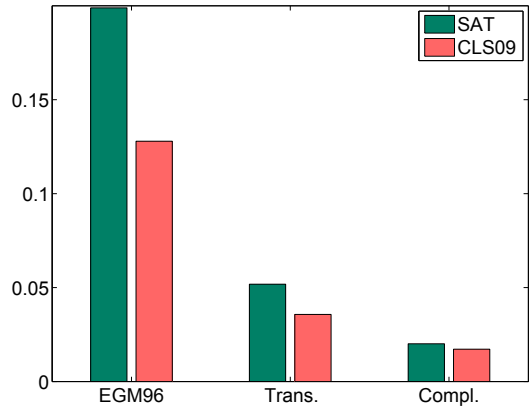

Fig. 3.6: Average FEMSECT MDT deviations in m from the Reference run MDT.

listic MDT error description is applied. This is shown in figure 3.6 by means of the FEMSECT MDT deviations from the Reference run MDT. The small errors of the EGM96 estimate cause a considerable deviation from the MDT of the Reference run. This is reduced to a large extent by the Transition domain error model already. In the CompleteITG estimate, the MDT data has only little influence on the model solution.

3.2.4 Posterior volume and heat transports

The FEMSECT Reference run and the CompleteITG models SAT and CLS09 are compared to other estimates in terms of volume and heat transports. As shown in figure 3.7a, the results agree with all other volume transport estimates presented here within errorbars.

A comparison of heat transports is presented in figure 3.7b. The variability of the estimates of heat transport is large, reflecting the high variability of the Antarctic Circumpolar Current system. The FEMSECT estimates are comparatively high, but agree with most of the other estimates within errorbars.

Of course, the good agreement of both volume and heat transports is partly due to the large posterior FEMSECT error estimates. Reduction of this formal error however requires more accurate knowledge about the omission error (see section 3.2.2).

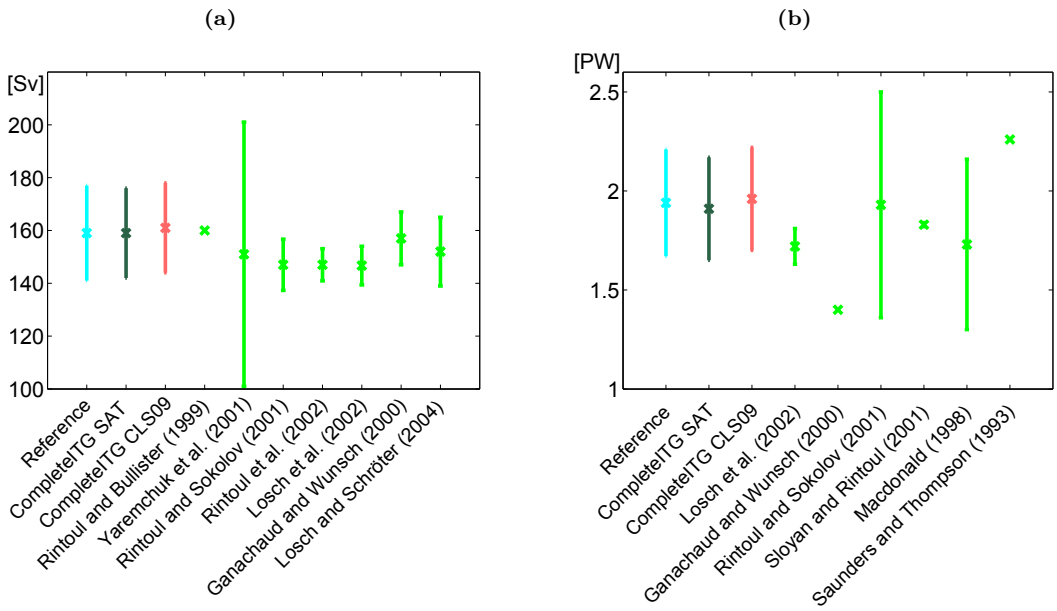

Fig. 3.7: Comparison of transport estimates to those of other authors: (a) Volume transports, (b) Heat transports.

3.2.5 FEMSECT currents

FEMSECT reproduces all commonly known fronts and features in the current system across the SR3 section. From north to south these are (see also figure 3.8)

- the westward Tasman outflow (TAS) directly south of Tasmania,
- the subantarctic zone recirculation (SAZ) which is rather smooth here,
- a cold core ring (CCR) or meander, a typical feature in this region,
- the Subantarctic front (SAF), extending from the surface to the seafloor,
- the Polar front (PF) whose northern branch is not distinctly separated from the SAF,
- a westward flow south of the mid-ocean ridge, called South of SAF (SSAF),
- the broad southern branch of the Polar front,
- the southern ACC front, split into Southern Front (SF) and Southern Boundary (SB),
- the westward Antarctic slope front (ASF).

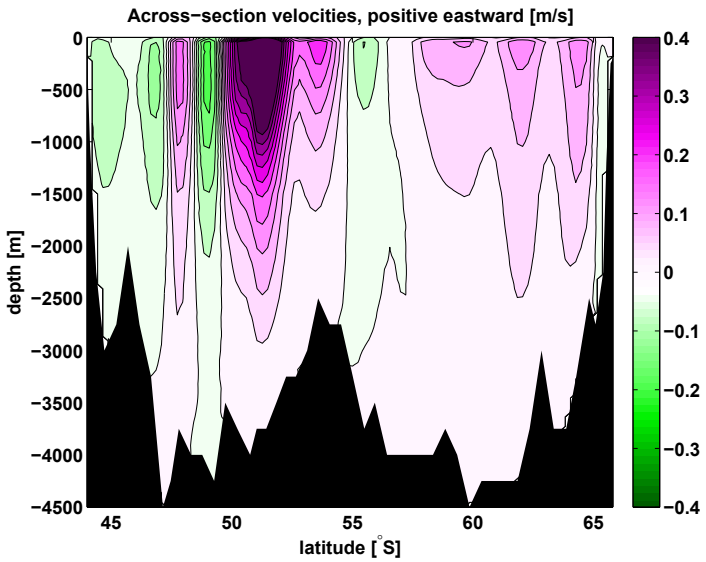

Fig. 3.8: Across-section velocities of the FEMSECT Reference run. All commonly known fronts can be identified.

Most of the eastward ACC transport is done by the SAF and PF, as also found by Rintoul and Bullister (1999). The westward flow over the southern flank of the mid-ocean ridge system, the SSAF, is a persisting feature. It results from the eastward flowing ACC south of this latitude turning north over rising bottom topography and back across the hydrographic section, crossing the mid-ocean ridge west of the section (Yaremchuk et al., 2001).

For our choice of parameters (see section 3.1.4), the FEMSECT results for the different geoid error models and different MDTs resemble each other very much, as shown in figure 3.9. The largest differences however are within the error estimates. This result was expected as the FEMSECT Reference run already provides a reasonable current structure and good estimates of volume and heat transports as shown in section 3.2.4. Unfortunately, the large formal posterior errors can hardly be reduced if the MDT error estimate is deduced carefully. In the CompleteITG model that considers the omission error, the expected error reduction is much less than assumed by a crude error model. This is in good agreement with Losch et al. (2002b).

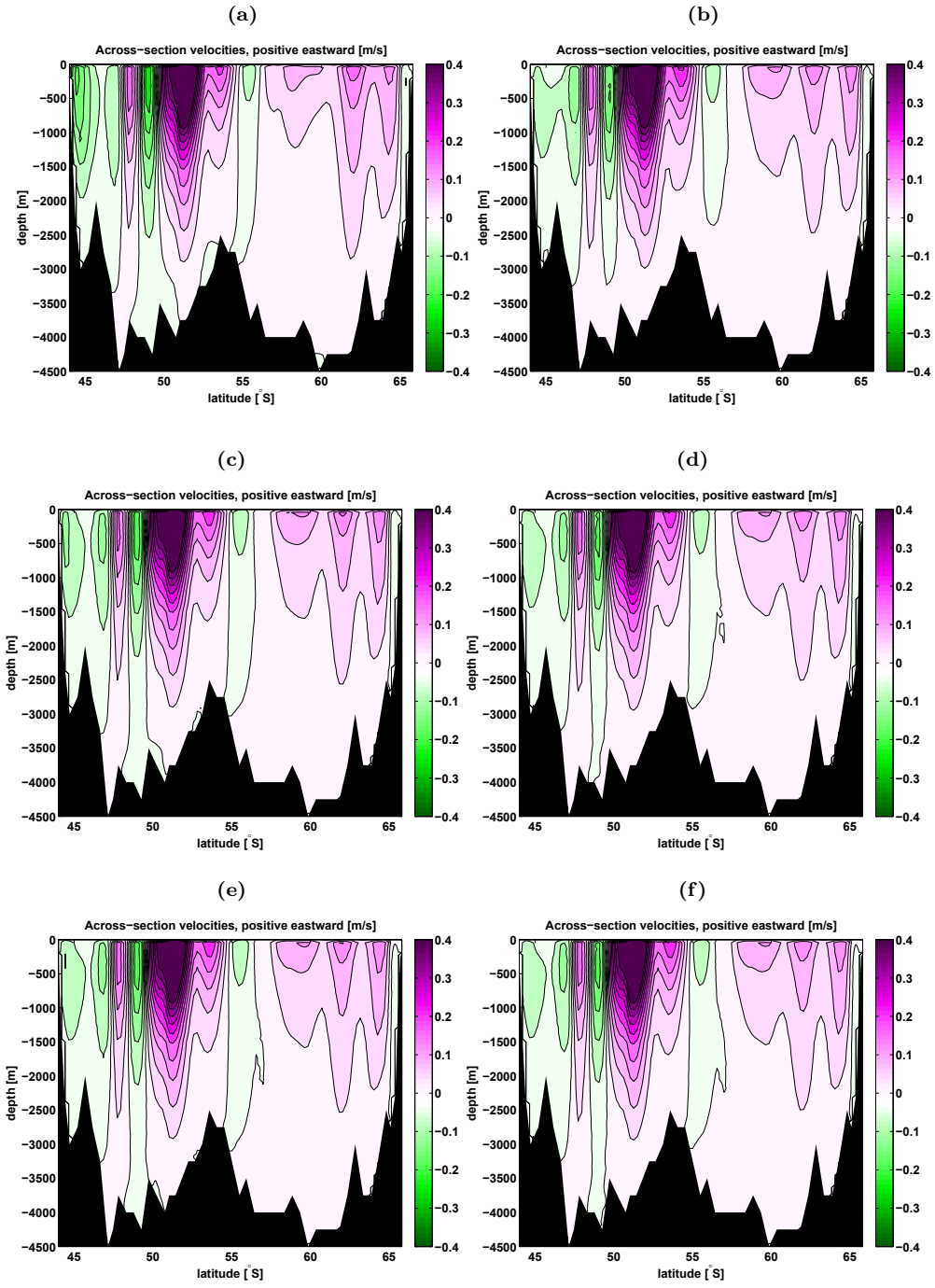

Fig. 3.9: Across-section velocities of FEMSECT results with different geoid error models with SAT MDT (left) and with CLS09 MDT (right): (a) EGM96 SAT, (b) EGM96 CLS09, (c) Transition SAT, (d) Transition CLS09, (e) CompleteITG SAT, (f) CompleteITG CLS09. In some areas of the model region, differences are so small that numerical difficulties arise. Therefore difference plots are not shown here.

3.2.6 Bottom velocities

The MDT data constrains the model solution by imposing geostrophic velocities at the ocean surface. The equivalent is done at the ocean bottom by the reference velocities. Usually it is assumed that abyssal velocities are close to zero which is a reasonable assumption in many regions of the world ocean. However, there are almost no measurements of abyssal velocities, so we must apply some error estimate that allows for more or less small deviations from zero. All the previous FEMSECT model runs use a small reference velocity error of $0.01\,\mathrm{m\,s^{-1}}$. This results in high weights for the zero reference velocities and thus represents a strong constraint on the ocean circulation.

Due to very limited knowledge about the abyssal circulation, we can as well apply a larger reference velocity error estimate of $0.05\,\mathrm{m\,s^{-1}}$. This gives more freedom to the bottom velocities and thus influences the whole water column. The FEMSECT Reference run without MDT displays only marginal changes due to the modified reference velocity errors. In combination with the SAT MDT data, a westward countercurrent appears at the ocean bottom at the northern slope of the South East Indian Ridge (between 48°S and 55°S). It is strongest in the EGM96 model run when a lot of weight is put on the MDT data and weaker in the other cases, but still present even in the Complete model run shown in figure 3.10.

The reason for its occurrence can be found in the MDT data set itself, see figure 3.5. The largest differences between the SAT MDT and the CLS09 MDT can be observed at about 48°S, 51°S, 54°S and 62°S. Via the principle of geostrophy, equation 3.5, the SAT MDT induces an increased westward flow (or a reduced eastward flow) at each of these latitudes, with accelerated eastward flow directly south of it. For the FEMSECT model runs from the previous section (with reference velocity errors of $0.01\,\mathrm{m\,s^{-1}}$), this is apparent comparing figures 3.9a and 3.9b. When the MDT error description is refined (Transition and CompleteITG model runs), the MDT data has not enough impact on the solution to evoke these subtle distinctions.

Releasing the reference velocity error to $0.05\,\mathrm{m\,s^{-1}}$ gives more freedom to the model and therefore the changes by the MDT data are also visible in the CompleteITG model run. The rough MDT increases velocities at some latitudes and decreases them at others. When the eastward surface velocity is decreased and the velocity shear throughout the water column is kept constant by the density field, then the bottom velocity will be decreased as well and may even become negative (westward). This happens here between 48°S and 55°S.

As mentioned before, the MDT cannot be represented accurately at the small scales of the ocean model. On the one hand, the SAT MDT suffers from lack of small-scale information and thus presumably also from numerical effects causing the oscillations in the data. On the other hand, the CLS09 MDT is to a large extent determined by hydrography and thus does not represent independent observations. Therefore its gain of information for the ocean model must be questioned. Hence a judgement about the quality of the data or the model is not possible at the current stage of research.

The westward undercurrent was also reported by Yaremchuk et al. (2001). They note a significant countercurrent in the bottom 1000 m directly beneath the main part

of the SAF between 48°S and 52°S. It results from a constraint on the tracer balance and current meter data at shallower levels.

Phillips and Rintoul (2000) also show the existence of a bottom countercurrent at the northern edge of the SAF, approximately 50 km north of the velocity peak. They describe the deep velocity profiles as quite different to the shallow ones which is presumably the result of interaction with the sea floor.

In contrast, Losch and Schröter (2004) deny the existence of this undercurrent, refering to Rintoul and Sokolov (2001) and the generally accepted notion of a deep-reaching ACC. However, the countercurrent is also present in their model results when a MDT estimate is assimilated. Rintoul and Sokolov (2001) indeed approve the assumption of a deep level of no motion for geostrophic calculations, but also note the possibility of significant barotropic flow. Until now, there are no direct observations available to support or disprove the statement. The FEMSECT model however allows the deep westward velocities if they are not explicitly constrained.

The issue of circulation in the abyssal ocean still raises a lot of questions. We will not be able to answer them within the framework of this study and suggest further investigations be done about the detailed structure of these (deep) current systems.

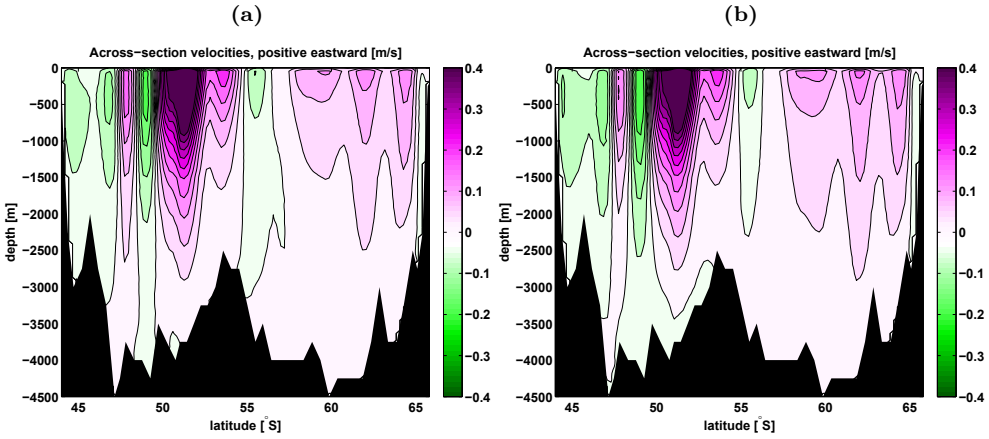

Fig. 3.10: Across-section velocities of FEMSECT results with large reference velocity errors: (a) Reference run, (b) Complete SAT.

3.2.7 Ocean velocities from sea ice drift

In polar regions, weather conditions are hostile, particularly in winter. In-situ measurements are often hard or impossible to obtain. Therefore, these areas, which are of outstanding importance for modelling and research, suffer from undersampling (Minster, 1995).

For engineering reasons, Earth observing satellites are preferably sent on a sun-synchronous orbit which leaves a polar gap without satellite data (Sneeuw and van Gelderen, 1997). Furthermore, altimetric measurements of sea surface height fail in the presence of sea-ice (Silvia Becker, pers. comm.). Both issues do not apply for the SR3 section as it does not reach far enough south and is hardly covered by sea ice. However, if the Fram Strait situated at about 80°N or the prime meridian in the Southern Ocean is to be investigated by the FEMSECT model, these considerations will be important.

The investigations presented in this section therefore only concern the southernmost part of the SR3 section where a small amount of sea ice is present. The method is applied to the FEMSECT model which is already running well in order to analyse the effects and the potential benefit of the approach. The actual gain of the method may only become obvious when applied to other region in the ocean.

In this approach, we try to benefit from the idea that velocity and direction of sea ice drift must be partly dependent on the surface circulation in the ocean. Thus we derive new surface reference velocity information for the ocean model from satellite observations of sea ice drift.

3.2.7.1 Method and data

Sea ice drift is to a large extent determined by the wind field. To examine the relationship between sea ice motion, wind field and ocean currents, a linear formula following Kimura (2004) is used. This rule was adopted from Thorndike and Colony (1982) and relates sea ice velocity (U,V), wind velocity (u,v) and mean ocean current $(\bar{c_u}, \bar{c_v})$ via:

$$\begin{bmatrix} \bar{c_u} \\ \bar{c_v} \end{bmatrix} = \begin{bmatrix} \bar{U} \\ \bar{V} \end{bmatrix} - F \cdot \begin{bmatrix} \cos\theta & -\sin\theta \\ \sin\theta & \cos\theta \end{bmatrix} \begin{bmatrix} \bar{u} \\ \bar{v} \end{bmatrix} \tag{3.8}$$

with turning angle θ and speed reduction factor F. Thorndike and Colony (1982) show that equation (3.8) is a reasonable approximation to the balance of forces on sea ice in geostrophic equilibrium in the absence of internal stress gradients and inertial effects. Optimum values for turning angle θ and speed reduction factor F are calculated by a least squares technique following Kimura and Wakatsuchi (2000):

$$\begin{aligned} \theta &= \arctan\left[\frac{\sum u'V' - \sum v'U'}{\sum u'U' + \sum v'V'}\right] \\ F &= \frac{c_1 + c_2 - c_3 + c_4}{\sum u'^2 + \sum v'^2} \end{aligned} \tag{3.9}$$

where

$$c_1 = \cos\theta \sum u'U', \quad c_2 = \sin\theta \sum v'U',$$

$$c_3 = \sin\theta \sum u'V', \quad c_4 = \cos\theta \sum v'V'.$$

Here, $\bar{u}$, $\bar{v}$, $\bar{U}$, $\bar{V}$ denote the mean values of u, v, U, V, and u', v', U', V' the respective anomalies defined by $(u - \bar{u})$, $(v - \bar{v})$, $(U - \bar{U})$, $(V - \bar{V})$. Time variations of θ, F, and $(\bar{c_u}, \bar{c_v})$ are assumed to be negligible.

For this study, ice drift data from Fowler (2003) was used, the respective mean ice drift data is presented in figure 3.11a. The daily gridded fields combine data from Advanced Very High Resolution Radiometer (AVHRR), Scanning Multichannel Microwave Radiometer (SMMR), Special Sensor Microwave/Imager (SSM/I) and the International Arctic Buoy Programme (IABP). Version 1 is available online at `http://nsidc.org/data/nsidc-0116.html`. For representation of the wind field, NCEP Reanalysis data was used, the respective mean is shown in figure 3.11b. The data set was provided by the NOAA/OAR/ESRL PSD, Boulder, Colorado, USA and can be downloaded from their Web site `http://www.esrl.noaa.gov/psd/`.

3.2.7.2 Results

By applying equation (3.8) to ice drift and wind data, sea surface currents for the southernmost part of the section are obtained and shown in figure 3.11c. Only very little sea ice is observed, flowing southwestwards. A strong mean wind field is blowing mainly southeastwards, exept close to the Antarctic coast where the direction is opposite. (This part is shown in the figure.) Resulting ocean surface currents are directed towards the Southwest.

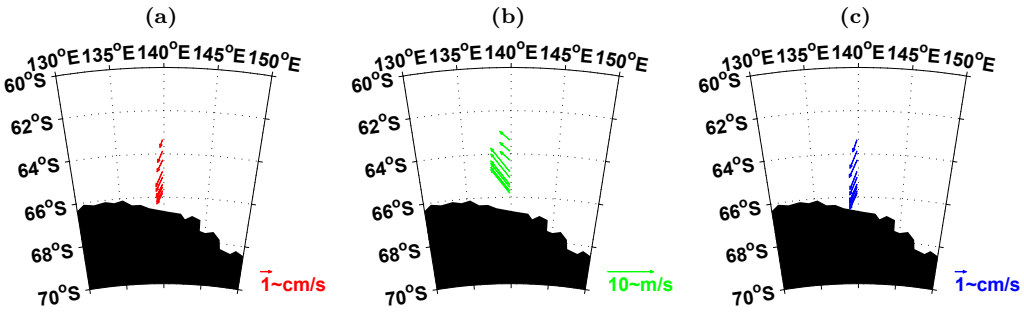

Fig. 3.11: Ice drift approach according to formula (3.8) in the southernmost part of the SR3 section: (a) Mean ice drift data $(\bar{U}, \bar{V})$, (b) Mean wind data $(\bar{u}, \bar{v})$, (c) Resulting ocean surface currents $(\bar{c_u}, \bar{c_v})$.

These surface currents are now incorporated into the FEMSECT model. As the sea ice covers only a small part of the SR3 section, only limited modifications to the overall circulation are expected. However, interesting effects can be noticed when assimilating the new data set.

The impact of the sea ice drift derived ocean surface velocities on the FEMSECT solution clearly depends on the assumed (bottom) reference velocity errors. If the latter are chosen to be small (e.g. $0.01\,\mathrm{m\,s^{-1}}$), the FEMSECT model cannot depart

CompleteITG model run	Volume transport [Sv] $W = 0\,s^2\,m^{-2}$	Volume transport [Sv] $W = 400\,s^2\,m^{-2}$	Volume transport [Sv] $W = 625\,s^2\,m^{-2}$
SAT, $\Delta v_{ref} = 0.01\,m\,s^{-1}$	159	155	153
SAT, $\Delta v_{ref} = 0.05\,m\,s^{-1}$	156	137	133
CLS09, $\Delta v_{ref} = 0.05\,m\,s^{-1}$	174	156	150

Table 3.2: Results from FEMSECT for SR3 section. $W = 400\,s^2\,m^{-2}$ and $W=625\,s^2\,m^{-2}$ are the weights that were used for the sea ice drift derived surface velocities. $W = 0\,s^2\,m^{-2}$ means no sea ice drift derived velocities were assimilated.

too much from this constraint and the solution is only changed to a small extent. If in contrast large reference velocity errors (e.g. $0.05\,m\,s^{-1}$) are assumed, the solution can adapt much more to the additional information in the sea ice drift data (compare table 3.2 and also figures 3.12a and 3.12b). In this case, the westward Antarctic slope front (ASF) is enforced and forms an undercurrent below the Southern Boundary (SB).

The increase of the westward countercurrent results in decreased absolute eastward volume transports (table 3.2). The decrease can be as much as 24 Sv when a weight of $625\,s^2\,m^{-2}$ is applied for the sea-ice drift derived ocean surface velocities and the reference velocities are assumed to be large. This might be of benefit in the common situation that assimilating geodetic MDT data causes unrealistically high transports in the Southern Ocean (Griesel et al. (2010), Martin Losch, pers. comm.). The reason for this phenomenon is still unclear. In our model this happens for the assimilation of the CLS09 data set, see table 3.2. When a small reference velocity error of $0.01\,m\,s^{-1}$ is applied, the model has not much freedom to adjust to the MDT data. In contrast, applying a reference velocity error of $0.05\,m\,s^{-1}$ uncovers the tendency towards increased transports which is then counteracted by the ice drift derived velocities.

Unlike the volume transports, the heat transports are hardly affected by the sea-ice drift data assimilation (and therefore not presented in this section). Only very little heat is transported along the southernmost fronts of the ACC. Therefore it would be interesting to apply the method to regions where sea ice reaches further northwards or even to latitudinal sections as the most important transport of heat is happening in north-south direction.

However, at the current state of research it is very difficult to estimate the ice motion error (Kimura, 2004). For this study, the rough estimates of $0.05\,m\,s^{-1}$ and $0.04\,m\,s^{-1}$ were applied, resulting in the constant diagonal weights $W=400\,s^2\,m^{-2}$ and $W=625\,s^2\,m^{-2}$, respectively. This is slightly more than the estimates given in the description of the dataset by Fowler (2003) in order to account for the wind speed error. The wind speed error is almost negligible due to the large value of the speed reduction factor F in equations (3.8) and (3.9). Unfortunately, no information about the error covariances is available for any of the two datasets. The importance of precise knowledge of the data errors is reflected in table 3.2 which shows that smaller errors

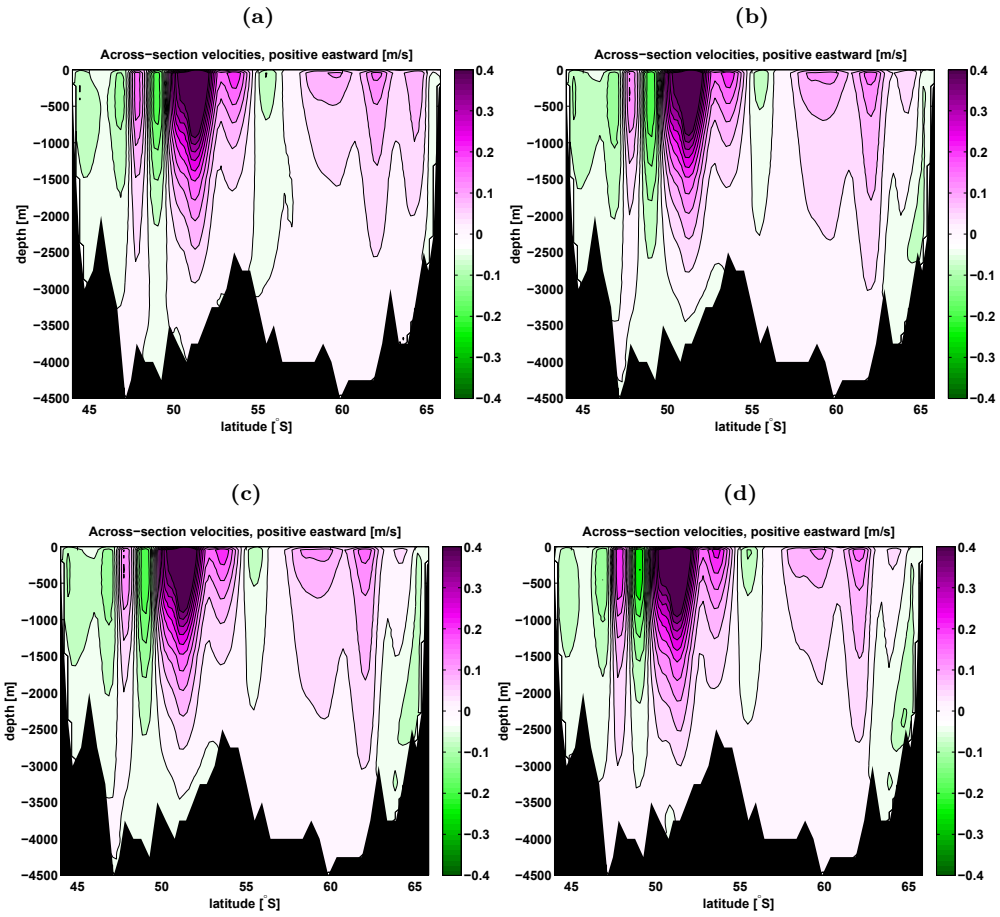

Fig. 3.12: Across-section velocities of FEMSECT results with ice drift and wind data, CompleteITG error model, different weights applied: (a) SAT with small reference velocity errors, W=400 s^2m^{-2}, (b) SAT with large reference velocity errors, W=400 s^2m^{-2}, (c) SAT with large reference velocity errors, W=625 s^2m^{-2}, (d) CLS09 with large reference velocity errors, W=625 s^2m^{-2}. Compare also table 3.2.

and therefore increased weights lead to more modifications of the results. Compare also figures 3.12b and 3.12c.

Due to the small amount of sea ice in the SR3 section and to the uncertainty of the data errors, this approach is not able to reduce the final FEMSECT error estimates. The wind field data are a model output by themselves, and the linear relationship of equation (3.8) might not always apply, leading to potential errors that are not modelled here. Still, the results of this section suggest that this method has some value when transports amplified by geodetic data become an issue. It could be a way to constrain the model against the biased information of the MDT data without assuming very small errors for unknown bottom reference velocities.

3.2.8 Summary and conclusions: FEMSECT

FEMSECT is a two-dimensional stationary ocean model with simplified physics. It permits assimilation of various data sets such as hydrographic data, direct velocity measurements and satellite data. In this study, it is applied to the SR3 section, although it is general enough to be used anywhere in the ocean where geostrophy applies (see section 3.1.1). FEMSECT provides estimates of volume and heat transport across the section. A formal error estimate is provided as well by inversion of the Hessian matrix of the cost function.

FEMSECT is sensitive to a couple of parameters (section 3.1.4). Choosing these parameters carefully results in a reasonable cross-section circulation and transports that compare well with estimates of other authors (sections 3.2.4 and 3.2.5).

Due to the two-dimensional structure of the model, the application of the Rifugio approach to FEMSECT is not possible (section 3.2.1). Instead, the INTERMOD approach (see section 2.4.1) is used and three different MDT error covariance models are analysed and compared to each other. A refined omission error model leads to a larger error estimate. It is shown that neglecting the omission error underestimates the true error (section 3.2.2).

Two MDT data sets are analysed within this study. The satellite-only MDT (SAT) effects smaller across-section transports when it is weighted heavily in the optimization process. In contrast, the combined CLS09 MDT results in higher transports as it is generally the case for geodetic MDTs in the Southern Ocean. This is the first of the three main problems that could be identified.

The second one is the choice of the reference velocities (section 3.2.6). Hydrographic measurements provide only the shear of the velocity field, and the depth independent part is determined solely by absolute velocity measurements, the MDT data and the reference velocities. Unfortunately, the latter are unknown, although assumed to be small. This results in large uncertainties in the abyssal circulation.

These two issues can be fixed by including surface reference velocities derived from sea ice drift data (section 3.2.7). As a new approach, the application of Kimura's (2004) method for estimating surface velocities from sea ice drift data is proposed to get more reliable (surface) reference velocities. However, this method is rather crude and does not readily provide us with a velocity error estimate. Therefore, either from refinement of the method or from other approaches of incorporating sea ice drift data, large improvements can be expected for the supplement of MDT data by ice drift information.

The third problem is a resolution issue. The FEMSECT model grid is very fine compared to the MDT data. Satellite-only data of the MDT is limited by the resolution of the geoid model. Therefore, scales of the SAT MDT differ from those of the ocean model and cannot be well represented in terms of the ocean model grid. Nevertheless, given an appropriate error description, the MDT data can be used for assimilation into ocean models. However, solving this problem to full extent would mean improving the resolution of the observational data. The resolution is not an issue for the combined CLS09 MDT, because for its calculation additional hydrographic

(in-situ) information was used. However, this is not necessarily a gain in information, because the CLS09 MDT is not independent data.

The simple ocean model FEMSECT already teaches a lot about inverse modelling. Valuable data has to be imported and a fair amount of prior knowledge has to be brought in to get some new information out of the model. The weighting is most critical and the error (co)variance models are of highest importance for the model output. A formal error estimate being provided, the gain of information for the model from new data sets can be quantified. Still, independent validation of the results is necessary.

In summary, the MDT data set seems to be of great benefit at a first glance; however, a refined error estimate decreases its impact. As a new way of approaching two of the common problems in our field of study, Kimura's (2004) method for estimating surface velocities from sea ice drift data was proposed. Clearly, data resolution is another important issue for the modelling process. While the geoid can be determined quite accurately on large scales (Shum et al., 2011), the application to comparatively small scale ocean models is not straightforward. The analysis of this issue is investigated further in the following chapter.

Chapter 4

Combination of Ocean and MDT: IFEOM

4.1 The 3D model IFEOM

The **I**nverse **F**inite **E**lement **O**cean **M**odel IFEOM was derived by Sidorenko (2004) from a stationary version of the **F**inite **E**lement **O**cean **M**odel FEOM, (Danilov et al., 2004, 2005)). In its present configuration its three dimensional model grid in the North Atlantic reaches from 4°N to 80°N and is separated into 29 vertical layers. The surface mesh is displayed in figure 4.1. The Finite Element method allows for straightforward mesh adaption to the coastal regions as well as to the ocean bottom. For inverse methods, grid nodes can be located at observation locations (here a hydrographic atlas). This is the main advantage of the Finite Element method in the ocean modelling context.

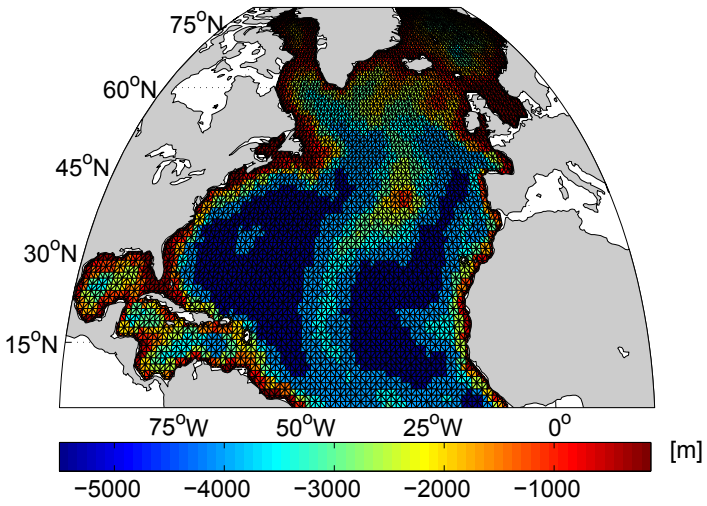

Fig. 4.1: IFEOM surface mesh. Colour indicates modelled ocean depth.

4.1.1 Model equations

The model consists of the vertically integrated steady momentum equations:

$$-fV - A_l\Delta U + gH\partial_x\eta + \frac{1}{\rho_0}\int_{-H}^{0}\partial_x p dz = \frac{\tau_x}{\rho_0} \quad (4.1)$$

$$fU - A_l\Delta V + gH\partial_y\eta + \frac{1}{\rho_0}\int_{-H}^{0}\partial_y p dz = \frac{\tau_y}{\rho_0} \quad (4.2)$$

$$\partial_x U + \partial_y V = 0 \quad (4.3)$$

$$\partial_z p = -g\rho \quad (4.4)$$

with the horizontal directions x and y, the barotropic transport vector (U, V), the sea surface height η, mean sea water density ρ_0 and the deviation from the mean density ρ. Pressure is denoted by p, the Coriolis parameter by $f = f(y)$ and the lateral momentum diffusion coefficient by A_l. The depth of the ocean bottom is $H = H(x, y)$ and the wind stress vector applied to the ocean surface is $\tau = (\tau_x, \tau_y)$, normalized by ρ_0. These equations are solved with boundary conditions

$$(U, V) = 0 \text{ on lateral rigid walls} \quad (4.5)$$

$$(U, V)\cdot\boldsymbol{n} = (U_{\mathrm{OB}}, V_{\mathrm{OB}})\cdot\boldsymbol{n} \text{ at the open boundary} \quad (4.6)$$

Here, $\boldsymbol{n}$ denotes the two dimensional normal at the boundary. The tangential component of the viscous stress is set to zero at the open boundary.

Now with η known, the 3D momentum equation with the vertical unit vector $\boldsymbol{k}$

$$f(\boldsymbol{k}\times\boldsymbol{u}) - \nabla\cdot A\nabla\boldsymbol{u} = -\frac{1}{\rho_0}\nabla p - g\nabla\eta \quad (4.7)$$

$$\text{and the continuity equation } \nabla\cdot\boldsymbol{u} = 0 \quad (4.8)$$

can be solved for the velocities $\boldsymbol{u} = (\boldsymbol{v}, w) = (u, v, w)$. The momentum diffusion coefficient is separated into a horizontal and a vertical part:

$$A = \begin{bmatrix} A_l & 0 & 0 \\ 0 & A_l & 0 \\ 0 & 0 & A_v \end{bmatrix}.$$

Boundary conditions are:

$$A_v\partial_z\boldsymbol{v} = \boldsymbol{\tau} \text{ at the surface} \quad (4.9)$$

$$A_v\partial_z\boldsymbol{v} + A_l(\nabla H\cdot\nabla)\boldsymbol{v} = 0 \text{ on the bottom and} \quad (4.10)$$

$$\text{at the lateral rigid walls} \quad (4.11)$$

$$\left(\int_{-H}^{0}\boldsymbol{v}dz\right)\cdot\boldsymbol{n} = (U_{\mathrm{OB}}, V_{\mathrm{OB}})\cdot\boldsymbol{n} \text{ at the open boundary} \quad (4.12)$$

For simplicity, these equations are formulated in Cartesian coordinates here (instead of spherical coordinates as in the model code) and in a non-stabilized form. Details according to the necessary stabilization can be found in Danilov et al. (2004).

This is the dynamical part of the model that is solved exactly, while the residuals of the thermodynamical part are minimized. The advection-diffusion equations for temperature and salinity are:

$$\boldsymbol{u}\nabla T + \nabla K \nabla T = \boldsymbol{\epsilon}_T \quad (4.13)$$

$$\boldsymbol{u}\nabla S + \nabla K \nabla S = \boldsymbol{\epsilon}_S \quad (4.14)$$

with diffusion coefficient

$$K = \begin{bmatrix} K_l & 0 & 0 \\ 0 & K_l & 0 \\ 0 & 0 & K_v \end{bmatrix}.$$

The residuals $\boldsymbol{\epsilon}_T$ and $\boldsymbol{\epsilon}_S$ represent physical processes that are not described by the model, first of all temporal evolution.

4.1.2 Boundary conditions

The IFEOM model accounts for momentum flux on the ocean surface but neglects bottom friction. The model domain is enclosed by rigid walls along all the Western, Northern and Eastern boundaries. This represents a severe restriction to the model and a crucial departure from reality. Surrounding the North Atlantic Ocean by rigid lateral walls means suppressing any flux of mass, temperature, salinity and other tracers through the Canadian Arctic Archipelago, through Fram Strait and into Barents Sea. Neglect of these processes may severely influence the North Atlantic circulation, including deep water formation and Meridional Overturning (see e.g. Wekerle et al., 2011; Hu et al., 2010). Regarding volume, this results in an imbalance of several Sverdrups propagating southwards throughout the model domain. The only open lateral boundary is the Southern edge of the domain. Here an integrated flux condition known from a forward model run on a larger domain is applied (Richter, 2010).

4.1.3 Cost function

A cost function penalizes the residuals of the advection-diffusion equations as well as the deviation from data sets and model behaviour that is known to be unrealistic. In IFEOM, this is done in a least-squares sense:

$$J = \frac{1}{2}\sum_i J_i \quad (4.15)$$

The first two terms of J penalize the residuals $\boldsymbol{\epsilon}_T$ and $\boldsymbol{\epsilon}_S$:

$$J_1 = \boldsymbol{\epsilon}_T^T \mathbb{W}_{\epsilon_T} \boldsymbol{\epsilon}_T \quad (4.16)$$

$$J_2 = \boldsymbol{\epsilon}_S^T \mathbb{W}_{\epsilon_S} \boldsymbol{\epsilon}_S \quad (4.17)$$

In this chapter, some scalar values such as the residuals, temperature etc. are bold to stress that they are represented as vectors in the model code when we consider the whole model domain. In this way, it makes sense to introduce error covariance or weighting matrices, respectively.

The following two terms penalize the deviations from a climatology. We use the climatology of Gouretski and Koltermann (2004), as Sidorenko (2004) showed it to be among the most suitable for our application.

$$J_3 = (\boldsymbol{T} - \boldsymbol{T}_{\text{klim}})^T \mathbb{W}_{\text{klim}_T} (\boldsymbol{T} - \boldsymbol{T}_{\text{klim}}) \tag{4.18}$$

$$J_4 = (\boldsymbol{S} - \boldsymbol{S}_{\text{klim}})^T \mathbb{W}_{\text{klim}_S} (\boldsymbol{S} - \boldsymbol{S}_{\text{klim}}) \tag{4.19}$$

The inverse model lacks some skill in reproducing the mean circulation correctly. In order to reduce the individual cost function terms, the models tends to undertake dramatic changes to the deep ocean circulation. This contradicts our general understanding of the ocean circulation and also the first guess solution. Because we believe the deep ocean should not undergo intense changes, another constraint is applied below 2000 m depth:

$$J_5 = (\boldsymbol{u} - \boldsymbol{u}_{\text{prog}})^T \mathbb{W}_{uv} (\boldsymbol{u} - \boldsymbol{u}_{\text{prog}}) + (\boldsymbol{v} - \boldsymbol{v}_{\text{prog}})^T \mathbb{W}_{uv} (\boldsymbol{v} - \boldsymbol{v}_{\text{prog}}) \tag{4.20}$$

A detailed study of this "deep velocity constraint" is given in Sidorenko (2004).

The most relevant term in this study includes $\boldsymbol{\eta}_{\text{data}}$, the new mean dynamic topography and its associated inverse error covariance serving as weighting matrix $\mathbb{W}_\eta$:

$$J_6 = (\boldsymbol{P}_{2\times 2}\boldsymbol{\eta} - \boldsymbol{\eta}_{\text{data}})^T \mathbb{W}_\eta (\boldsymbol{P}_{2x2}\boldsymbol{\eta} - \boldsymbol{\eta}_{\text{data}}). \tag{4.21}$$

Some experiments described in the following sections required the use of an interpolation operator $\boldsymbol{P}_{2\times 2}$. Theoretically, in this approach the MDT is calculated directly on the ocean model grid, however the geodetic calculations are very time and storage consuming. Therefore in some cases it was required to work with MDT data given on a $2^\circ \times 2^\circ$ subgrid of the IFEOM grid only. $\boldsymbol{P}_{2\times 2}$ then does the projection to this subgrid and equals identity otherwise.

Additional smoothing constraints and scaling issues are examined in Richter (2010).

Each cost function term is applied to each node of the three dimensional ocean model grid, except the MDT data deviations which are naturally given only at the ocean surface and the deep velocity constraint which is applied only below 2000 m depth. Thus the cost function J has $N = 838063$ different terms but only $M = 234328$ adjustable control variables (T and S), leaving $N - M = 603735$ degrees of freedom.

The limited-memory-quasi-Newton method BFGS and the routine M1QN3 are applied for approaching the minimum of the cost function J (see Nocedal, 1980; Gilbert and Lemarécha, 1995). The gradient of the cost function is computed via the adjoint model equations, see Sidorenko (2004). In each model run, 5000 iterations were executed to ensure the cost function is not decreasing any more. (Compare e.g. Richter (2010), who carried out similar assimilations using IFEOM with a maximum of 3000 iterations.)

4.1.4 First guess solution

For a meaningful and relatively fast solution, it is most important to provide the inverse model with a reasonable first guess for the control variables (density at each node of the model grid). We use the outcome of a long-term IFEOM model run that was fit to the climatology data only (Gouretski and Koltermann, 2004, and no additional data sets). Therefore at the starting point of the actual minimization and assimilation of additional data, the climatology and the advection-diffusion equations are already in good balance with each other. The first guess solution already served as a reference model run in Richter (2010) and some of its oceanographic features are shown in figure 4.2.

The first guess solution is very smooth and remains close to the climatology of Gouretski and Koltermann (2004). Whereas the first guess MDT looks reasonable, the barotropic stream function reveals too strong a Subpolar Gyre compared to e.g. Dijkstra (2008), Pinet (1998) and many others. The most striking feature is the anticyclonic circulation in the Norwegian Sea. This has not been observed and contradicts the general conception of the circulation in the Nordic Seas (see for example Hopkins, 1991). Apart from that, the most important currents in the North Atlantic area described for example by Tomczak and Godfrey (1994), Pinet (1998) or on `http://oceancurrents.rsmas.miami.edu/atlantic/atlantic.html`(28 Oct 2011) can be found in the model solution and are well represented.

Evaluation of integrated values is not always straightforward. Whereas the MDT (figure 4.2a) represents the surface circulation in a geostrophic system, the barotropic stream function (figure 4.2b) is integrated over depth. Therefore the "true" shape of the Subtropical Gyre is partly hidden by deep inflow from the south. The MOC (figure 4.2c) is integrated over circles of latitude. These include two different ocean basins north of 60°N and the American Mediterranean Sea between 10°N and 30°N.

A reasonable Meridional Overturning Circulation (MOC) is computed with a maximum of 18 Sv as in Cunningham et al. (2007) and Rayner et al. (2011) who give 18.7 ± 5.6 Sv and 18.7 ± 4.8 Sv, respectively. However, this maximum is expected to occur 10 to 15 degrees further north (Richter, 2010). Meridional heat transports calculated from the first guess estimate are very small compared to those of other authors (see figure 4.14 and references therein). Particularly the low latitudes are considerably underestimated, whereas at about 36°N, we find good agreement (see figure 4.14d). At higher latitudes, the first guess estimate exceeds others (see figures 4.14e and 4.14f). Overall, despite some deficiencies, the first guess seems to be a suitable starting point for the assimilation of data that will improve the model.

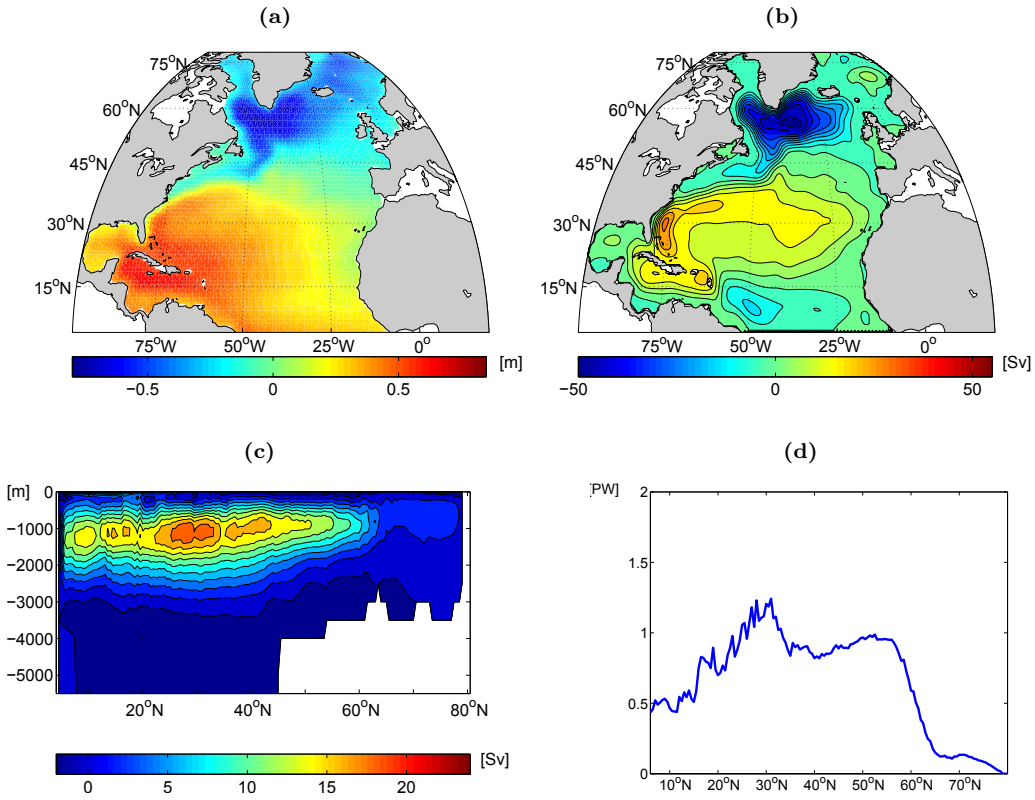

Fig. 4.2: Oceanographic features of the First Guess: (a) Mean dynamic topography, (b) Barotropic stream function, contour interval 5 Sv, (c) Meridional Overturning Circulation, contour interval 2 Sv, (d) Meridional heat transports in Petawatt.

4.2 Results with IFEOM

This section provides a series of different IFEOM model solutions all of which include the new MDT estimate. This MDT estimate was developed and computed at the Institute of Geodesy and Geoinformation (IGG) at the University of Bonn and was made available to the AWI within the framework of the project Rifugio. On the basis of this project, the solutions are named "RifXY", where the number XY stands for the modelling progress. A higher number means improvement compared to a model run with a lower number. An overview is given in table 4.1. The items in the left column will be explained in detail in the following sections.

	Rif01	Rif02	Rif03	Rif04	Rif05
weighting factor $\alpha = 7$	✓	✓	✓	✓	✓
refined omission error model	✘	✓	✓	✓	✓
resolution $1° \times 1°$	✘	✘	✓	✓	✓
2 months of GOCE data	✘	✘	✘	✓	✓
7 months of GOCE data	✘	✘	✘	✘	✓

Table 4.1: Overview of the preconditions for IFEOM model solutions Rif01, Rif02, Rif03, Rif04 and Rif05.

A key aspect is the determination of the weights in the optimization which the following sections are dedicated to. After the improving steps from table 4.1, the structure of the final Rif05 solution is investigated in detail in section 4.2.6.

4.2.1 Determination of weights

In the weighted least-squares method, the quadratic deviations of measured data from the forward model output are weighted by the inverse of their respective error covariances. In this way, data with large errors are considered less important in the fitting procedure, while accurate data with small errors are emphasized (Thacker and Long, 1988). This approach is straightforward as long as an appropriate error description is available. The squared model residuals represent another part of the cost function for which some weighting terms are necessary. Specifying the error resulting from discretization, incorrect bathymetry description etc. is not straightforward and requires special care. However, because the solution is strongly determined by the weights, choosing them is a crucial part of inverse modelling (Egbert and Erofeeva, 2002).

4.2.1.1 The First Guess solution

As described before in section 4.1.4, the first guess used in this study is the output of the inverse ocean model IFEOM that was fit to climatology data. Data and model terms are well balanced due to an elaborate choice of weights. Richter (2010) used as a priori estimation for the temperature and salinity climatology data 2.48 K and 0.35 PSU, respectively. These values decrease down to 0.26 K and 0.037 PSU in the deep ocean where changes are small. The coastlines and the open boundary are also considered separately.

In the regularization term of the cost function, the residuals of temperature and salinity in the advection-diffusion equations are weighted by the inverse of a squared model drift of $10.7\,\mathrm{K\,y^{-1}}$ and $1.5\,\mathrm{PSU\,y^{-1}}$.

Weighting factors for smoothness of temperature and salinity and for the DVC (deep velocity constraint) were adjusted manually by Richter (2010) and Sidorenko (2004). Below 2000 m, the velocities are allowed to vary by $1.4\,\mathrm{cm\,s^{-1}}$ from the forward model run. Leading to a model solution with all penalty terms at approximately the same scale, this facilitates the search for a global minimum and avoids that the solution is completely dominated by one feature or data set.

Introducing the new highly accurate MDT data set implies using its inverse error description as cost function weights. In our situation, we are even provided with a complete MDT error *co*variance for the first time ever. Unfortunately, assimilating the new data in this way leads to a highly overweighted MDT, resulting in an unrealistic ocean circulation. The reason for this behaviour will be investigated in the following sections.

4.2.1.2 Statistical methods for weight definition

In many cases defining appropriate weights to individual cost function terms is a challenge. In many cases, errors are not known or even error sources are unclear. Regularization terms are often used whose influence has to be balanced with the main part of the system (Hansen, 2005). In this situation without sufficient deterministic information, one can gain knowledge from statistical approaches.

The most commonly used statistical concept is that of maximum entropy. This computationally expensive task can be bypassed by using an approximation, namely the maximum data cost (Kivman et al., 2001).

Another very elegant way of parameter estimation is to construct a plot of the cost function term of the regularized solution versus the corresponding residual on a log-log scale. Under certain assumptions, this leads to a very characteristic shape, the so-called "L-curve". The sought-after parameter is situated in the corner, at the point with the largest curvature. If the L-curve is defined by a computable and twice continuously differentiable formula, this can even be determined analytically (Hansen and O'Leary, 1993).

However, application of these methods fails for the IFEOM model as they rely on

the existence of a maximum or a L-shaped curve, respectively. This might be connected to a phenomenon that is investigated by Hanke (1996) using the example of the sideways heat equation[1]. He uses the L-curve method to determine the parameter α in the minimization problem $\|y^\delta - Kx\|^2 + \alpha\|x\|^2 \longrightarrow \min$ where y^δ is the given data, contaminated by noise δ. The penalty term $\alpha\|x\|^2$ stabilizes the solution. This method is also known as Tikhonov regularization.

This problem is equivalent to ours seen as $\frac{1}{\alpha}\|y^\delta - Kx\|^2 + \|\hat{K}x\|^2 \longrightarrow \min$ with some regularization (model) operator $\hat{K}$ and data y^δ with weight $\frac{1}{\alpha}$. This way of writing is more favourable in our case as the "regularization" consists of several already scaled terms and the data term $\|y^\delta - Kx\|^2$ is the new input whose weighting shall be investigated here.

Hanke now proves that in the general case, the α resulting from the L-curve method grows quadratically with error δ decreasing. This is exactly what one would expect from the deterministic least-squares point of view. The numerical example however demonstrates that this quadratic increase of parameter α is too large and therefore the results become biased and erroneous when the error estimate δ approaches zero.

One assumption in using the simple weighted least-squares method is that there are no or only negligibly small errors in variables other than the measured data y^δ. Violation of this precondition is widespread in practice and therefore its implications are analysed in the literature for several applications, see e.g. de Brauwere et al. (2005), Bruzzone and Moreno (1998). In our case, considering the penalty term $\|y^\delta - Kx\|^2$ with Kx representing the model MDT, investigation of the accuracy of the model MDT in comparison to the data MDT is necessary. Bruzzone and Moreno (1998) give a condition stating that $\frac{\text{error(model MDT)}}{\text{error(data MDT)}} \ll 1$ is required for neglecting the model MDT error. If this cannot be satisfied, the effective variance method of Barker and Diana (1974) has to be applied. De Brauwere et al. (2005) provide detailed instructions in how the refined covariance matrix can be constructed.

Assuming the IFEOM model error cannot be neglected compared to the highly accurate MDT data set, there is still no appropriate description of the model error part that is necessary for the refinement of the covariance matrix. Therefore other methods are needed for the determination of some reasonable weighting factor α in the cost function $J = \frac{1}{\alpha}J_{\text{MDT}} + J_{\text{IFEOM}}$. In the following, three different attempts are tested and compared to each other.

[1]The sideways heat equation is a model of a problem where one wants to determine the temperature on both sides of a thick wall, but where one side is inaccessible to measurements:

$$\begin{aligned} u_t &= u_{xx}, \qquad 0 < x < \infty,\ 0 < t < \infty \\ u(x,0) &= 0, \qquad 0 \le x \le \infty, \end{aligned}$$

where the temperature profile is measured at $y = u(1, \cdot)$ and the boundary values $u(0,t)$, $t > 0$, are sought. This kind of problem is a frequently occurring situation in many remote sensing applications.

4.2.1.3 Approach 1: Minimum model MDT error (MMME)

At the current state of research, we are not able to calculate an accurate error estimate for the IFEOM MDT that is compared to the measured MDT data in the least-squares fit. However, we can think of a lower bound for this error, precisely the lowest model MDT error that still allows a sensible least squares optimization. To make the LSF solution lie within the standard deviation of the data as well as the standard deviation of the model, we need to satisfy

$$|\mathrm{MDT}_{\mathrm{data}} - \mathrm{MDT}_{\mathrm{model}}| \leq \sigma_{\mathrm{data}} + \sigma_{\mathrm{model}}$$

at each grid point, see sketch in figure 4.3. Thus

$$(|\mathrm{MDT}_{\mathrm{data}} - \mathrm{MDT}_{\mathrm{model}}| - \sigma_{\mathrm{data}})^2 = \min\{\sigma^2_{\mathrm{model}}\}$$

is defined as a minimal model MDT error and added on the diagonal of the MDT data covariance.

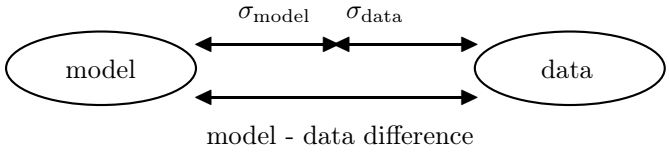

Fig. 4.3: Reasonable model-data differences should be smaller than the sum of model standard deviation and data standard deviation.

The diagonal of the data covariance σ^2_{data} is used in this calculation which largely overestimates the data variance due to the neglection of the error correlation. So the resulting $\min\{\sigma^2_{\mathrm{model}}\}$ is still too small compared to the true value, but gives a lower bound.

The maximum eigenvalue of the inverse MDT error covariance is $9026.6\,\mathrm{m}^{-2}$ in the model run Rif05 (see section 4.2.5). The maximum eigenvalue of the combined effective inverse covariance matrix calculated above is $2731.4\,\mathrm{m}^{-2}$. As we want to keep the structure of the actual inverse data covariance instead of using the combined effective inverse covariance based on model-data discrepancies, we compute the factor α as the fraction of the maximum eigenvalues of the respective inverse covariance matrices

$$\frac{9026.6\,\mathrm{m}^{-2}}{2731.4\,\mathrm{m}^{-2}} = 3.3048 \approx 3.3 = \alpha_{\mathrm{MMME}}$$

and use $\frac{1}{\alpha}\mathbb{W}_\eta$ in equation (4.21). In this way, this approach provides us with a lower boundary for the factor α.

4.2.1.4 Approach 2: Minimum penalty variance (MPV)

In a well balanced model-data system, none of the different penalty terms in the cost function should dominate the others to a large extent after optimization (Loza, S. and Sidorenko, D., pers. comm.). This is due to the weighting by the inverse error covariances - if some terms of the cost function differ in scale from others, it means that weights were not chosen appropriately for the data-model comparison. It is not necessary that the penalty terms are equal, but it is very unlikely that they are of different scale.

If the weighting factor α is very small, the penalty term for the MDT becomes much larger then the other ones, leading to a solution completely determined by the MDT data. The penalty terms are of different scale, thus their variance is high as shown in figure 4.4. Similarly, a very large α causes underweighting of the MDT data und a high penalty term variance. In between, we find the optimum for the IFEOM model system at the minimum penalty variance parameter $\alpha_{\mathrm{MPV}} = 7$.

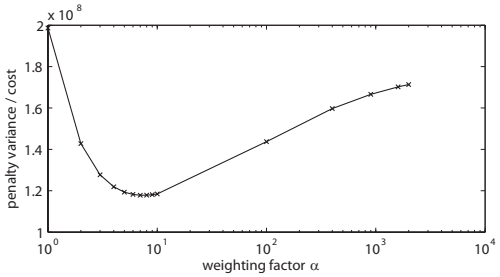

Fig. 4.4: Penalty variance normalized by overall cost in dependence of weighting factor α. A minimum is found at $\alpha = 7$.

4.2.1.5 Approach 3: Maximum model entropy (MME)

To analyse the behaviour of IFEOM subject to MDT datasets with errors of different magnitude, the following experiment was designed. The first guess MDT is taken as reality and disturbed by random Gaussian errors with zero mean and different constant standard deviations. In a series of simulations, the resulting datasets are assimilated back into the IFEOM model, using the inverses of the squared standard deviations as weights in the cost function.

In this way, the weighting is consistent with the actual deviation of the synthetic data from the first guess and with the way we define the respective covariance matrices using the "real" data with "real" error estimates.

The fit to the data becomes monotonically better with decreasing error, also in the relative sense ($\frac{\text{posterior deviation}}{\text{prior error}}$). In contrast, the fit to the model behaves non-monotonically as shown in figure 4.5. The mean squared posterior deviations from the first guess solution show a strong peak while the prior model errors are kept constant.

We interpret this peak as a region in the model space that advances maximum model entropy in the sense of Kivman et al. (2001). The location of the maximum is found by fitting a parabola to the model fit plot on a log-log scale. That means we fit a function of the type $f(x) = 10^c \cdot x^{a \ln x + b}$ and calculate its maximum location analytically. We get $x_{\max} = \exp\left(\frac{-b}{a}\right) = 0.0577\,\mathrm{m}$ as the disturbing error that maximizes the model entropy in the optimization. Thus the eigenvalues of the respective weighting matrix equal $0.0577^{-2}\,\mathrm{m}^{-2}$ and the weighting factor α becomes

$$\frac{9026.6\,\mathrm{m}^{-2}}{0.0577^{-2}\,\mathrm{m}^{-2}} = 30.0522 \approx 30 = \alpha_{\mathrm{MME}}.$$

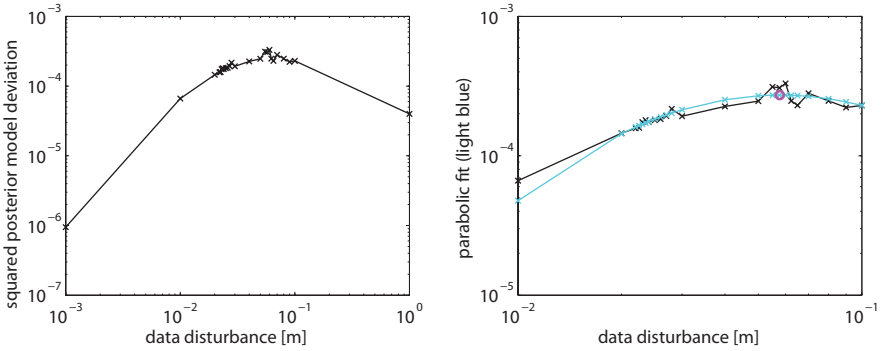

Fig. 4.5: MME approach: Model cost in dependence of prior data error, parabolic fit (cyan) and maximum point of fit (magenta)

4.2.1.6 Conclusion

Approach 1 provides only a lower bound for the weighting factor $\alpha_{\mathrm{MMME}} = 3.3$. This boundary is consistent with the results of approach 2 and 3 that return $\alpha_{\mathrm{MPV}} = 7$ and $\alpha_{\mathrm{MME}} = 30$. We will investigate the effect of the two different factors α_{MPV} and α_{MME} for tuning the cost function of IFEOM in the next step.

4.2.2 Impact of weighting factors

For demonstrating the impact of the weighting factors, the example of the Rif05 solution (see section 4.2.5 or, for a quick check, table 4.1) is used. However, the same effects can also be seen in all other solutions. The findings detailed in this section are illustrated in table 4.2 and figure 4.6.

In the least-squares fit optimization procedure, the model is searching for the best compromise between the first guess and the new data (MDT). Downweighting the data by a factor $\alpha = 30$ leads to a solution "resembling" the first guess, while a weighting factor of $\alpha = 7$ produces a slightly better fit to the MDT data.

Therefore, with $\alpha = 7$ we observe higher maxima of the stream function, of the Meridional Overturning Circulation and also of the meridional heat transports. The Gulf Stream and the Mann Eddy at approximately 42°N, 43°W are more pronounced, the MDT gradient across the Gulf Stream is steeper. For $\alpha = 7$, the MOC is considerably stronger between 0°N and 20°N.

As already stated by Richter (2010), this indicates inconsistency of the MDT data with the boundary condition on the Southern boundary of the model domain. The barotropic transports computed by a prognostic ocean model also described by Richter (2010) are prescribed on the Southern boundary. This prognostic model does not incorporate any measurements of MDT or velocity and differs substantially from the MDT data information. As no error estimate is provided together with the prognostic model run, we appreciate the changes to the MOC by the MDT data, so that the weighting factor $\alpha = 7$ seems more appropriate than $\alpha = 30$.

This is also supported by a recent study of Knudsen et al. (2011) who evaluate the geodetic satellite-only MDTs against the Maximenko MDT (Maximenko et al., 2009) which incorporates in-situ drifter data. The authors observe similar features as the above mentioned (sharpening of currents and increased velocities) and substantiate their likeliness via comparison to the combined Maximenko MDT.

	$\alpha = 7$	$\alpha = 30$
stream function maximum	55.6 Sv	53.8 Sv
overturning maximum	23.7 Sv	22.9 Sv
heat transports maximum	1.76 PW	1.66 PW

Table 4.2: Comparison of selected oceanographic diagnostics for weighting factors $\alpha = 7$ and $\alpha = 30$.

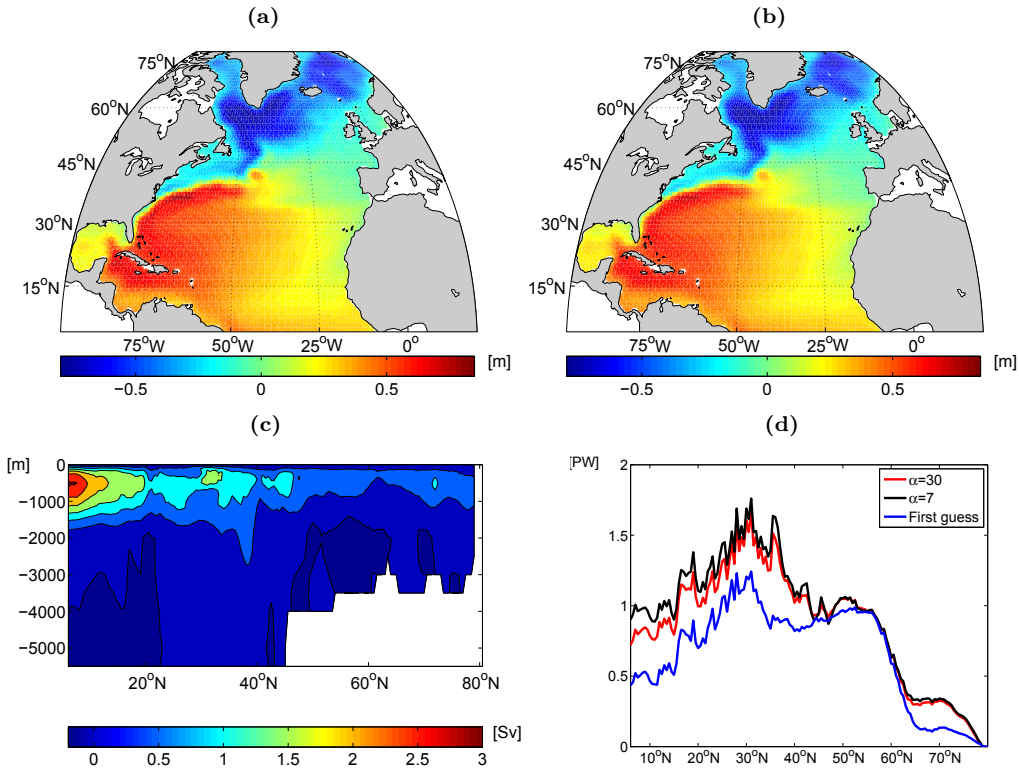

Fig. 4.6: Comparison of oceanographic features of the solution Rif05 from section 4.2.5, for $\alpha = 7$ and $\alpha = 30$: (a) Mean dynamic topography, $\alpha = 7$, (b) Mean dynamic topography, $\alpha = 30$, (c) Meridional Overturning Circulation difference, "MOC($\alpha = 7$) − MOC($\alpha = 30$)", contour interval 0.5 Sv, (d) Meridional heat transports in Petawatt

4.2.3 Impact of omission error model

To investigate the influence of the omission error (see section 2.1.3) models on the solution, the stochastic model introduced in section 2.4.3 is specified further. Two extreme cases have been analysed on a two degree grid. These and also another case in between the two extremes are presented in Becker et al. (2012).

In the first case, we make the assumption that no further a priori information about the signal content of the gravity field is known beyond degree and order 240. A reduction of the signal $\boldsymbol{\mathcal{S}}$ by a deterministic approximation of the mean sea surface enables us to compute an empirical auto-covariance function and thus to assemble the covariance matrix $\boldsymbol{\Sigma}_S^{\text{emp}}$. The expectation value is assumed to be zero due to the reduction by the deterministic model, resulting in the stochastic characteristics of $\mathcal{S}$:

$$\boldsymbol{E}\{\boldsymbol{\mathcal{S}}\} = \mathbf{0} := \Delta\boldsymbol{l}_{\text{MSS}}, \quad \boldsymbol{\Sigma}\{\boldsymbol{\mathcal{S}}\} = \boldsymbol{\Sigma}_S^{\text{emp}} := \boldsymbol{\Sigma}_{\Delta\text{MSS}} \tag{4.22}$$

The IFEOM solution using this omission error model is called Rif01, see also Becker et al. (2012).

In the second - contradicting - case, we assume extensive knowledge about the omission domain. The information of the gravity field model EGM08 (Pavlis et al., 2008) is used to reduce the mean sea surface by the geoid signal in the range between degree and order 241 and 2160. The EGM08 provides estimates of error degree variances $\sigma^2_{n,\text{EGM08}}$ which are used to estimate the accuracy of the geoid height information. Beyond degree and order 2160, Kaula's rule of thumb is introduced as prior information: $\boldsymbol{\mathcal{X}}_{\text{cs4}} \sim \mathcal{N}(\mathbf{0}, \boldsymbol{\Sigma}_{\text{cs4}}^{\text{smooth}})$. The omission part of the covariance function thus reads

$$\begin{aligned}\text{Cov}(N(r,\phi,\lambda), N(r',\phi',\lambda')) &= \frac{G^2M^2}{R^2\gamma(B)\gamma(B')} \sum_{n=241}^{2160} \frac{R^{2(n+1)}}{(rr')^{n+1}} \sigma^2_{n,\text{EGM08}} P_n(\cos\psi) \\ &+ \frac{G^2M^2}{R^2\gamma(B)\gamma(B')} \sum_{n=2160}^{\infty} \frac{R^{2(n+1)}}{(rr')^{n+1}} \sigma^2_{n} P_n(\cos\psi) \end{aligned} \tag{4.23}$$

with Legendre polynomials $P_n(\cos\psi)$ and spherical distance ψ. Combining the different frequency domains results in

$$\boldsymbol{E}\boldsymbol{\mathcal{S}} = \Delta\boldsymbol{l}_{\text{EGM08}} := \Delta\boldsymbol{l}_{\text{MSS}} \tag{4.24}$$

$$\boldsymbol{\Sigma}\boldsymbol{\mathcal{S}} = \boldsymbol{\Sigma}_{S1}^{\text{EGM08}} + \boldsymbol{\Sigma}_{S2}^{\text{Kaula}} = \boldsymbol{\Sigma}_{\Delta\text{MSS}} \tag{4.25}$$

The IFEOM solution using this omission error model is called Rif02.

Leaving the omission error model undetermined up to the statistics as in the Rif01 model gives little improvement over the first guess. Even with weighting factor $\alpha = 7$, the solution is still determined by the prior guess, compare figure 4.7 and figure 4.2. Features like the weak Gulf Stream, low heat transports and the anticyclonic circulation in the Nordic Seas are still present. The error description and thus the weighting of the data cost term is not sufficient to improve the solution. In contrast, using the second omission error model leads to increased weights and thus to changes like the ones described in the previous section, see figures 4.9a and 4.9d. Therefore, from now on, we always use the second modelling approach assuming considerable knowledge about the omission error.

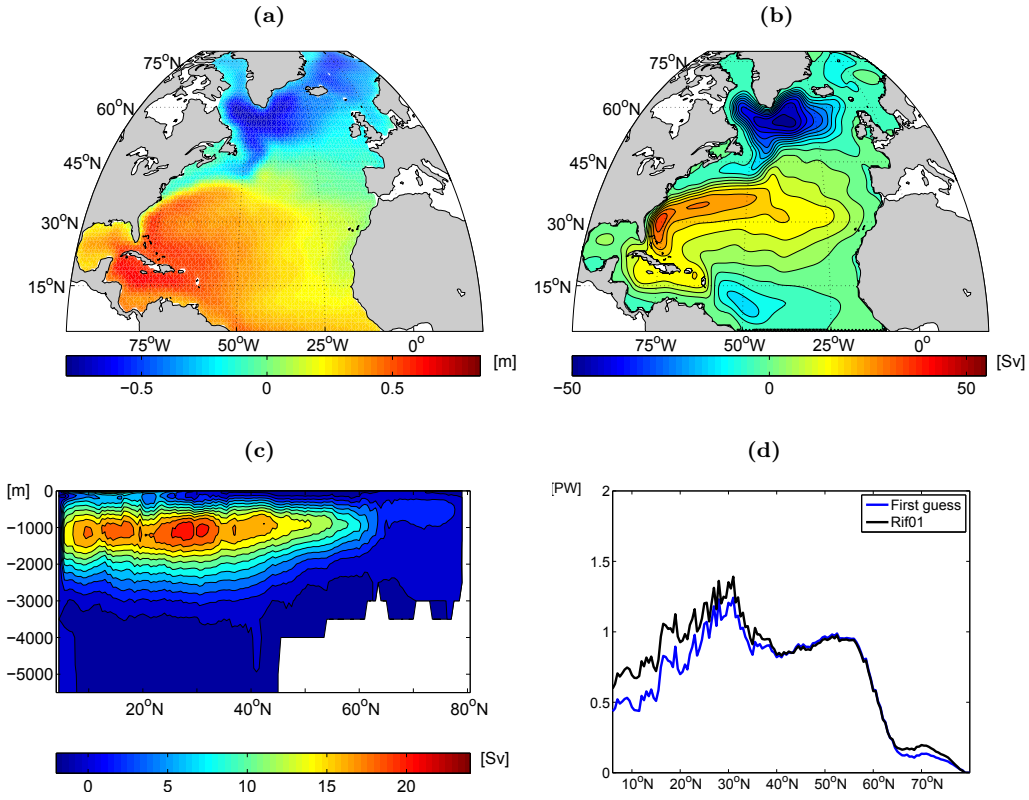

Fig. 4.7: Oceanographic features of the solution Rif01 with $\alpha = 7$: (a) Mean dynamic topography, (b) Barotropic stream function, contour interval 5 Sv, (c) Meridional Overturning Circulation, contour interval 2 Sv, (d) Meridional heat transports in Petawatt.

4.2.4 Impact of resolution

In the previous section, the combined MDT was only calculated on a 2° subgrid of the North Atlantic IFEOM mesh and the modelled MDT was interpolated to the ocean's coarse grid. Now, the computation is extended to the actual 1° grid of the ocean model IFEOM and the resulting model solution is named Rif03.

Applying the MDT on a 1° grid leads to a less smooth solution revealing more details of the circulation. The Meridional Overturning is enforced in the region near the Southern boundary as well as between 30 and 45°N. Obviously this is related with the intensified Gulf Stream and Mann Eddy in these latitudes. Meridional heat transports are amplified as well south of 45°N, most noticable the strong peak between 35°N and 40°N. North of approximately 45°N, the changed MDT grid does not modify the heat transports considerably.

Flow from the North Atlantic into the Nordic Seas is better reproduced in the model solution Rif03. In figure 4.8, it can be seen that there is only little mean flow across the Iceland-Faroe Ridge, but flow through the channels has increased and transports several Sverdrups more across the topographic features. For more details concerning topography in this area, consider e.g. Hansen and Østerhus (2000). The resolution of the ocean grid itself did not change proceeding from Rif02 to Rif03, thus the effect observed is not the same as found by Oka and Hasumi (2006). They show by modelling experiments that the representation of the overturning circulation is dependent on model resolution, mostly due to the delicate topography in the northern North Atlantic. A traditional way to overcome the topographic blocking due to coarse resolution is prescribing known surface fluxes as boundary conditions. Assimilating MDT data is comparable via inducing surface currents as long as resolution is not coarser than the ocean model grid.

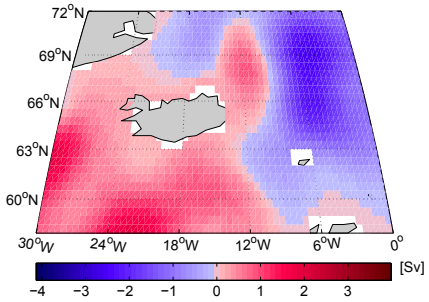

Fig. 4.8: Stream function differences between solutions Rif03 and Rif02 in the North East North Atlantic.

It can also be seen from figure 4.9 that the resolution of the MDT plays an important role for the modelling output. All the following results therefore used a MDT that was computed on the 1° grid.

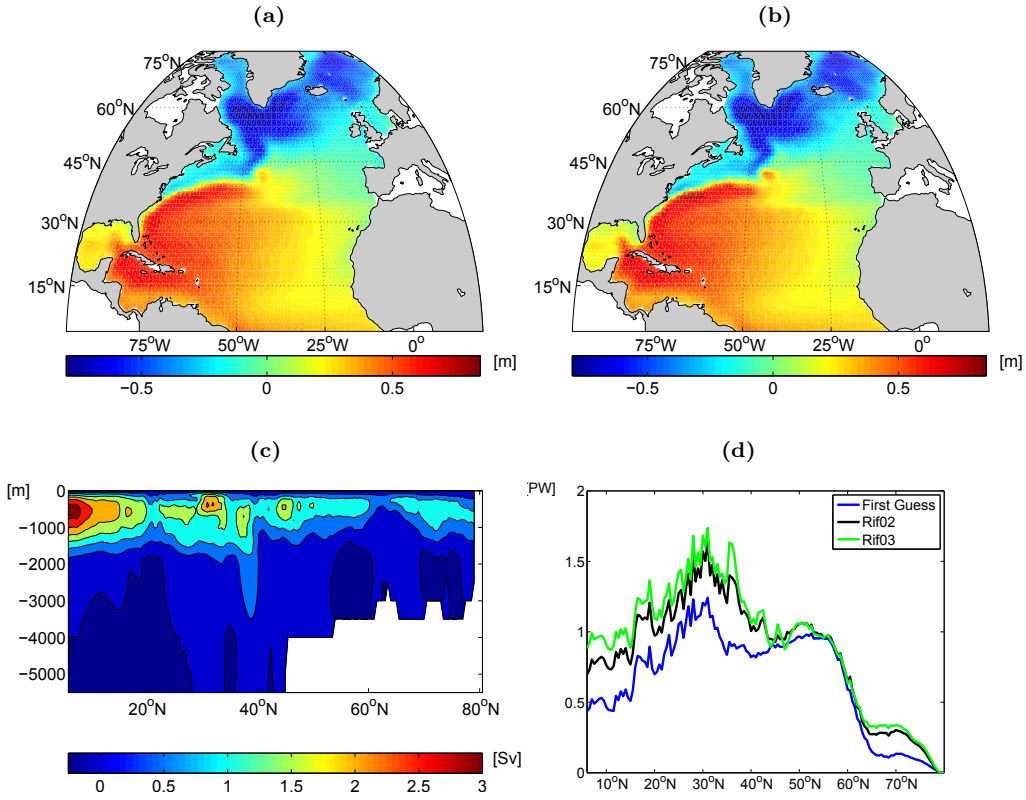

Fig. 4.9: Oceanographic features of the solutions with different MDT data resolution: (a) Mean dynamic topography: Rif02, (b) Mean dynamic topography: Rif03, (c) Meridional Overturning difference, contour interval 0.5 Sv, (d) Meridional heat transports in Petawatt.

4.2.5 Impact of 2 months and 7 months of GOCE data

Launched in March 2009, the satellite mission GOCE (see section 2.1.1) became operational in October 2009 (Steiger et al., 2010). The first level-2 gravity products are available since 2010 (Pail et al., 2010). In this study, we first incorporated 2 months of GOCE data in the MDT computation and named the corresponding IFEOM solution Rif04. Later on, 7 months of GOCE data were used when they were available, leading to the solution named Rif05.

Modifications achieved by the new data set are slight but noteworthy. The difference plots of the MDT to the GRACE only solution (4.10a and 4.10b) reveal that striping effects are present in the solutions, although they are too small to be visible in the solutions themselves. Already 2 months of the new GOCE data suffice to uncover the striping effect north of 60°N where the oscillations and therefore the deviations from the first guess are highest. Using the full 7 months of available GOCE data does not perform any more modifications to the high latitudes but results in small stripy changes almost all over the model domain down to 20°N.

We have a closer look at one of the areas of the largest changes, that is the Greenland Sea along latitude 73.5°N. Figure 4.11a presents the MDTs of the solutions Rif03, Rif04 and Rif05 along this section. Small oscillations on the grid scale are visible, however of an amplitude far below 1 cm which is below the accuracy of the GOCE data. Comparison of the MDT results with the actual data input (figure 4.11b, 4.11c and 4.11d) shows that the oscillations observed in the results are obviously the remainders of much larger oscillations in the MDT data. As already mentioned in section 2.4.4, the MDT data itself without its covariance information is not smooth. Only using its error covariance information content via an assimilation procedure reveals the benefit of the approach. The grid scale oscillations are almost completely removed from the MDT in the solutions. This result cannot be attributed to the smoothness conditions implemented in the ocean model! The MDT is heavily weighted in the least-squares optimization due to the Rifugio error estimates. Therefore a good data fit in terms of its covariance structure is favoured by the model over sticking to the smooth first guess estimate. Hence, Reduction of amplitudes during the optimization procedure is not due to model smoothing but a result of the MDT error covariance. Thus we directly observe the benefit of the Rifugio approach.

The oscillations of the MDT data decrease from approach Rif03 to Rif05, with an amplitude range of 90 cm for Rif03, 54 cm for Rif04 and 44 cm for Rif05 (considering only the section along 73.5°N in the Greenland Sea). This decrease in oscillations is probably due to the more accurate GOCE data used in the models Rif04 and Rif05.

The circulation itself is modified only to a minimal extent which can be seen in the virtually identical meridional heat transports (figure 4.10e) and the small stream function changes of less than a Sverdrup (figure 4.10c). This reflects consistency of the new GOCE data with the combined GRACE-IFEOM-MDT Rif03.

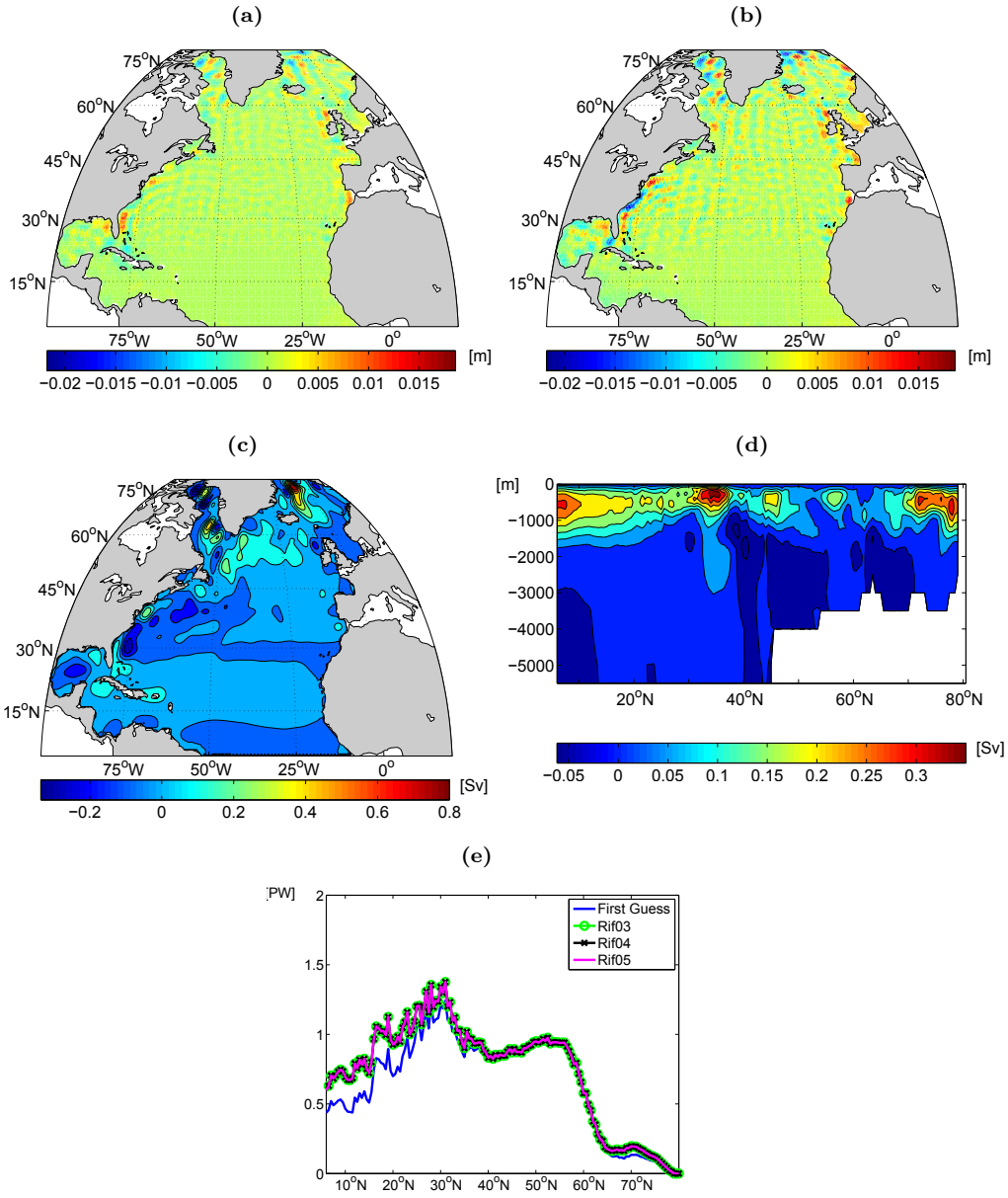

Fig. 4.10: Oceanographic features of the solution with GOCE data, Rif04 and Rif05: (a) Mean dynamic topography difference Rif04-Rif03, (b) Mean dynamic topography difference Rif05-Rif03, (c) Barotropic stream function difference Rif05-Rif03, contour interval 0.1 Sv, (d) Meridional Overturning difference Rif05-Rif03, contour interval 0.05 Sv, (d) Meridional heat transports in Petawatt.

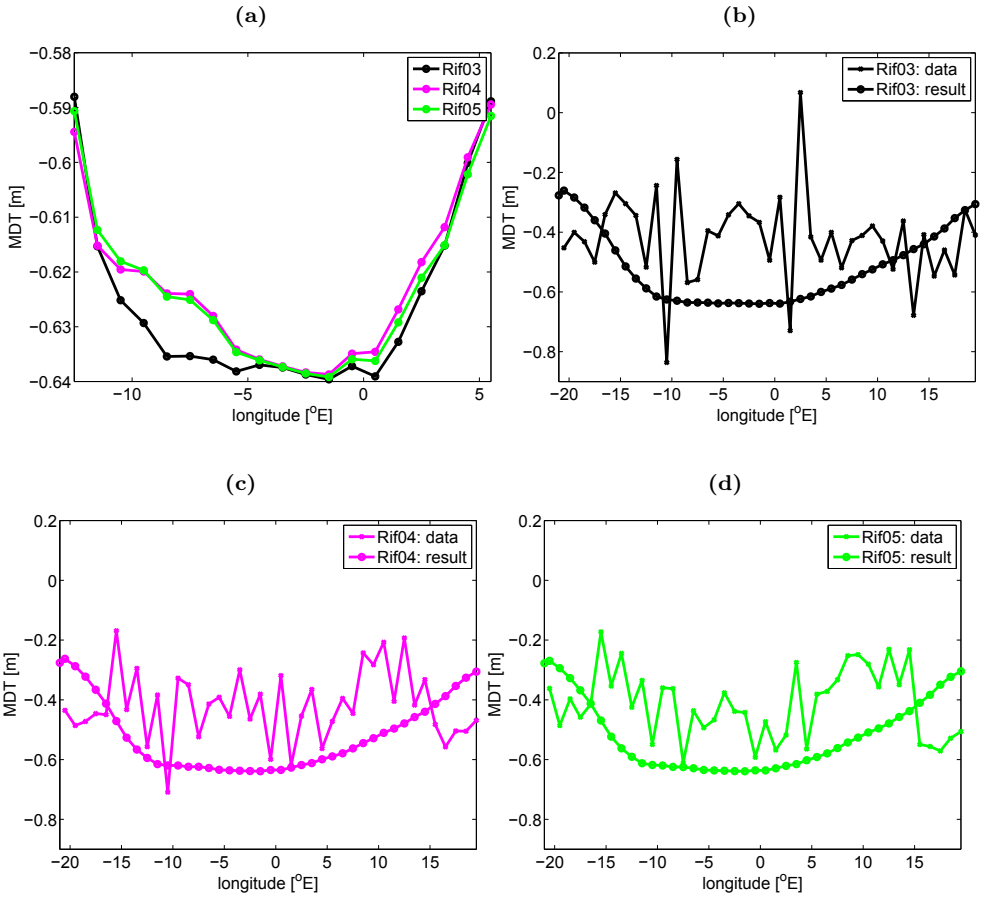

Fig. 4.11: "Striping effects" on a latitudinal section across the Greenland Sea at 73.5°N: (a) IFEOM MDT: model solutions Rif03, Rif04, Rif05, (b) Rif03: MDT data and model result, (c) Rif04: MDT data and model result, (d) Rif05: MDT data and model result.

4.2.6 Final IFEOM solution

An overview of the IFEOM solutions Rif01 to Rif05 is given in table 4.1. Selected oceanographic features of our best IFEOM solution, Rif05, are presented in figure 4.12. The weighting factor $\alpha = 7$ was used in the computation. The MDT was given on a 1° grid with omission error model as in Rif02 and utilizing the full 7 months of available GOCE data.

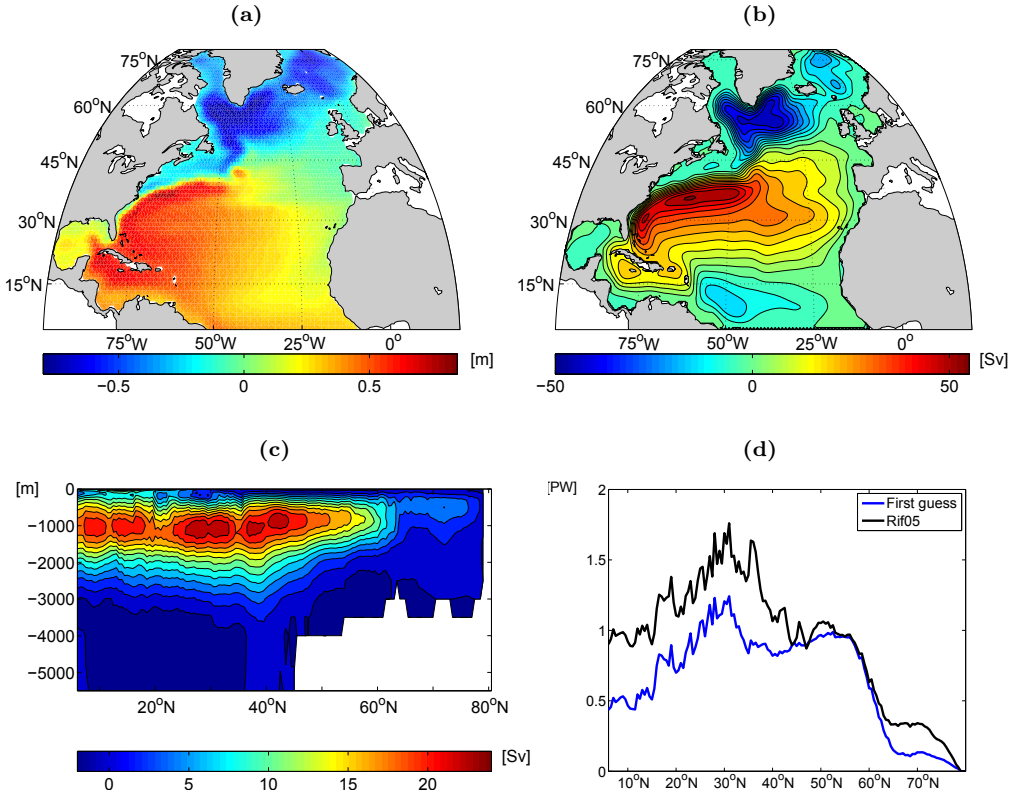

Fig. 4.12: Oceanographic features of the final IFEOM solution Rif05: (a) Mean dynamic topography, (b) Barotropic stream function, contour interval 5 Sv, (c) Meridional Overturning Circulation, contour interval 2 Sv, (d) Meridional heat transports in Petawatt.

Improvements over the first guess solution (figure 4.2) are numerous. The Gulf Stream is stronger and more of its small scale structure becomes visible. The Subtropical Gyre is better represented in the Rif05 solution as well as the Mann Eddy. The latter could not be detected in the first guess. The circulation in the Norwegian Sea is corrected by the data assimilation towards an anticyclonic flow and the circulation between the Nordic Seas and the Atlantic Ocean is improved. The Meridional Overturning Circulation is strengthened, particularly the cell between 7°N and 20°N which was too weak in the first guess estimate compared to the "AltArgo" model runs by Richter (2010). Meridional heat transports are increased considerably 7°N and 55°N and to a smaller extent between 65°N and 75°N. The structure of the heat transports is similar, apart from a strong peak between roughly 35°N and 40°N. This peak can

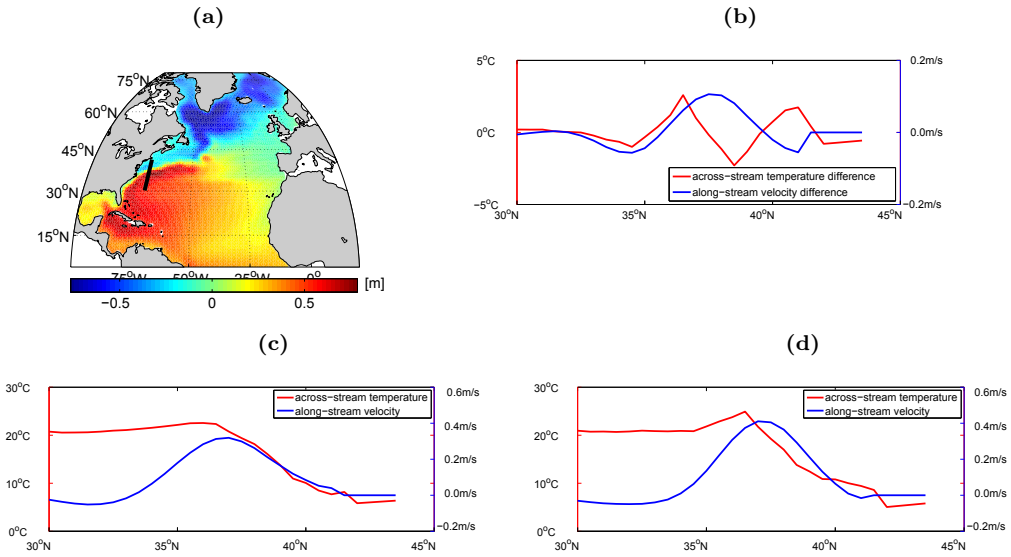

Fig. 4.13: Velocities and temperature at a longitudinal section across the Gulf Stream: (a) Area of particular interest: 70°W, 30°N to 45°N, (b) Differences of IFEOM solution Rif05 to Richter's solution, at 70°W, between 30°N and 45°N, (c) Richter's solution at 70°W, (d) IFEOM Rif05 solution at 70°W.

clearly be attributed to the intensification of the Gulf Stream in the new model.

Differences in Gulf Stream and North Atlantic Current velocities and across-stream temperatures as presented in figure 4.13b may possibly be attributed to a southward shift of the current system. It becomes obvious in figures 4.13c and 4.13d that this is not true. The model reacts to the steeper MDT data input in two distinct ways: The geostrophic velocity is adjusted by about $10\,\mathrm{cm\,s^{-1}}$ to match the increased across-stream density gradient. At the same time the density gradient is increased by a modification in temperature which was increased from 23 °C to 25 °C at the southern boundary of the current and decreased from 6 °C to 5 °C at the northern boundary. These changes are well within the a priori assumed errors. Hence, both across-stream temperature difference and along-stream velocity are higher in the Rif05 solution than in Richter's work.

IFEOM is a stationary model, i.e. time variability is not included. Thus we describe a steady state such as a monthly average which does not exist in reality. Not only the time-dependent data is conflicting with this approach, but also physical processes cannot be represented properly in this type of model. The high variability of the oceanic system is well known and an example for the heat transport varying between different time spans can be found in Koltermann et al. (1999). Lorbacher and Koltermann (2000) quantify the annual variability to 30% in the heat transports and to 20% in the Meridional Overturning rate. However, the assumption that large-scale baroclinic interior flow does not vary on seasonal or shorter time scales can be justi-

fied (Bryden et al., 2005) and constitutes the background for our modelling approach. Comparison to other authors' findings is difficult though, because different data sets from different decades are used and evaluated. Figure 4.14 can therefore only give an impression of whether orders of magnitude coincide with common belief.

For the low latitudes (figures 4.14a and 4.14b), a very high variability due to the strong wind dependence of the heat transports is expected (Klein et al., 1995). The stationary IFEOM used for this study does not incorporate external wind data, and given the strong dependence on the boundary condition along 4°N, this model is not applicable for the tropics. IFEOM heat transport estimates are relatively small at these latitudes however mainly influenced by the boundary condition at the Southern boundary of the model domain. At latitudes around 24°N, there are numerous estimates of heat transport available of which most agree with ours within errorbars (figure 4.14c). The increase of the North Atlantic Current in the IFEOM solutions is reflected in a sharp peak in the meridional heat transports at 36°N which is not consistent with estimates of other authors given in figure 4.14d. In our step-by-step-procedure of improving the model as described in the previous sections, this sharp peak occurs first when the MDT data is given on a 1° grid. In contrast to all other MDT estimates known to the author, the Rifugio MDT is the only one which has not been treated by explicit additional smoothing. Thus it is able to accurately represent this feature of ocean circulation. However, given the variablity of the flow field, this is not to be overinterpreted. At higher latitudes (figures 4.14e and 4.14f), the IFEOM model results in higher heat transports than are usually estimated, independent of whether Richter's data and method or the Rifugio approach is applied. There are two possible reasons for this. First, the IFEOM model circulation is subject to the closed boundaries applied in the polar areas, and the rather shallow and finely structured bathymetry in the Nordic Seas. Second, the satellite data quality deteriorates at higher latitudes which leads to less adjustment of the model to the data.

The overall maximum of the Meridional Overturning stream function (MOC) and its maximum values at specific latitudinal sections are given in table 4.3. The estimates of Rif05 are a bit higher than those of Richter (2010) throughout. However, they agree with most other estimates presented in the table. The large range of the values and the few error estimates demonstrate again the high uncertainty of the results. Consider for example Cunningham et al. (2007) for the interannual variability of the MOC (5.6-34.9 Sv) or Köhl and Stammer (2008) for a 50-year time series estimate of the North Atlantic MOC.

As already stated in section 4.2.2, the improvement of the ocean current structure due to the new model resemble those found by Knudsen et al. (2011) when they analysed the new GOCE data. Surprisingly, using the Rifugio approach, these improvements occur already by improved modelling (solutions Rif02 and Rif03), without using the GOCE data. Incorporating the GOCE data does not lead to further significant changes of the result. The detailed structure of the ocean currents achieved by the Rifugio modelling approach was already contained in the GRACE data and its error covariance!

However, given the higher accuracy and resolution of the GOCE data, an a posteriori error estimate would be highly reduced by the new MDT data. Currently, this cannot be computed for the IFEOM solutions, but would be possible by the iterative

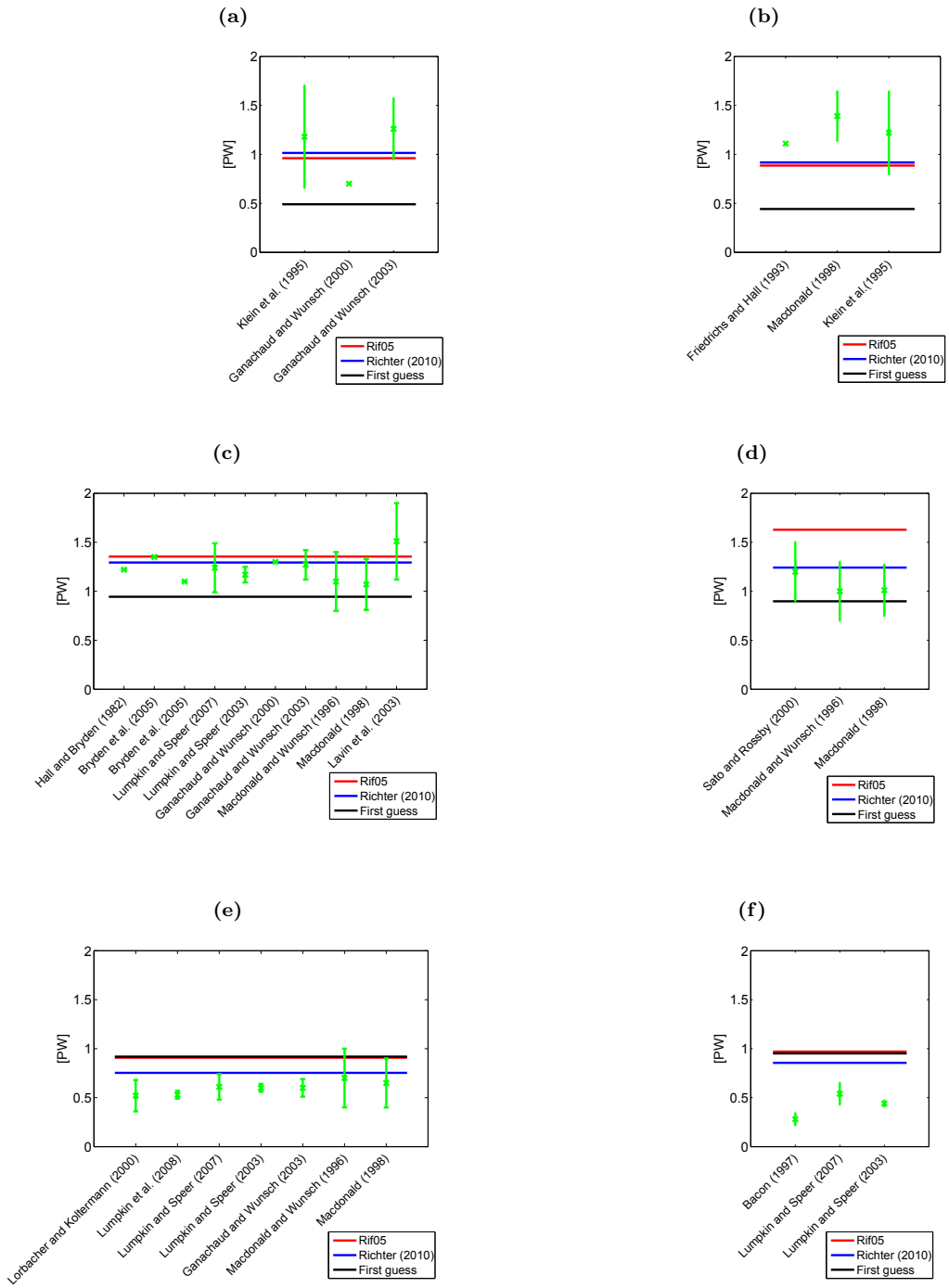

Fig. 4.14: Heat transports across different latitudinal sections and comparison to other estimates: (a) Heat transports across 7°N-8°N, (b) Heat transports across 11°N-14.5°N, (c) Heat transports across 24°N-25°N, (d) Heat transports across 36°N, (e) Heat transports across 47°N-48°N, (f) Heat transports across 55°N-60°N. The estimate of Rif05 is almost identical to those of the first guess in (e) and (f).

inversion technique described by Yaremchuk and Nechaev (2001). Therefore, setting up of the Hessian matrix of the cost function will be the next step in the future work with the IFEOM model.

Reconsidering the weighting process described at the beginning of this chapter, another finding is the superiority of the MPV (Minimum Penalty Variance) approach (section 4.2.1.4) over the MME (Maximum Model Entropy) approach (section 4.2.1.5). This must not be true in general, but in our case it shows that the satellite data are actually good enough to be weighted heavily. The ocean model IFEOM draws large benefit from the thoroughly processed satellite MDT.

MOC [Sv]	maximum	24°N	25°N	26.5°N	48°N	56°N
Rif05	**23.7**	**20.4**	**21.0**	**22.7**	**19.4**	**14.7**
Richter (2010)	23.0	19.9	20.4	21.7	17.2	12.7
Msadek et al. (2010)	20-29					
Lumpkin and Speer (2007)		18.0±2.5			*16.3±2.7*	17.0±4.3
Köhl and Stammer (2008)			*12-17*		13-20	
Cunningham et al. (2007)				18.7±5.6		
Talley et al. (2003)	*18±(3-5)*					

Table 4.3: Meridional Overturning Circulation estimates of different authors. Those which *do not* agree with the Rif05 solution are shown *in italics*.

4.3 Further analysis of the results

In this section, at first the goodness of fit of the IFEOM model is investigated. Afterwards, the MDT error covariance and its influence on the model result is analysed. Finally, the two most promising IFEOM solutions, Rif05 and RifCov3-45, are compared to the CLS09 MDT.

4.3.1 Goodness of fit

The iterative optimization process in the ocean model IFEOM must not necessarily converge to a meaningful result. This may be due to false prior modelling assumptions, inconsistent data sets, inappropriate error estimates or simply numerical issues. Therefore the model result has to be checked carefully. The following sections present different approaches for evaluation of the goodness of fit.

4.3.1.1 Decrease of cost function

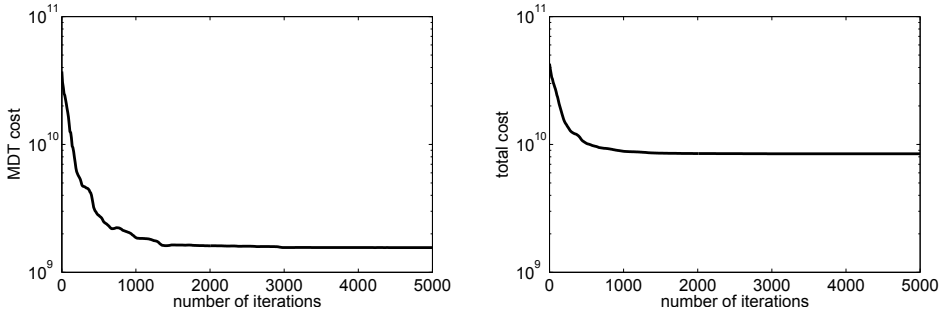

Fig. 4.15: Decrease of the IFEOM cost function

As shown in figure 4.15, the IFEOM cost function decreases considerably during the first 2000 iterations. At each model run, 5000 iterations are conducted to ensure that a minimum is found. However, no big changes occur in the second half of the optimization.

4.3.1.2 χ^2 statistic

From a meaningful optimization, we expect the posterior model-data deviations to be significantly smaller than the a priori assumed errors. As the inverse squared prior errors represent the weights used in the cost function, it is required that each term of the cost function

$$\begin{aligned} 2 \cdot J_i &= (\text{data} - \text{model})_i^T \mathbb{W}_i (\text{data} - \text{model})_i \\ &= (\text{data} - \text{model})_i^T (\text{prior error})_i^{-2} (\text{data} - \text{model})_i \end{aligned} \tag{4.26}$$

be close to zero after the optimization. More precisely, a normal distribution with mean 0 and variance 1 is expected for each term $(\text{prior error})_i^{-1}(\text{data} - \text{model})_i$. This

leads to a cost function $2 \cdot J = \sum_{i=1}^{N} 2 \cdot J_i$ that is χ^2_{N-M} distributed with $N - M$ degrees of freedom (Bennett, 2002). Here, N denotes the total number of adjusted data values including additional assumptions, thus the total number of terms in the cost function J. The number of adjustable model parameters is represented by M, and thus the degrees of freedom in the Rif05 model run sum up to $N_{\text{Rif05}} - M$ =603735. We get $\chi^2_{603737} = 8447.6$, and the probability of this χ^2_{603737} value is 0.99999995.

In this optimization test, the null hypothesis is that the model ocean differs from the observational data only within the assumed errors. With a χ^2 probability of 0.99999995, the null hypothesis cannot be rejected at any reasonable level of significance. This means that it is not possible to demonstrate inconsistency of data and model by this statistical test. However, by definition of the method, no positive statement about consistency can be made either.

Theoretically, the expected value of χ^2_{N-M} equals the degrees of freedom: $E(\chi^2_{N-M}) = N - M$. In the case of IFEOM, there is a large difference between the χ^2 test value and the number of degrees of freedom. On the one hand, this might be due to the choice of the prior errors (weighting factors) which is critical for the optimization process as shown in section 4.2.2. Other weighting factors produce very different results. Our result suggests that the prior errors may have been chosen too large and could even be reduced. But this option must be considered very carefully as it might only be a statistical effect as shown in Steinkamp (2011).

On the other hand, the difference is also a consequence of the good model adjustment already before adding the MDT data. The corresponding model weights and parameters had already been balanced carefully by Richter (2010). His IFEOM model run without MDT serves as a first guess for our experiments, using $N_{\text{first guess}} - M =$ 599070 theoretical degrees of freedom. This results in a final cost function value of $2 \cdot J(\hat{Y}) = 4328.0$, with a probability of 0.99999997. Now 4665 MDT terms are added to the cost function and the number of degrees of freedom is increased by 4665. The first guess is already a good estimate (see 4.1.4) which is not modified to a very large extent by the additional MDT data. Therefore the χ^2 test is also not expected to deviate considerably from the one of Richter's (2010) estimate.

However, the $N_{\text{first guess}}$ different cost function terms do not represent independent data points as it is required for a true χ^2 distribution. Atlas data of temperature and salinity were smoothed, interpolated and adjusted to the ocean physics before. Therefore, also the residuals for the advection-diffusion equations are not independent any longer. The velocity data are an output of the forward model run with the same temperature T and salinity S. Smoothness conditions for T and S are implemented as additional constraints in extra equations which could also be done in terms of an error covariance, leading to $2 \cdot$ number of nodes = 234328 degrees of freedom less. For these reasons, the "effective" degrees of freedom are much less in the IFEOM model and uncertain to determine (for more general information on effective degrees of freedom, consider e.g. Emery and Thomson, 2001).

Because the true number of effective degrees of freedom is not known, the following thought experiment is conducted: The smallest possible number of degrees of freedom is assumed for Richter's (2010) model run such that it is just not possible to reject the null hypothesis on a 5 percent level of significance (0.05). This is

	first guess	Rif05, $\alpha = 7$	Rif05, $\alpha = 1$	MDT term, $\alpha = 7$	MDT term, $\alpha = 1$
N	833398	838063	838063	4665	4665
$N - M$	599070	603735	603735	4665	4665
$\tilde{N} - M$	4483	9148	9148	N/A	N/A
χ^2	4328.0	8447.6	13900.0	1560.6	4756.1

Table 4.4: Comparison of the IFEOM model solution Rif05 with $\alpha = 7$ and $\alpha = 1$ to the first guess in terms of χ^2 statistics.

$\tilde{N}_{\text{first guess}} - M = 4483$ with a probability of 0.95043977. Keeping these "imaginary" degrees of freedom in mind and adding the MDT data to the optimization results in $\tilde{N}_{\text{Rif05}} - M = 4483 + 4665 = 9148$ final degrees of freedom. Thus $\chi^2_{9148} = 8447.6$ has a probability of 0.99999992. This shows that assimilation of the MDT data set in the Rif05 model run with $\alpha = 7$ does not contribute to possible rejection of the null hypothesis. In contrast, the Rif05 model run with $\alpha = 1$ results in $\chi^2_{9148} = 13900$ with a probability of 0. Thus we can reject the null hypothesis even at a level of significance of $10^{-7}\%$ or higher. The weighting factor $\alpha = 1$ has produced an improbable result and has led to inconsistency of data and model.

Now, the changes that are implied by the additional MDT data set are investigated. Adding 4665 degrees of freedom to the model leads to an increase of the cost function by $8447.6 - 4328.0 = 4119.6$ (difference Rif05 solution - first guess). The χ^2 test is now applied separately to this increase of the cost function. For 4665 additional degrees of freedom, the test results in a probability of 0.99999997 showing a good statistical agreement of the new data set and the prior model (first guess). Even assuming very few effective degrees of freedom for the first guess solution so that this model would be rejected without any additional data, the addition of the MDT data still converts the fit into a good one that passes the hypothesis test with exceptionally high probability.

The χ^2 test is now executed separately for the MDT part of the cost function. With the weighting factor $\alpha = 7$ used in this study, the χ^2 test value is 1560.6 for 4665 degrees of freedom, leading to a probability of 0.99999998. Therefore, rejection is again not possible and the optimization was performed successfully. In contrast to this, consider a model run without additional MDT weighting factor ($\alpha = 1$). In this case, a χ^2 value of 4756.1 is computed for the same number of degrees of freedom. Although the null hypothesis cannot be rejected at a high level of significance in this case (only at significance level 0.2, given the 20% chance of a wrong decision), it shows that optimization was less successful. For a higher number of grid points, the model-data difference could not be reduced below the threshold given by the prior errors. This confirms our choice of the weighting factor $\alpha = 7$ from section 4.2.2.

The numerical values according to these findings are summarized in table 4.4.

4.3.1.3 R^2 statistic

We calculate an approximation of the coefficient of determination R^2 for the Rif05 solution:

$$R^2 \equiv 1 - \frac{\text{residual sum of squares}}{\text{total sum of squares}} \approx 1 - \frac{\text{residual sum of squares}}{N \cdot (\text{sample variance})} \quad (4.27)$$
$$= 1 - \frac{2 \cdot J(\hat{Y})}{N} = 0.9899.$$

This can be interpreted as "98.99% of the overall variance are explained by the model" whereas in the first guess solution without MDT 99.48% of the variance are explained. The adjusted $\bar{R}^2$ accounts for the number M of adjustable model parameters and gives:

$$\bar{R}^2 = 1 - (1 - R^2) \cdot \frac{N-1}{N-M} = 0.9860 \quad (4.28)$$

meaning 98.60% of variance are explained by the model (99.28% for the first guess solution without MDT). The numerical values are summarized in table 4.5. They show that the use of additional MDT data in the Rif05 model runs changes the amount of explained variance only to a minimal extent. The statistical properties of the model are not deteriorated by the additional data set. More detailed explanation and derivation of the R^2 statistic are given in Draper and Smith (1981).

	first guess	Rif05, $\alpha = 7$	Rif05 $\alpha = 1$
R^2	0.9948	0.9899	0.9834
$\bar{R}^2$	0.9928	0.9860	0.9770

Table 4.5: Comparison of the IFEOM model solution Rif05 with $\alpha = 7$ and $\alpha = 1$ to the first guess in terms of R^2 statistics.

The coefficient of determination R^2 can be regarded as a squared correlation coefficient between the regressors and the outcomes, thus the observed and the modelled values. Therefore $R^2 \in [0, 1]$ is a measure of goodness of fit, and the high value can show that the IFEOM model is perfectly suitable to explain the data variation. In contrast, it could also mean that the prior errors have been chosen too large, a possibility already mentioned in section 4.3.1.2.

However, the values of R^2 depend on the knowledge of the correct number of independent data values N and on the actual applicability of the approximation in 4.27. The correct number of N cannot be determined due to the large amount of additional constraints in the ocean model, and the approximation 4.27 is questionable as there are dependencies among the different data sets and large differences between the error variances. Therefore this method is not reliable in our case. Additionally, the actual information content of the coefficient of determination is emphatically argued about, see e.g. Achen (1982): "But it makes little sense to base decisions on a statistic that [...] measures nothing of serious importance."

Therefore, this subject is not extended here, but the section is closed with the remark that the high percentage of explained variance from the first guess is almost preserved when the MDT data set is added in the Rif05 model run. It can be concluded that the model explains the MDT data variance as well as the variance of the other data sets used in the optimization.

In summary, we should avoid "diagonal" weighting.

Andrew F. Bennett

4.3.2 Impact of the covariance

Adding an estimate of error *co*variance to the usual estimate of error variance has several important implications that are discussed in this section. The probably most obvious one is the smoothing effect. The geodetic MDT is intentionally very rough, because the relevant smoothness information is contained in the error covariance estimate. The covariance matrix is inverted before it is used as a weighting matrix in the optimization process. Therefore, the diagonals of the resulting weighting do not equal the inverse variances as it is the case with a diagonal variance-covariance-matrix. Thus the off-diagonals of the covariance matrix do not only impact the mixed MDT terms in the cost function by the off-diagonals of the weighting matrix, but also the quadratic terms via the diagonal components of the inverse covariance matrix.

4.3.2.1 Diagonal weights

Introducing covariances does not only change the off-diagonals of the weighting matrix, but also the diagonal. In our case with the Rifugio covariance matrix, diagonal weights become much higher: Inverting the covariance matrix without off-diagonals leads to a mean diagonal weight of $165.3\,\mathrm{m}^{-2}$ and a maximal diagonal weight of $318.6\,\mathrm{m}^{-2}$. Inverting the full covariance matrix results in a mean diagonal weight of $1238.9\,\mathrm{m}^{-2}$ and a maximal diagonal weight of $3001.8\,\mathrm{m}^{-2}$.

This means not the actual mean variance of $0.008\,\mathrm{m}^2$ is used in the optimization, but an "effective" mean variance induced by the off-diagonals of $0.002\,\mathrm{m}^2$. The mean standard deviation is decreased from 8.44 cm to an "effective" value of 3.55 cm, see also table 4.6.

Thus the adaptation of the model to the MDT data is much stronger in the non-diagonal case with nonzero off-diagonals. The ratio of the mean diagonal weights in both cases is

$$\frac{1238.9\,\mathrm{m}^{-2}}{165.3\,\mathrm{m}^{-2}} = 7.49.$$

In the diagonal case we can therefore omit the weight decreasing factor $\alpha = 7$ and still get a reasonable (not overweighted) result! For comparison, we even have to set $\alpha = 1$, so that in both cases the MDT is weighted similarly and the only difference are the off-diagonal terms. This IFEOM model run with diagonal covariance matrix and weighting factor $\alpha = 1$ is named RifCov1 and is shown in figure 4.16a. It can be seen that the impact of the MDT data is less in the RifCov1 solution, although the weighting factor α was omitted.

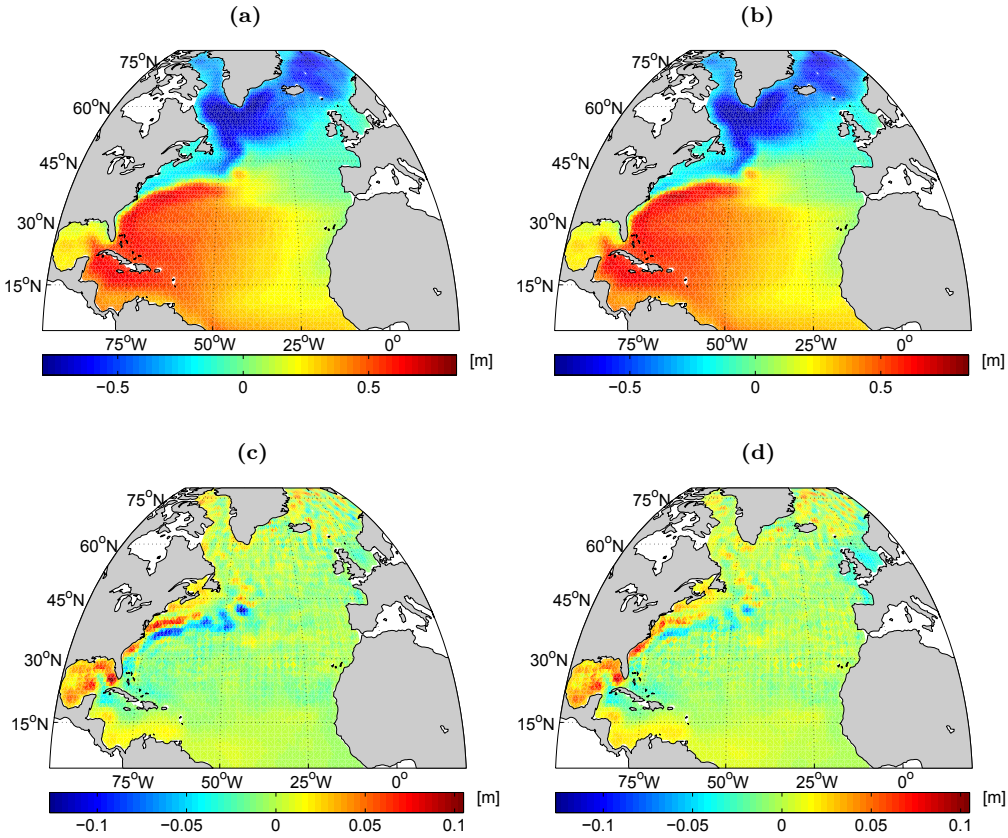

Fig. 4.16: Impact of the error covariance on the optimization: subplots on the left hand side show the result when only the variance (diagonal of the covariance matrix) is used, those on the right hand side show the result when only the diagonal of the weight matrix is used. (a) RifCov1 MDT, (b) RifCov2 MDT, $\alpha = 7$, (c) MDT difference: RifCov1 - Rif05, (d) MDT difference: RifCov2 - Rif05

The reason for these changes of the diagonal weights is the modified spectrum of the covariance matrix. Adding covariances to our diagonal matrix increases the largest eigenvalue and decreases the lowest which results in a smaller determinant compared to the diagonal matrix's one and therefore increases diagonal weights when the inverse is calculated.

The diagonals are weighted differently than before because the observations are not independent any more. Only by a rotation of the observations, diagonal weights can be applied and interpreted as inverse variances again. This can be done by a singular value decomposition (Olbers, 1989); but this is not useful for our model because it has several other components that we want to keep in their respective coordinate system.

However, rather than by algebraic theory, the IFEOM model seems to be influenced mostly by the changes in the diagonal weights. This is not surprising considering the mean absolute value of the off-diagonals which is $1.9537\,\mathrm{m}^{-2}$ compared to the

diagonal mean value of $1238.9\,\mathrm{m}^{-2}$. This difference in scale ($\frac{1238.9\,\mathrm{m}^{-2}}{1.9537\,\mathrm{m}^{-2}} = 634.1301$) determines what is more important in the reduction of the cost function. The reason for this difference in scale could be the small covariances compared to the variances. Increasing the covariances by a constant factor of 1.5 for example results in a much smaller mean diagonal/ off-diagonal weight ratio when the diagonal is kept constant: $\frac{205.5782\,\mathrm{m}^{-2}}{175.1705\,\mathrm{m}^{-2}} = 1.1736$. With this ratio, it would be more likely that the covariances actually impact the optimization apart from diagonal weighting strength.

In order to prove that the most important impact of the error covariances is the diagonal weighting, another IFEOM model run was conducted. Only the diagonal of the original weighting matrix was used and the off-diagonal weights were simply set to zero. The result is called RifCov2 and is shown in figure 4.16b. It is expected not to differ largely from the Rif05 solution if the assumption is true that the off-diagonals of the weighting matrix have only small impact on the solution. The difference to the Rif05 solution is presented in figure 4.16d. Differences are much smaller than those between RifCov1 and Rif05 which are presented in figure 4.16c. This shows that the error covariance induced changes to the diagonal of the weighting matrix are much more important than those to the off-diagonal entries of the weighting matrix.

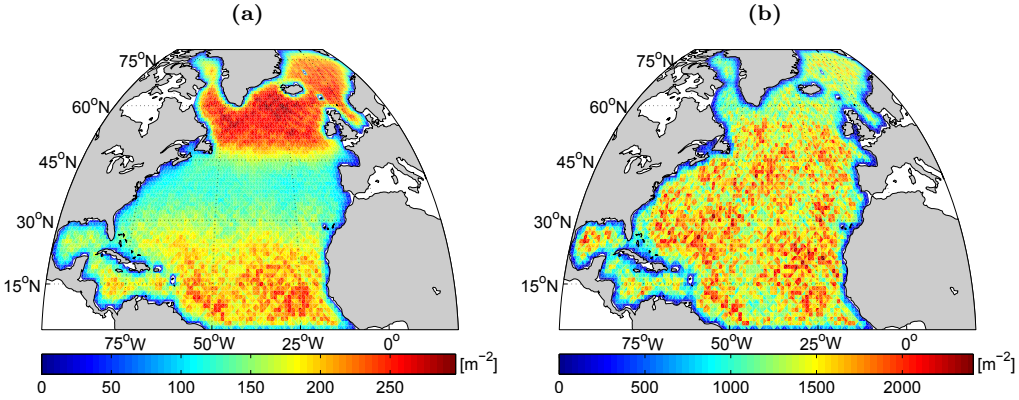

Fig. 4.17: (a) Inverse of the diagonal of the Rifugio MDT error covariance matrix, (b) Diagonal of the Rifugio weighting matrix $\mathbb{P}$.

Both diagonals of the diagonal weighting matrices used in the experiments RifCov1 and RifCov2 are shown in figure 4.17. It is obvious from figure 4.17a that inverting only the diagonal of the covariance matrix results in unrealistic weights. It is very unlikely that there is a physical reason for the weights being constantly higher between 45°N and 75°N than anywhere else in the North Atlantic. Satellite tracks are closer together at high latitudes. This may reduce the error variances, but will increase the error covariance due to aliasing effects. Inverting the full error covariance leads to the diagonal weights shown in figure 4.17b. High latitudes do not stand out here and a small impact of the major topographic features on the MDT error estimate can be recognized such as the Mid-Atlantic Ridge, Bermuda Rise, Cape Verde islands. In the areas of the abyssal plains, weights are generally highest and corresponding variances therefore smallest. This physically more reasonable estimate confirms that error covariances cannot be neglected due to their influence on the diagonal weights.

4.3.2.2 Smoothing

As already claimed in section 4.2.5, the MDT error covariance leads to smoothing of the MDT in the optimization. The experiment RifCov1 using the diagonal of the covariance matrix for weighting was also performed to demonstrate this (see figure 4.16a).

Apart from the more pronounced Gulf stream and Mann Eddy in the original Rif05 solution (with full covariance), the differences are small. Regarding smoothness, the differences increase with latitude, where the solution with diagonal weights is rougher. As already seen in section 4.2.5, a meridional striping effect becomes apparent in figure 4.16c. However, the effect is small given the high smoothness of the Rifugio solution which is due to incorporating very smooth climatology data and also to implying explicit smoothness conditions in the IFEOM ocean model. These parts of the model possibly hide the oscillations in the MDT data, so that a rougher ocean model would perhaps be more suitable in this case to analyse the smoothness effects of the MDT error covariance.

That is why we have a closer look at the MDT data (figure 4.18a) and its covariance. The MDT data are so rough that they are usually not presented alone, but only in combination with their covariances (e.g. assimilated into an ocean model already). We are now looking for a smoothing operator $\mathbb{S}$, such that $\mathbb{S}$ applied to the MDT data set looks smooth as e.g. the MDT shown in figure 4.18b. Additionally, we would like to keep the fine spatial structures of the data and lose as less information as possible. This leads to the thoughts presented in the following.

Let the cost function term for the MDT be given by

$$f_{\mathrm{MDT}} = x^T \mathbb{P} x$$

with the model-data difference $x = x_{\mathrm{data}} - x_{\mathrm{model}}$ and the weighting matrix $\mathbb{P} = \mathrm{inv}(\mathrm{COV})$ being the inverse error covariance matrix. Then, due to symmetry and positive definiteness of $\mathbb{P}$, we can decompose it in a unique way such that

$$\mathbb{P} = \mathbb{S}^T \cdot \mathbb{D} \cdot \mathbb{S} \tag{4.29}$$

where $\sqrt{\mathbb{D}} \cdot \mathbb{S}$ is the matrix square root of $\mathbb{P}$. The diagonal matrix $\mathbb{D}$ is determined such that each row of $\mathbb{S}$ sums up to one, so that $\mathbb{S}$ can be applied to the MDT as a smoothing filter. In this way the inverse-covariance-weighted rough MDT term $f_{\mathrm{MDT}} = x^T \cdot \mathbb{P} \cdot x$ becomes the diagonally weighted smooth MDT term

$$f_{\mathrm{MDT}} = (\mathbb{S} \cdot x)^T \cdot \mathbb{D} \cdot (\mathbb{S} \cdot x). \tag{4.30}$$

The filter $\mathbb{S}$ is shown for some arbitrarily chosen locations in figure 4.19. It is bell-shaped with a half width of approximately one degree latitude and longitude, respectively. There is some significant negative part in about three degrees distance from the maximum. The filter $\mathbb{S}$ is not isotropic, but exhibits about 5 almost longitudinal stripes overlapping with the approximately isotropic circular structure of the bell.

The method of decomposing $\mathbb{P}$ and applying 4.30 in the ocean model optimization has a major advantage: The smoothing filter $\mathbb{S}$ is directly determined from the data themselves. There is no artificial filtering applied with estimated filter width and

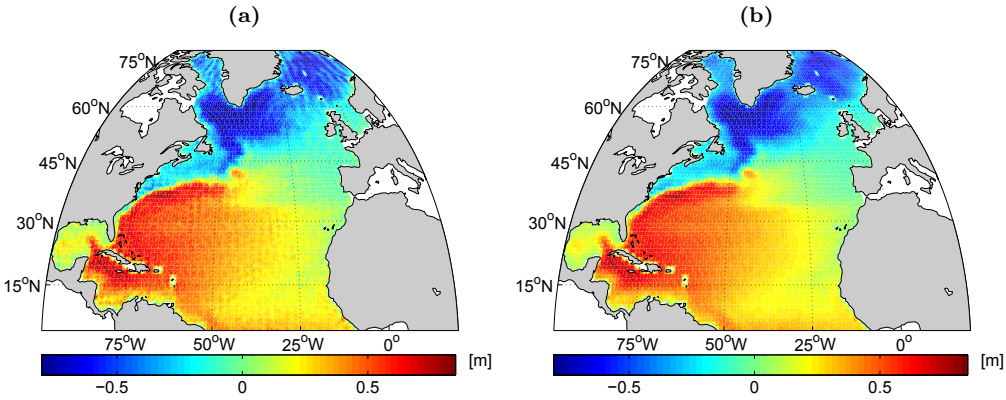

Fig. 4.18: Impact of the error covariance on smoothing of the satellite MDT, shown on the example of the Rifugio MDT data: (a) Rifugio MDT x_{data} without smoothing, usually not shown this way, (b) Rifugio MDT smoothed by row-normalized square root of inverse error covariance: $\mathbb{S}x_{\text{data}}$.

shape as for example in Knudsen et al. (2011); Jayne (2006); Bingham et al. (2008) and others. In the standard filtering procedure, a smoothing radius is guessed mostly from visual inspection without knowing how much of the actual signal content is lost. In the Rifugio approach, no part of the signal is lost, but in contrary evaluated in the assimilation of the data.

Applying this decomposition however smoothes not only the MDT data, but actually the difference $x = x_{\text{data}} - x_{\text{model}}$ between data and model. Therefore it has to be analysed whether

$$\mathbb{S}x = \mathbb{S}(x_{\text{data}} - x_{\text{model}}) = \mathbb{S}x_{\text{data}} - \mathbb{S}x_{\text{model}}$$

leads to unwanted smoothing of the model MDT x_{model}.

At the beginning of the optimization, the modelled MDT x_{model} is the first guess MDT. Hence the smoothing operator is applied to the first guess MDT and the resulting difference is presented in figure 4.20. It can be seen that the smoothing operator mainly affects the boundaries of the model domain. However, the MDT error is large along the coastlines and thus the corresponding weights are small. Therefore the coastal MDT is not important in the calculation and we focus on the open ocean. Here, differences are again largest in the high latitudes and along the Gulf Stream. The mean difference between the smoothed and the unsmoothed first guess MDT equals 7.4 mm. The impact of smoothing or not smoothing the modelled MDT on the optimization is analysed in the next section.

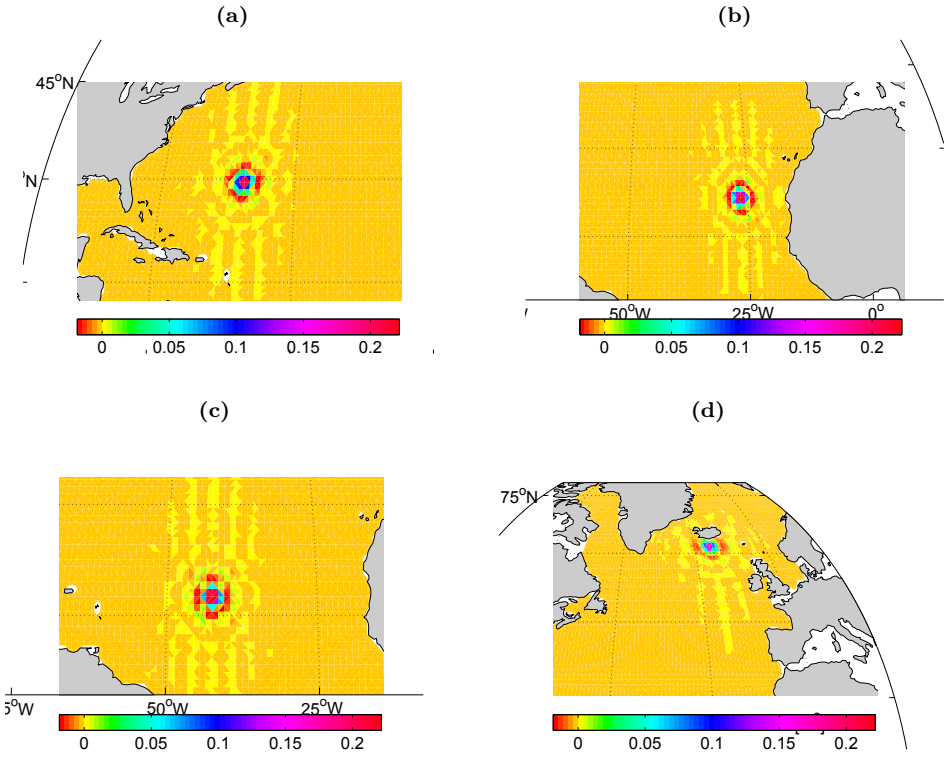

Fig. 4.19: Filter $\mathbb{S}$ for different locations in the North Atlantic, (a) east of Florida, (b) west of Africa, (c) between the Caribbean and Africa, (d) directly south of Iceland.

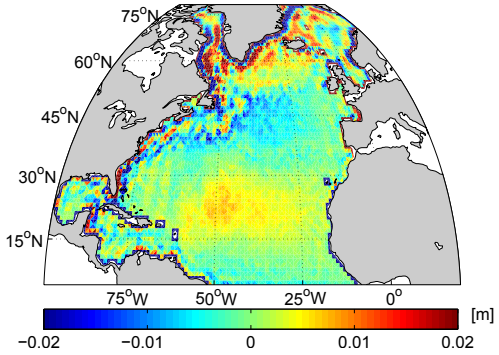

Fig. 4.20: Impact of the error covariance on smoothing of the first guess: Difference between smoothed and unsmoothed first guess MDT

4.3.2.3 Revising the normal equations

In the previous section, the weighting matrix $\mathbb{P}$ was decomposed into $\mathbb{P} = \mathbb{S}^T\mathbb{D}\mathbb{S}$. Maintaining the original cost function term f_{MDT} then leads to smoothing of both the MDT data and the modelled MDT. In this section, the idea is pursued that the smoothness information belongs to the MDT data only. It is analysed whether interpreting $\tilde{x}_{\mathrm{data}} = \mathbb{S}x_{\mathrm{data}}$ as the new data set is consistent with the geodetic normal equations. Furthermore, applying the smoothness operator $\mathbb{S}$ to x_{data} but not to x_{model} will modify the cost function and therefore also change the result of the optimization.

The MDT data x_{data} and their respective weighting matrix $\mathbb{P}$ originate in the geodetic normal equations (see section 2.4.2):

$$\mathbb{P}x_{\mathrm{data}} = n$$

This system of equations was set up in order to solve the best fit problem of

$$\mathbb{A}x_{\mathrm{data}} = l + v, \text{ with } \Sigma \tag{4.31}$$

where l are the actual satellite observations with errors v. The covariance for v is known and given by Σ. The system matrix $\mathbb{A}$ does not need to be quadratic, and equations (4.31) are solved by a least-squares fit:

$$\begin{aligned} \underbrace{\mathbb{A}^T\Sigma^{-1}\mathbb{A}}_{=:\mathbb{P}} x_{\mathrm{data}} &= \underbrace{\mathbb{A}^T\Sigma^{-1}l}_{=:n} \\ \mathbb{P}\quad x_{\mathrm{data}} &= n \end{aligned}$$

An identity matrix $\mathbb{I} = \mathbb{S}^{-1}\mathbb{S}$ is now inserted into equation (4.31):

$$\underbrace{\mathbb{A}\mathbb{S}^{-1}}_{=:\tilde{\mathbb{A}}}\underbrace{\mathbb{S}x_{\mathrm{data}}}_{=:\tilde{x}_{\mathrm{data}}} = l + v, \text{ with } \Sigma \tag{4.32}$$

and the resulting system is solved:

$$\tilde{\mathbb{A}}\tilde{x}_{\mathrm{data}} = l + v, \text{ with } \Sigma \tag{4.33}$$

As above, this leads to

$$\tilde{\mathbb{A}}^T\Sigma^{-1}\tilde{\mathbb{A}}\tilde{x}_{\mathrm{data}} = \tilde{\mathbb{A}}^T\Sigma^{-1}l$$

Replacing $\tilde{\mathbb{A}} = \mathbb{A}\mathbb{S}^{-1}$ again gives:

$$\mathbb{S}^{-T}\underbrace{\mathbb{A}^T\Sigma^{-1}\mathbb{A}}_{=\mathbb{P}}\mathbb{S}^{-1}\tilde{x}_{\mathrm{data}} = \mathbb{S}^{-T}\mathbb{A}^T\Sigma^{-1}l =: \tilde{n}$$

Remembering the decomposition $\mathbb{P} = \mathbb{S}^T\mathbb{D}\mathbb{S}$ and inserting it into the previous equation results in

$$\begin{aligned} \mathbb{S}^{-T}\mathbb{P}\mathbb{S}^{-1}\tilde{x}_{\mathrm{data}} &= \tilde{n} \\ \mathbb{S}^{-T}\mathbb{S}^T\mathbb{D}\mathbb{S}\mathbb{S}^{-1}\tilde{x}_{\mathrm{data}} &= \tilde{n} \\ \mathbb{D}\tilde{x}_{\mathrm{data}} &= \tilde{n} \end{aligned}$$

We now solve for the new MDT data $\tilde{x}_{\text{data}}$ with the new weighting matrix $\mathbb{D}$. Therefore the geodetic normal equations are consistent with the new interpretation of the MDT data $\tilde{x}_{\text{data}} = \mathbb{S}x_{\text{data}}$ if $\mathbb{D}$ is used as weighting matrix in the cost function term:

$$\tilde{f}_{\text{MDT}} = (\tilde{x}_{\text{data}} - x_{\text{model}})^T \mathbb{D} (\tilde{x}_{\text{data}} - x_{\text{model}}) \tag{4.34}$$

The new cost function, including the term $\tilde{f}_{\text{MDT}}$ was used for the computation of two more optimization results. First, the same weighting factor as before, $\alpha = 7$, was applied. The resulting Meridional Overturning Circulation and the meridional heat transports are given in figure 4.21. On the Southern boundary, the overturning circulation is too strong, probably resulting from an inconsistency with the prescribed boundary condition as in Richter (2010).

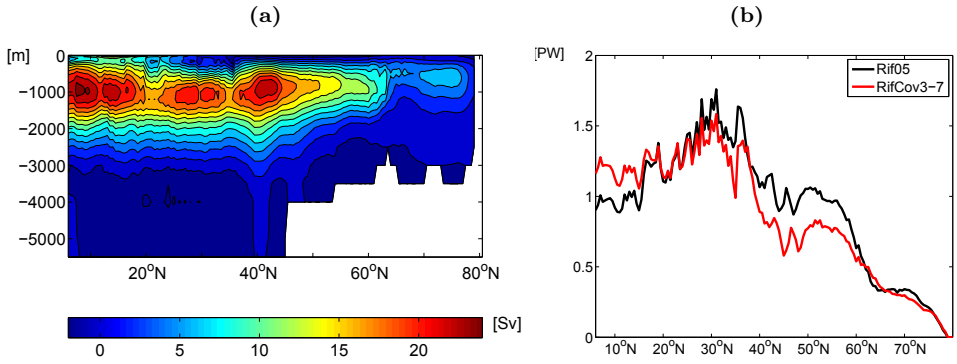

Fig. 4.21: Selected oceanographic features of RifCov3-7 solution: (a) Meridional Overturning Circulation for solution RifCov3-7, (b) Heat transports for RifCov3-7 solution in comparison with heat transports of Rif05 solution.

However, a new cost function needs a new determination of the weighting factor α. Thus the MPV approach (section 4.2.1.4) was employed again and provides the new weighting factor $\alpha = 45$ at the point of minimum penalty variance (see figure 4.22). The results of these two model runs are called RifCov3-7 and RifCov3-45, respectively. An overview of the IFEOM solutions RifCov1 to RifCov3 is given in table 4.6.

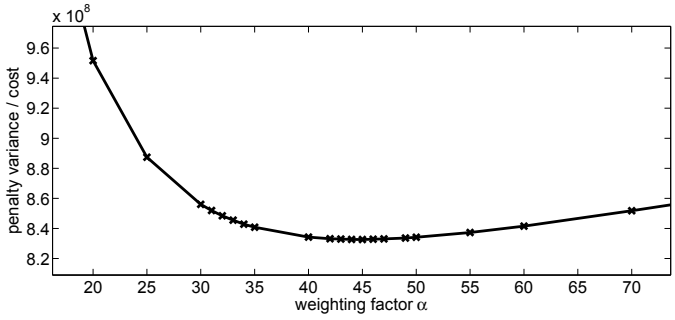

Fig. 4.22: Penalty variance normalized by overall cost in dependence of weighting factor α for the new cost function including $\tilde{f}_{\text{MDT}}$.

	Rif05	RifCov1	RifCov2	RifCov3
weighting matrix	$\mathbb{P}$	$\frac{1}{\text{diag(COV)}}$	diag($\mathbb{P}$)	$\mathbb{D} = \mathbb{S}^{-T}\mathbb{P}\mathbb{S}^{-1}$
mean diagonal weight [m^{-2}]	1238.9	165.34	1238.9	5269.6
mean MDT variance [m^2]	0.002	0.0080	0.002	0.00079
mean MDT standard dev. [m]	0.0355	0.0844	0.0355	0.0191
smoothing of MDT	error	none	none	data

Table 4.6: Comparison of the IFEOM model solutions RifCov1, RifCov2 and RifCov3 with Rif05.[2]

The solution RifCov3-45 is presented in figure 4.23. In comparison to the Rif05 solution, the Gulf Stream is shifted northwards (see figure 4.23a). The Meridional Overturning Circulation (figure 4.23c) is significantly weaker at low latitudes which underlines the its maximum between 40°N and 45°N. This modification in the result enhances agreement with other authors (Wunsch, 2002; Köhl and Stammer, 2008; Griffies et al., 2009). This change is also reflected in the heat transports (figure 4.23d). With the weighting factor $\alpha = 45$, heat transports are smaller at low latitudes, but almost unchanged at high latitudes.

A comparison of heat transports of the solutions Rif05, RifCov3-7 and RifCov3-45 with the First guess is shown in figure 4.24. In terms of meridional heat transports, the solution RifCov3-45 is the smoothest IFEOM solution that includes MDT data. From 7°N to 40°N, the RifCov3-45 heat transports are higher than the First guess estimates, but smaller than the other IFEOM solutions. At higher latitudes, they resemble the RifCov3-7 estimates which are smaller than the First guess and the Rif05 estimate between 40°N and 60°N and which are higher than the First guess estimates from 60°N northwards.

In figure 4.25, the different solutions are compared to heat transport estimates of other authors. At low and mid-latitudes, the RifCov3-45 heat transport estimates are lower than those of RifCov3-7. In particular at 11°N-14.5°N, the RifCov3-45 estimate is too small. All IFEOM solutions show good agreement with other estimates at 24°N-25°N. At 36°N, the RifCov3-45 estimate shows the best agreement of all IFEOM solutions with other estimates. At high latitudes, estimates of RifCov3-45 are higher than those of RifCov3-7, but still smaller than the Rif05 estimates. At 55°N-60°N however, all IFEOM estimates are too large. Because the heat transport estimates of other authors show a large spread and partly also large error bars, no statement can be made about superiority of one of the solutions over another by this comparison.

Altogether, the RifCov3-45 solution seems to be the best IFEOM result within this study, partly because of the smoothest heat transports, but primarily because of the improved representation of the Meridional Overturning Circulation.

[2]For illustration, the weighting matrix of the RifCov1 solution is written in a non-mathematical way. This weighting matrix is obtained from inverting the variances (diagonal of the covariance matrix) after the off-diagonals of the covariance matrix have been set to zero.

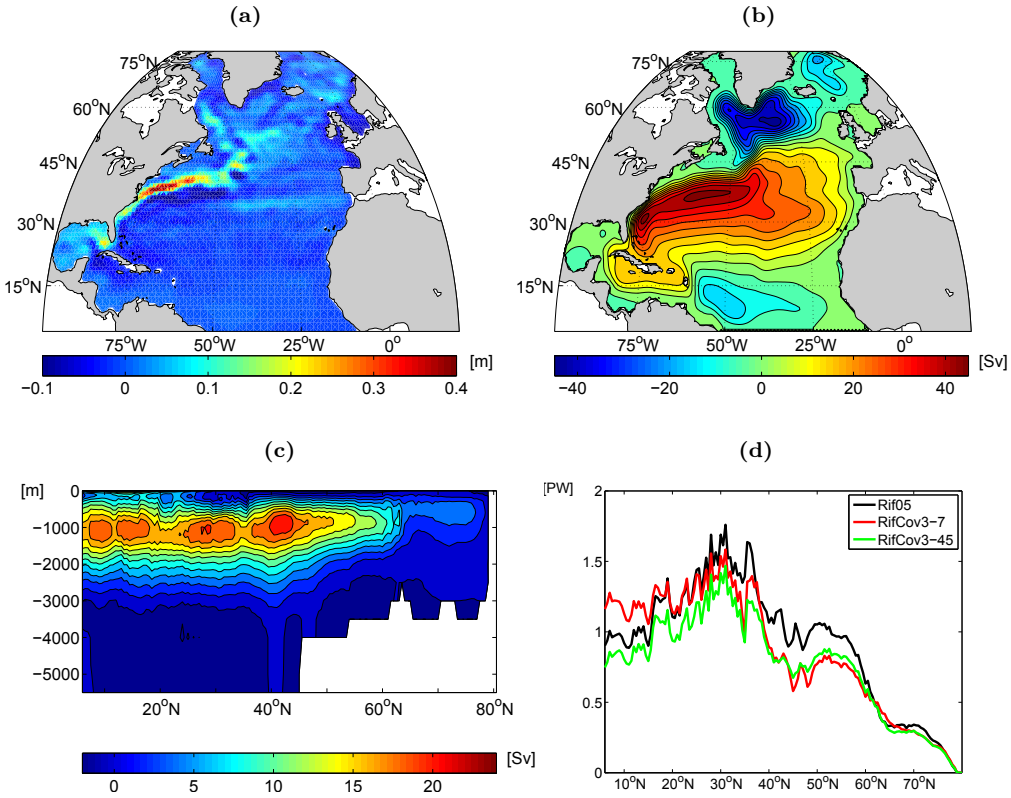

Fig. 4.23: Selected oceanographic features of RifCov3-45 solution: (a) MDT difference between RifCov3-45, and Rif05 solution, (b) Barotropic stream function of solution RifCov3-45, contour interval 2 Sv, (c) Meridional Overturning Circulation for solution RifCov3-45, (d) Meridional heat transports for RifCov3-45 solution.

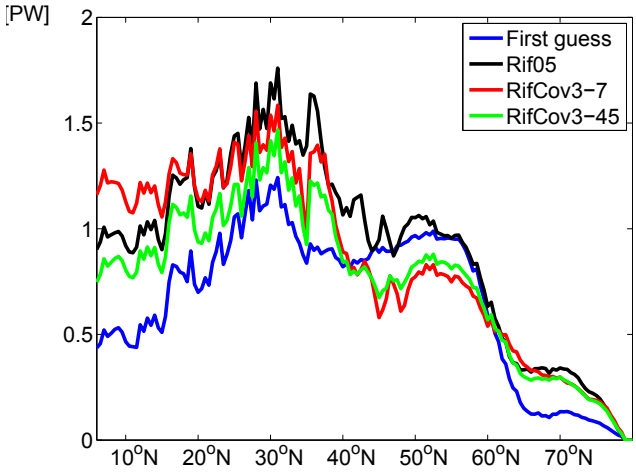

Fig. 4.24: Meridional heat transports.

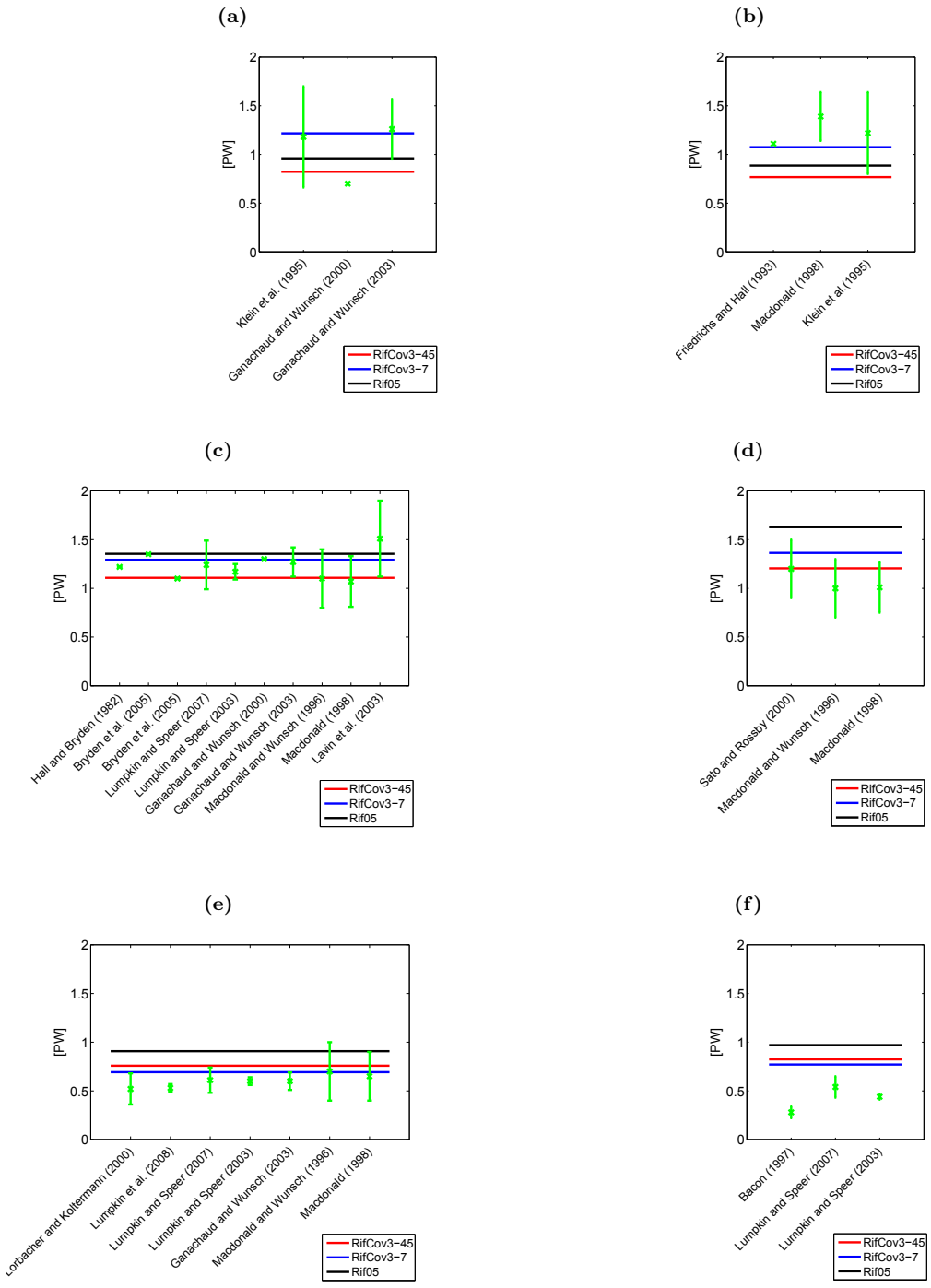

Fig. 4.25: Heat transports across different latitudinal sections and comparison to other estimates: (a) Heat transports across 7°N-8°N, (b) Heat transports across 11°N-14.5°N, (c) Heat transports across 24°N-25°N, (d) Heat transports across 36°N, (e) Heat transports across 47°N-48°N, (f) Heat transports across 55°N-60°N.

4.3.2.4 Shrinking the covariance matrix - an analogy to portfolio optimization

As the inverse covariance or weight matrix can be directly taken from the normal equations' coefficients, it suggests that the covariance matrix and its inverse are well known. It becomes obvious in section 4.2.3 that this assumption is not true. Both omission error models used in the approach Rif01 and Rif02 are equally possible just considering the available data. Only by inspection of the resulting model output, a decision is made which approach is to be preferred. So the covariance is at most determined up to an omission error model. The impact of this error model on the covariance and its inverse is large: The mean diagonal weight used in the Rif01 solution amounts to $45.8\,\mathrm{m}^{-2}$, the one used in the Rif02 solution $2387.3\,\mathrm{m}^{-2}$. Therefore, the error covariance description itself is not free from uncertainty.

A similar situation occurs in financial theory, when the best composition of portfolios is determined by an optimization. In this case, the covariance matrix of stock returns is required, but hardly known. The standard method is to compute a sample covariance matrix with an extreme amount of error due to insufficient data (Ledoit and Wolf, 2004). One approach for reducing the estimation error of the sample covariance matrix is weighted averaging with a covariance matrix estimator with a lot of structure imposed (Disatnik and Benninga, 2007). This so-called "shrinking target" matrix decreases the estimation error but creates a specification error. Therefore, the situation is a trade-off and the best proportion of the two components is again found by an optimization. The off-diagonal elements of the shrinkage estimator are usually moderated ("shrunk") compared to the typically large off-diagonal elements of the sample covariance matrix. The variance elements in the diagonal are kept untouched (Disatnik and Benninga, 2007).

The "constant correlation" shrinking target proposed in Ledoit and Wolf (2004) is applied to the Rifugio covariance matrix. The target T has the same variances as the covariance matrix COV and very small off-diagonals. The mean diagonal of the inverse of T is $165.6\,\mathrm{m}^{-2}$ which is very close to the diagonal covariance used in the RifCov1 model run. The mean diagonal weight of the inverted weighted average is given in figure 4.26. It remains to determine the "shrinkage constant" δ for the calculation of the weighted average $\mathrm{COV}_{\mathrm{shrink}} = \delta\mathrm{T} + (1-\delta)\mathrm{COV}$. A formula for the optimal shrinkage constant $\delta^\star$ is given in Ledoit and Wolf (2004). For the Rifugio covariance, a similar constant was determined in section 4.2.1: the weighting factor α, describing the trade-off between the given covariance matrix and the zero matrix.

Various other methods exist in finance theory for improving the poorly known covariance matrix (Disatnik and Benninga, 2007). Similar difficulties with the covariance matrices also arise in data assimilation problems using Ensemble Kalman Filters (EnKF) (e.g. Greybush et al., 2011; Hamill et al., 2001). A comparison of these methods exceeds the scope of this study, but will be done in the near future. The different fields of work will most likely benefit from more research on the connection between them.

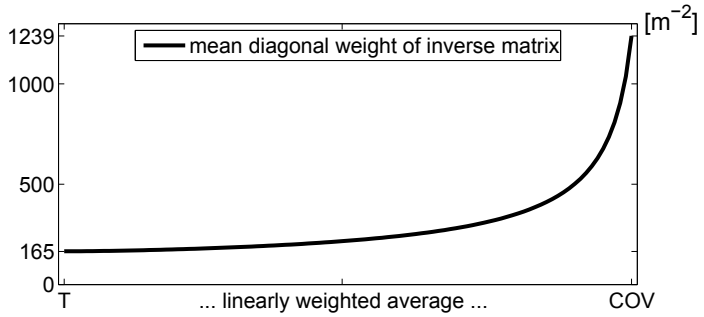

Fig. 4.26: Mean diagonal weight of the inverse of $\mathrm{COV}_{\mathrm{shrink}}$. From left to right, the shrinking constant δ is decreased linearly from 1 to 0.

4.3.2.5 Summary: Impact of the covariance

The main impact of the off-diagonal terms in the covariance matrix is the increase of diagonal weights in the inverse covariance (weight) matrix. As explained in section 4.3.2.1, this is not expected theoretically. A possible explanation may be an unusual ratio of variances and covariances.

The error covariance matrix contains some smoothness information for the MDT data as presented in figures 4.18 and 4.20. It is shown that this information can be extracted from the covariance matrix and be applied to the data directly. In this case, the smoothed MDT data is to be compared with the modelled MDT by means of a modified (inverse) error covariance matrix.

When decomposing the error covariance matrix and smoothing the MDT data by a part of it, one has to be aware of the origin of this information about data and error. It was shown that for consistency with the normal equations, the modified weighting matrix $\mathbb{D}$ has to be used instead of $\mathbb{P} = \mathbb{S}^T\mathbb{D}\mathbb{S}$.

The cost function is changed by this procedure, and thus a new weighting factor α has to be determined. By the MPV approach (section 4.2.1.4), $\alpha = 45$ is obtained.

The final solution, RifCov3-45, shows a significantly improved Meridional Overturning Circulation. No inconsistency can be observed on the Southern Boundary any longer, and meridional heat transports are the smoothest of all IFEOM solutions. Therefore, the results of this study suggest that a decomposition of the Rifugio inverse error covariance matrix is advantageous.

Uncertainties concerning the plausibility of the covariance matrix are not restricted to optimization in oceanography and geodesy (section 4.3.2.4). An example from financial optimization theory was presented in this section. Thus for further progress in this area of research, interdisciplinary cooperation should be launched.

4.3.3 Comparison to CLS09 MDT

A validation of our new MDT data sets Rifugio (satellite-only), Rif05 and RifCov3-45 (combined with ocean model IFEOM) is called for. This is not straightforward because

- The satellite GOCE delivers data of unprecedented accuracy (Steiger et al., 2010; Pail et al., 2010). Probably this data contains signals that could not be observed before and might deviate significantly from previous datasets. Comparison will reveal this but will not provide evaluation.
- The unsmoothed Rifugio MDT is the first unsmoothed MDT that was computed without any prior oceanographic information (Becker et al., 2012). On the contrary, almost all previously published MDT data sets contain hydrographic information. Any comparison has to take this difference into account.
- The Rifugio approach is the first method to compute a MDT without any extra filtering (Becker et al., 2012). All previously published MDT data sets contain specific artificial smoothness information. It is not clear which MDT (smoothed by a filter of a specified radius) the Rifugio MDT should be compared with.
- The Rifugio and Rif05 MDTs combine new data (GOCE) with a new method (Rifugio approach, section 2.4.2). Any difference to previous MDT data sets can possibly not be attributed clearly to one of the two new inputs.

The `CNES-CLS09_v1.1` MDT is chosen for a comparison because it is a recent product and easily available. `MDT_CNES-CLS09` was produced by CLS Space Oceanography Division and distributed by Aviso, with support from Cnes (`http://www.aviso.oceanobs.com/`). CNES-CLS09 incorporates 15 years of drifting buoy and CTD (conductivity-temperature-depth) data. An "optimal filtering" approach was utilised for data smoothing (Rio et al., 2011). This MDT is called "CLS09 MDT" in the following and is shown in figure 4.27d for the region of interest.

The formal error estimate for the CLS09 MDT is computed by multivariate objective analysis (Rio et al., 2011) and is shown in figure 4.28a. The smallness of the errors can be explained by the large amount of very accurate in-situ hydrographic data used. For comparing the MDTs, an error description of the Rifugio, Rif05 and RifCov3-45 MDT is also required. The most pessimistic viewpoint is chosen, employing the largest error estimate available. Thus the diagonal of the original Rifugio covariance matrix that was used in the Rif05 model run is now employed as Rifugio MDT error (see table 4.6). The sum of both, the CLS09 error and the Rifugio error, is depicted in figure 4.28b.

First the smoothed Rifugio MDT shown in figure 4.27a is compared to CLS09 (see figures 4.29a and 4.29b). The Rifugio MDT differs from the CLS09 MDT to a much larger extent than the respective sum of errors allows. Apart from coastal regions, the largest differences are found in the Gulf Stream/ North Atlantic Current area. At some places in this area, the Rifugio MDT is up to several tens of centimeters lower than the CLS09 MDT. This is due to the MDT gradients along the ocean currents being much sharper in the Rifugio MDT where the CLS09 MDT shows a rather broad current (figure 4.27d). Presumably the sharper oceanographic features are caused by the small-scale geoid information of the GOCE data (CLS09 uses only GRACE data for the geoid). The differences between the two compared MDTs are much larger than

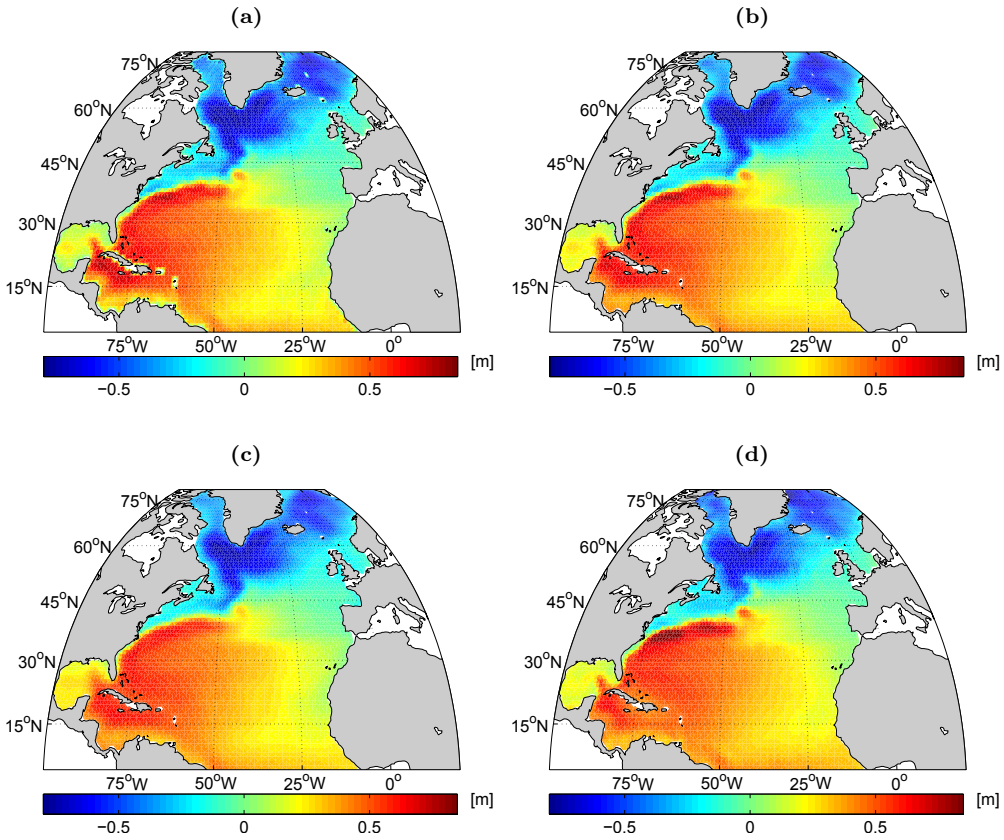

Fig. 4.27: MDTs for comparison: (a) Smoothed Rifugio MDT, (b) Rif05 MDT, (c) RifCov3-45 MDT, (d) CLS09 MDT.

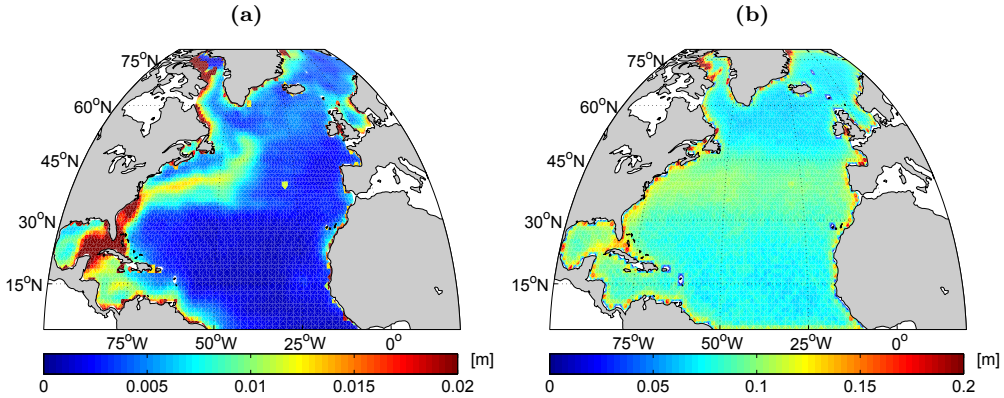

Fig. 4.28: (a) CLS09 MDT error, (b) sum of CLS09 MDT error and Rifugio MDT error.

the sum of errors shown in figure 4.28b. Figure 4.29b shows the value to which the absolute deviation of the two compared MDTs exceeds the error. The excess amounts

to 0.0563 m on average. This means that the actual deviation is about 5.63 cm higher than expected from the combined error estimate.

The same comparison is done with the Rif05 MDT and shown in figures 4.29c and 4.29d. Along most coastlines (Africa and America south of 30°N, Canada, Greenland, Islands in the GIN Seas), differences to the CLS09 MDT are decreased. This was expected as the satellite data cannot provide a good representation of the coastal areas due to leakage effects. In the open ocean, the biggest impact is observed at about 50°W-60°W, 37°N-40°N. In this region, the Rif05 MDT is closer to the CLS09 MDT than the Rifugio MDT. This means the ocean model IFEOM supplies MDT information similar to the CLS09 MDT. The excess of the difference of both MDTs above the sum of errors was decreased to 1.72 cm on average. In other areas of the open ocean, differences are only slightly smaller than in the above comparison with the Rifugio MDT. Deviations in the Gulf Stream/ North Atlantic Current area are still about 10 cm above the threshold given by the sum of both errors. Therefore the Rifugio and Rif05 MDT are not consistent with the CLS09 estimate within specified errors.

As explained at the beginning of this section, this comparison must be treated with caution. However, two features are striking in the difference plots: The deviations in the Gulf Stream and in the North Atlantic Current. In both regions, the CLS09 MDT is higher than our estimates. These areas are known for their strong activity of mesoscale (and submesoscale) eddies (e.g. Richardson, 1983; Ishikawa et al., 1997; Richardson, 1993). In-situ data from drifting buoys and Argo floats can partly capture these dynamics and therefore the CLS09 MDT which incorporates this type of data must differ from our estimates. The satellite-only Rifugio MDT is too large scale and the IFEOM model is too coarse for a proper representation of these physical processes.

Following the Gulf Stream in downstream direction, an abrupt increase in MDT height can be observed in the CLS09 data at approximately 70°W. Further eastwards, at around 60°W, the CLS09 MDT lowers again. Although this feature is also obvious in the Rifugio and Rif05 MDTs, it displays a much smaller across-stream extension. In contrast, this cannot be observed either in the RifCov3-45 solution (figure 4.27c) or in the preliminary GOCE MDT by Knudsen et al. (2011, not shown here). These MDTs are very homogenous following the Gulf Stream system from West to East. A possible explanation could be the different time spans which the compared MDTs are valid for. The CLS09 MDT describes the period from 1993-1999 (Rio et al., 2011), while all the Rifugio estimates use satellite data that were collected from 2001 onwards. However, this region of the ocean is determined by meandering of the Gulf Stream and its adjacent recirculations as well as shedding of eddies (references given above). Therefore, in any case this highly energetic system is difficult to represent in a steady-state model.

This becomes even more obvious in the comparison of the RifCov3-45 and the CLS09 MDT (figures 4.29e and 4.29f. In the RifCov3-45 solution, the North Atlantic Current is very smooth and the Mann Eddy very week. The largest difference however is visible in the Gulf Stream area. There are two contributions to this deviation: In the RifCov3-45 MDT, the across-stream gradient is less steep than in the CLS09 MDT and the whole current system is shifted slightly northwards. Both contributions might be a consequence of increased smoothness in this solution.

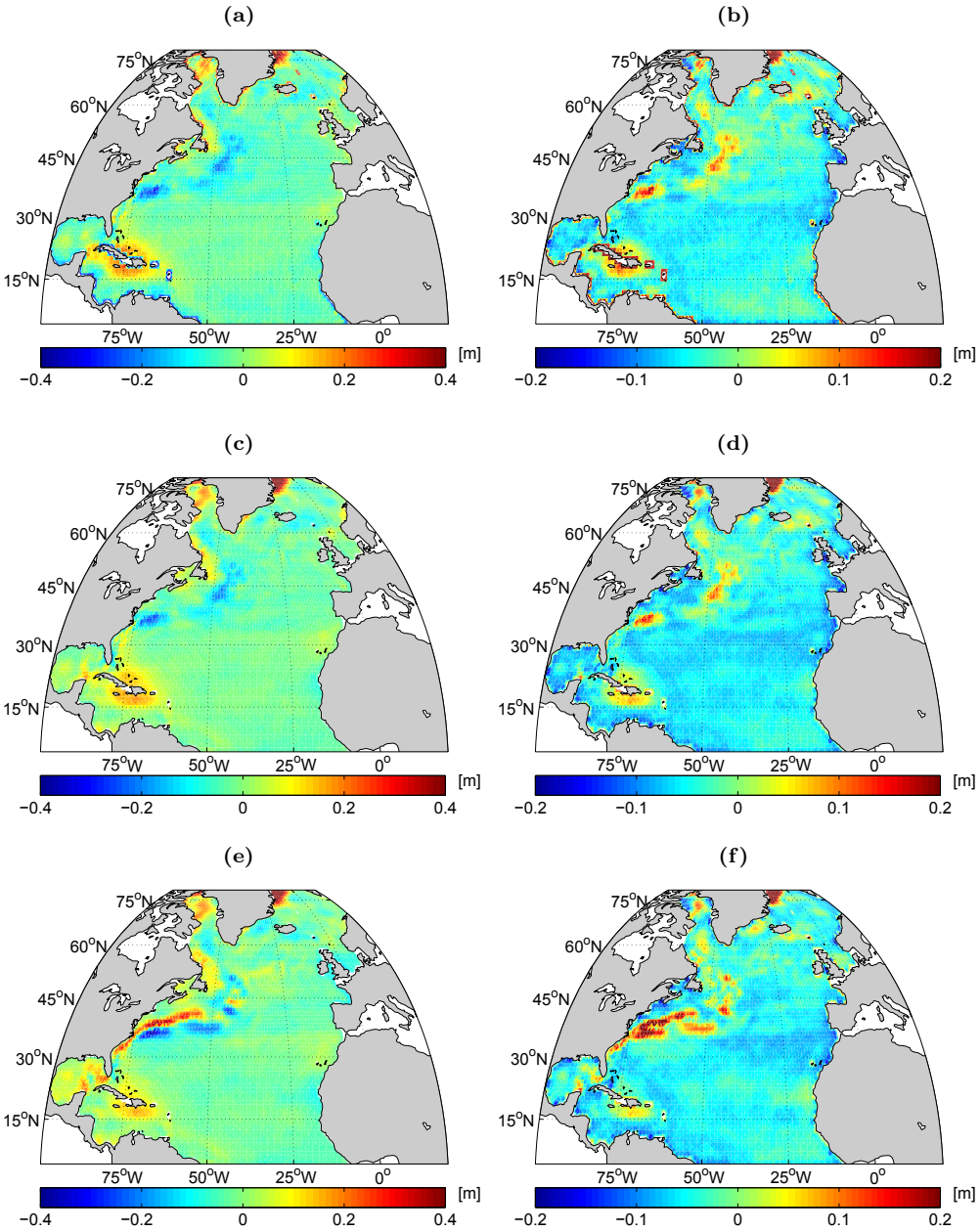

Fig. 4.29: Comparison of Rifugio, Rif05 and RifCov3-45 MDT with CLS09 MDT. The left panels show the differences to the CLS09 MDT, the right ones show the absolute difference minus the combined error estimate: (a) MDT difference: Rifugio - CLS09, (b) MDT: |Rifugio - CLS09| - error(CLS09+Rif05), (c) MDT difference: Rif05 - CLS09, (d) MDT: |Rif05 - CLS09| - error(CLS09+Rif05), (e) MDT difference: RifCov3-45 - CLS09, (f) MDT: |Rif05 - CLS09| - error(CLS09+Rif05).

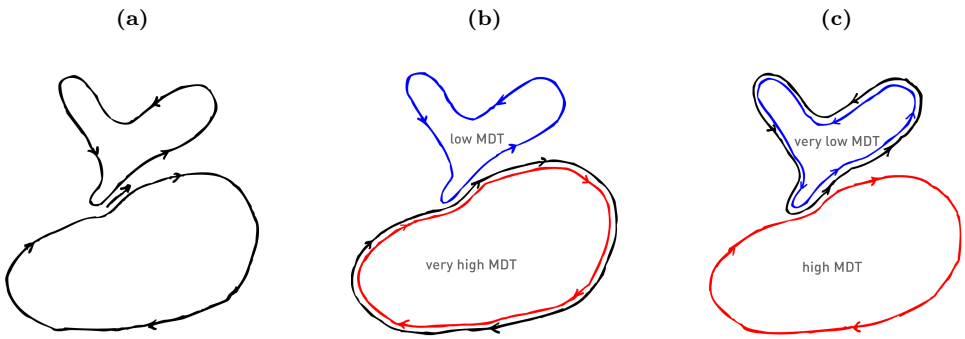

Fig. 4.30: Sketch demonstrating how (a) a strengthened North Atlantic Current may be the consequence of either (b) an increased Subtropical Gyre or (c) an increased Subpolar Gyre.

The Southern tip of the Labrador Current is well represented in the Rifugio, Rif05 and RifCov3-45 MDT (figure 4.27). It is significantly weaker in the CLS09 MDT (figure 4.27d) and also in the GOCE estimate by Knudsen et al. (2011, not shown here). Comparing the CLS09 MDT with its predecessor, the RIO05 MDT (Rio et al., 2011), illustrates that improved geoid data, optimized filtering and updated in-situ data increase velocities in the Labrador Current and in its southward extension. Our new MDT data sets continue this development. This finding is supported by Treguier et al. (2005), who derive southward velocities in the Labrador Current down to approximately 42°N both from WOCE drifter data and from four high-resolution ocean models.

The Rifugio MDT and the Rif05 MDT are lower than the CLS09 MDT both in the Gulf Stream and in the southern part of the Labrador Current (see above). This can be attributed to a comparatively weaker Subtropical Gyre and a comparatively stronger Subpolar Gyre, see sketch in figure 4.30. The MDT gradient along a virtual section across the Labrador Sea (Labrador - Greenland) is increased in the Rifugio, Rif05 and RifCov3-45 solutions compared to CLS09 as can be seen in figures 4.29a, 4.29c and 4.29e. This also supports the notion of an amplified Subpolar Gyre compared to the CLS09 MDT.

In the Rif05 result, the Labrador Current shows a barotropic transport of about 40 Sv which compares well with other models (39 Sv-45 Sv for the 1/6° Atlantic model (ATL6), Treguier et al., 2005) and also with observational estimates (40 Sv, Häkkinen and Rhines, 2004). The latter two authors describe a decline in Subpolar Gyre transport observed in the altimetry data during the 1990s. The CLS09 MDT is representative for this time period (Rio et al., 2011). In contrast, satellite data used in the Rifugio project were collected from 2001 onwards. Therefore the result might indicate that the trend in the satellite data observed by Häkkinen and Rhines (2004) has not continued to date and that the gyre strength has not been permanently altered. However, it is strongly recommended to verify this hypothesis with a high-resolution model more reliable than the coarse and stationary IFEOM.

4.3.4 Summary and conclusions: IFEOM

The three dimensional Inverse Finite Element Ocean Model IFEOM describes the stationary circulation in the North Atlantic ocean. The different model terms that are adjusted to each other within the cost function are already well balanced in the first guess computed by Richter (2010). The deviations of the model terms and the data terms are well within the a priori described errors. However, the first guess circulation displays several deficiencies that are described in section 4.1.4.

Step-by-step refinement of the model improves the circulation estimate considerably as does the assimilation of the new combined MDT data. The formal MDT error estimate however is too small to be utilized by the IFEOM model to its full extent of possible accuracy. Therefore it must be downweighted in the optimization process. In section 4.2.1 different approaches for extracting the most suitable amount of information from the data are presented.

When the new MDT data set is assimilated in an optimal way, it provides valuable information for the ocean model. More details of the ocean currents are revealed and increased velocities and temperature gradients appear that had been smoothed out in previous model runs by missing or less accurate data. The resulting MDT was compared to the CLS09 MDT of Rio et al. (2011) in section 4.3.3. Severe discrepancies were observed and investigated.

In section 4.3.2, the impact of the error covariances on the optimization was analysed. It was found that the covariances are of overall importance for smoothness and for the mean diagonal weight in the optimization. It was shown in section 4.3.2.3 that a decomposition of the covariance matrix and subsequent reinterpretation of the geodetic normal equations and the cost function is possible. The new cost function requires a recomputation of the weighting factor α. The resulting optimized model solution RifCov3-45 is the best IFEOM solution in terms of the oceanographic features presented in figure 4.23.

Figures 4.24 and 4.25 visualize that heat transports are improved considerably in the RifCov3-45 model result and agreement with other authors' estimates is enhanced. However, the strong influence of the weighting factor α is obvious.

Most improvements regarding the IFEOM model output were observed by refining the omission error model and by increasing the model resolution (sections 4.2.3 and 4.2.4). However, these steps still leave enough room for further model enhancement. Therefore the use of a more sophisticated ocean model is suggested to fully exploit the value of the new space-borne data in terms of precision and accuracy.

This is a sad situation.
But this is the state of the art.

Mojib Latif

Chapter 5

Discussion and Outlook

In this study, a new estimate for the Mean Dynamic Topography (MDT) and its error description was analysed in terms of its impact on ocean models. For the first time, a full error covariance matrix was available whose inverse could directly be used as weighting matrix in the ocean model optimization.

The response of two different steady-state inverse ocean models to the new MDT data was analysed. Both the 2D model FEMSECT and the 3D model IFEOM are finite element models, however for different regions of the world ocean. The output of each of these models in turn provided a combined satellite-ocean model MDT.

This study proved that the inverse ocean models benefit from the new MDT data set and its error covariance. It was shown that the resulting combined MDT is more realistic than the model MDT and the observational MDT by themselves. Oceanographic features such as the ocean current structure, the Meridional Overturning Circulation and heat transports were improved by the assimilated MDT data set. The MDT error covariance estimate is shown to be of highest importance for the optimization.

5.1 2D model FEMSECT

The steady-state ocean model FEMSECT was applied to the WOCE SR3 hydrographic section in the Southern Ocean between Tasmania and Antarctica. The two dimensional FEMSECT model was combined with two different MDT data sets: the CLS09 MDT (Rio et al., 2011) and a satellite-only MDT called "SAT". The CLS09 MDT is a combination of hydrographic, geodetic and altimetric data and serves for comparison purposes. The satellite-only MDT SAT is purely derived from satellite data and is complemented with basic MDT error estimates resulting from previous work. It was shown that the error model has a big impact on the result of the model optimization as was expected from earlier studies (Losch et al., 2002b; Losch and Schröter, 2004). Therefore further improvement of the MDT error model is essential for making further progress in analysing the MDT data by means of inverse ocean models. Approaches for advancing MDT error models are presented in combination with the ocean model IFEOM (next section).

The SAT MDT is very noisy and differs in scale from the resolution of the ocean model grid. The combination of the SAT MDT with the FEMSECT model results in relatively small transports of volume and heat across the section. This may be due to effects on the boundaries of the modelled section. The transports however increase when the MDT error model is refined. On the contrary, the CLS09 MDT induces very high across-section transports which decrease when the error model is improved. Unrealistically large transport estimates in the Southern Ocean induced by satellite MDT data are a well known problem (Griesel et al., 2012; Losch and Schröter, 2004). Until now it could not be explained whether this inconsistency of geodesy and oceanography in the Southern Ocean is due to a potential bias in the satellite observations or a shortcoming of our understanding of the Southern Ocean circulation. The author suggests that the issue of the large satellite induced transports could be connected with the MDT error model. The influence of the MDT error model on the ocean model result was shown to be remarkable. Refining the MDT error model changed the resulting transports estimates in the order of 10 Sv and 0.3 PW.

The FEMSECT model reproduces a reasonable structure of the mean velocity field in the WOCE SR3 section between Tasmania and Antarctica with all the major fronts and currents resolved. Nevertheless, the flow field strongly depends on the (arbitrarily chosen) errors for the zero bottom reference velocities. The sensitivity to prior errors of these reference velocities is a consequence of the model's simplifying assumptions and missing dynamics and can only be overcome introducing more complexity.

As discussed in this study, the mean bottom current structure at the WOCE SR3 section is not clear and causes controversy among oceanographers (compare Yaremchuk et al., 2001; Phillips and Rintoul, 2000; Losch and Schröter, 2004; Rintoul and Sokolov, 2001). This study shows that the FEMSECT model cannot provide an answer to that problem either. The modelled FEMSECT current structure is strongly dependent on the uncertain prior assumptions. From this study, it cannot be recommended to draw conclusions about ocean velocities from models depending on the (mostly unknown) reference velocities. The structure of the mean ocean bottom currents is clearly a topic for further research.

As a new approach, ocean surface velocities derived from ice drift and wind data are also used to improve the outcome of the FEMSECT model. The rather simple and heuristic ice drift model used in this study produced surprisingly good results. Due to the regional sea ice situation, this new velocity information was only available in the southernmost part of the model area. Nevertheless, the impact on the model results is remarkable. Transports of volume and heat across the section are reduced by an improved representation of the Antarctic countercurrent. Again, the accuracy of the given data is of crucial importance. The lack of an appropriate error description for the derived ocean surface velocities complicates their combination with models. To the author's knowledge, the valuable information of sea ice drift and wind data is currently not used in inverse ocean models of this type. The results presented in this study however suggest that this approach might be promising. Pursueing this idea requires a thorough evaluation of data availability and reliability as well as development of a thorough error model.

5.2 3D model IFEOM

The three dimensional Inverse Finite Element Ocean Model IFEOM was analysed with respect to its behaviour under assimilation of the new Rifugio MDT. The circulation of the first guess (the starting point of the model-data optimization) displayed several deficiencies. The optimized IFEOM model result benefited from the successively refined assimilation in this study.

For an overview, the series of IFEOM model results is again presented in table 5.1. The features mentioned in the first column are explained in detail in chapter 4 about IFEOM. The weighing matrices $\mathbb{P}_1$, $\mathbb{P}_2$, $\mathbb{P}_3$ and $\mathbb{P}_4$ were not explicitly mentioned before, but used here to mark the predecessors of the Rif05 weighting matrix $\mathbb{P}$. Being the most mature solutions, only the Rif05 solution and the RifCov3-45 solution were analysed further.

The new MDT data set provides valuable information for the ocean model. The combination of ocean model and MDT data reveals a more detailed structure of the ocean currents as well as increased velocities and increased temperature gradients. Transports of volume and heat are increased and agreement with other authors' estimates is advanced. The representation of the MOC is also improved. This demonstrates the good quality of the MDT data and its usefulness for improving the inverse ocean model IFEOM. Combining ocean models and MDT data is one way of improving our knowledge about the ocean circulation.

The resulting Rif05 MDT and the CLS09 MDT of Rio et al. (2011) were compared. Large differences were revealed and discussed. In this context, it turned out that the ocean model component contributes to an improved representation in the coastal areas. Satellite data in the vicinity of coastlines are contaminated by the influence of the land nearby. Estimated errors are large for satellite MDT close to coastlines, therefore the corresponding weights in the optimization are small. Hence the influence of the MDT data on the result of the optimization is small compared to the influence of the ocean model. In the open ocean, the resulting Rif05 MDT agrees better than the Rifugio MDT with the CLS09 MDT in the area of the Gulf Stream extension at approximately 50°W-60°W, 37°N-40°N due to the combination with IFEOM.

The solutions of the inverse model IFEOM depend to a large degree, if not primarily, on the error description of the assimilated data. The Rifugio error estimate is too small to be utilized by the IFEOM model to its full extent of possible accuracy. Therefore, a downweighting of the MDT data set was necessary and several methods were proposed and compared in this study.

The impact of the error covariances on the optimization was analysed in detail. It was found that the covariances are of overall importance as they do not only affect the smoothness of the data set, but also the diagonal weights. The data were downweighted in the optimization to compensate for too large diagonal weights. The IFEOM model was only influenced by these large diagonal weights and did not react to the mixed terms in the cost function created by the off-diagonal weights. This suggests that the ratio of variances and covariances in the variance-covariance matrix needs to be revised.

	Rif01	Rif02	Rif03	Rif04	Rif05	RifCov1	RifCov2	RifCov3
weighting factor $\alpha = 7$	✓	✓	✓	✓	✓	✓	✓	✓
refined omission error model	✗	✓	✓	✓	✓	✓	✓	✓
resolution $1° \times 1°$	✗	✗	✓	✓	✓	✓	✓	✓
2 months of GOCE data	✗	✗	✗	✓	✓	✓	✓	✓
7 months of GOCE data	✗	✗	✗	✗	✓	✓	✓	✓
weighting matrix	$\mathbb{P}_1$	$\mathbb{P}_2$	$\mathbb{P}_3$	$\mathbb{P}_4$	$\mathbb{P}$	$\frac{1}{\mathrm{diag}(\mathrm{COV})}$	$\mathrm{diag}(\mathbb{P})$	$\mathbb{D} = \mathbb{S}^{-T}\mathbb{P}\mathbb{S}^{-1}$

Table 5.1: Overview of IFEOM model solutions Rif01, Rif02, Rif03, Rif04, Rif05, RifCov1, RifCov2 and RifCov3.[1]

[1]For illustration, the weighting matrix of the RifCov1 solution is written in a non-mathematical way. This weighting matrix is obtained from inverting the variances (diagonal of the covariance matrix) after the off-diagonals of the covariance matrix have been set to zero.

The prior assumptions about the structure of the MDT error model have a large impact on the MDT error covariance and thus on the result of the ocean model. Information about the MDT data itself is reflected in the error description. Different interpretations of the Rifugio data-error structure were proposed and used within the optimization of the ocean model IFEOM. The resulting solution RifCov3-45 is the best IFEOM solution in terms of Meridional Overturning Circulation (MOC) and heat transports. In this model run, the smoothness information included in the covariance was not applied to the MDT error but to the MDT data themselves. This approach is unique and no references were found for a potential comparison. The author currently plans to conduct several toy experiments to further investigate the general validity, applicability and utility of this approach.

In order to fully exploit the value of the new space-borne data in terms of precision and accuracy, the use of a more sophisticated ocean model is suggested. Time-dependent models with finer resolution such as ECCO-GODAE (Evangelinos et al., 2006) should more likely be able to take advantage of the new wealth of information in the MDT data. Therefore, however, consistent information about the MDT and sea surface height anomalies is required. The author assumes that this is the right path, because this study showed that not all aspects of the ocean circulation can be accurately described by steady-state models.

5.3 Mean Dynamic Topography

Three MDT data sets were computed in this study: the smoothed satellite-only Rifugio MDT, the combined Rif05 MDT and the combined RifCov3-45 MDT (see figure 4.27). Both the Rif05 MDT and the RifCov3-45 MDT are a combination of the Rifugio MDT and the ocean model IFEOM. The Rifugio approach was first described in Becker et al. (2012).

One of the advantages of the Rifugio MDT is the availability of a full error covariance description (Becker et al., 2012). A full invertible error covariance matrix is required for a consistent assimilation into ocean models such as FEMSECT and IFEOM. In Becker et al. (2012), a full error covariance matrix for the MDT was computed for the first time. Nevertheless, as already mentioned above, the ratio of variances and covariances has to be revised when the inverse error covariance matrix is to be used in an inverse ocean model.

The Rifugio MDT was developed for the single purpose of ocean model assimilation (Becker et al., 2012). The unsmoothed Rifugio MDT is very noisy, see figure 4.18a. It has been shown that the error covariance matrix can be decomposed such that a smoothing operator is applied to the MDT before the assimilation. This approach is shown to be consistent with the geodetic normal equations and provides a smoothed Rifugio MDT. Removing the smoothness information from the inverse error covariance matrix and direct application to the MDT data has noticeable impact on the result of the optimization. The results of this study suggest to apply the available smoothness or filtering information to the data directly rather than to store it in the error covariance description. This is true for the purpose of weighted optimization, but also for understanding and presenting the structure of the data.

The resulting MDT data sets were compared to the CLS09 MDT (Rio et al., 2011). It was found that the new MDT data sets are not consistent with the CLS09 MDT within errorbars. Largest differences of more than 20 cm were observed in the Gulf Stream and in the southern tip of the Labrador Current. In the Rifugio MDT and in the Rif05 MDT, the gradients are sharper than in the CLS09 MDT. This is presumably due to the GOCE data used in these data sets. The MDTs estimated in this study show a stronger Subpolar Gyre than the CLS09 MDT.

A decline of the Subpolar Gyre was described by Häkkinen and Rhines (2004) for the decade preceeding the satellite observations used in this work. As the Subpolar Gyre is comparatively strong in the Rifugio and Rif05 MDT, this trend is not confirmed by this study.

If I were dropped out of a plane into the ocean and told the nearest land was a thousand miles away, I'd still swim.

Abraham Maslow

5.4 Conclusions

Both the ocean models FEMSECT and IFEOM benefit from the new satellite MDT estimates. In return, also the satellite MDT estimates are improved by the ocean models. The resulting combined MDT data sets are shown to be superior to the first guess model MDT as well as to the satellite MDTs in terms of selected oceanographic features. Improvements, however, remain below those expected from the high precision and accuracy of the new satellite gravity field data (e.g. Rummel and Gruber, 2010).

The availability of a full error covariance matrix is of unprecedented benefit for the ocean model optimization. The ocean model optimization strongly depends on the estimate of the inverse MDT error covariance matrix that is used as weighting matrix in the optimization. This estimate, however, is only to a certain extent determined by observations and modelling assumptions about the error covariance structure must be introduced. First steps in this direction were undertaken by Becker (2009, pers. comm.) and the effect was analysed in this study. However, further research on the MDT error covariance structure and its statistical properties is required to exploit the satellite MDT information in an optimal way within the assimilation procedure. The author believes that this is one of the first issues that have to be addressed for making further progress.

Although a complete MDT error estimate was available, it could not be used in the ocean model optimization without the introduction of an additional weighting factor. The author suggests that this is due to an inaccurate ratio of variances and covariances in the variance-covariance matrix. Different strategies for the determination of the weighting factor are proposed in this study, and the minimum penalty variance (MPV) approach was shown to be the most successful for the ocean model IFEOM. Further research has to reveal whether the MPV approach is an appropriate method in general for inverse data assimilation problems.

A new way of interpreting the error covariance information was proposed in this

study, and the resulting model solution, RifCov3-45, is promising. It still has to be investigated whether this approach is appropriate in general or only in this specific isolated case. This topic is directly linked with the weighting process within the optimization. Clarification of this complex issue will generally improve the combination of models and observations, not only in ocean modelling. Further interdisciplinary research will be an advantage and come to the fore in the future.

When presence of sea ice impedes altimetric measurements, obtaining ocean surface velocities by sea ice drift assimilation represents a possible alternative. Apart from the sea-ice drift data used in this study (Fowler, 2003), a more accurate approach for estimating sea-ice motion from SAR (Synthetic Aperture Radar) images has been developed recently (Hollands and Dierking, 2011). For studies in high latitudes, a combination of these approaches will be beneficial and thus should be promoted.

As MDT calculation profits greatly by new geoid data from the satellites GRACE and GOCE, there is high interest in new gravity field missions in Germany (Müller et al., 2009). Possibilities for an increase of precision and accuracy are listed by Rummel (2003). These include e.g. performance of the sensor system, satellite altitude and the design of complementary space missions for the separation of individual contributions and for comprehensive modelling.

However, more accurate data alone is not sufficient to improve the results of inverse models as was shown also in this work. The long lists of publications that arose from the GRACE and GOCE missions (`http://www.csr.utexas.edu/grace/publications/citation.html` and `http://www.goce-projektbuero.de/7777--~goce~Projektbuero~papers~Literaturverzeichnis.html`) demonstrate that benefit can be drawn from improved data sets only in combination with further improvement of processing and interpretation methods. This is confirmed in this study, as the results suggest that much valuable information is contained in the satellite MDT data and its error description. However, the evaluation of the new data still needs to be advanced. In this study, the choice of the weighting factors in the optimization, the smoothing introduced with the RifCov3-45 approach and the statistical models for MDT error estimation were investigated. In this way, the Rifugio approach aims at making a small contribution to a consistent evaluation of the new data.

As the variety and amount of different data sets and the diversity of available ocean models increase, another point will become more important: Data and model need to match. It was shown in the case of the FEMSECT model that resolution of model and data have to agree. In the IFEOM model, the data had to be downweighted because the model could not incorporate data of this relatively high accuracy. Therefore, to the same extent as satellites are engineered, measuring techniques are developed and the processing of data is improved, also ocean models have to mature. As an example, the dependency of the FEMSECT model on prescribed (though mostly unknown) bottom velocities was mentioned. Both ocean models used in this study, FEMSECT and IFEOM, are steady-state models. This is a strong limitation for the description of ocean dynamics. Therefore, time-dependent estimation should be preferred as it is done e.g. by Janjić et al. (2012), however with a different approach and focus. Several other issues to be investigated and improved in the future include resolution both in time and space, resolving versus parametrizing physical processes, boundary conditions and coupling to different Earth system components.

Appendix G

Geodesy

G.1 Spherical harmonics

The gravity field outside the solid Earth can be represented as a solution of Laplace's differential equation $\Delta V = 0$ for the gravity potential V.

For a convenient representation of the solution, Legendre functions are introduced (National Research Council, 1998):

$$P_{\ell m}(x) = \frac{(1-x^2)^{\frac{m}{2}}}{2^\ell \ell!} \frac{d^{\ell+m}}{dx^{\ell+m}}(x^2-1)^\ell, \quad 0 \le m \le \ell. \tag{G.1}$$

The Legendre functions are normalized by constants

$$A_{\ell 0} = \frac{1}{2\ell+1} \text{ and } A_{\ell m} = \frac{1}{2(2\ell+1)} \frac{(\ell+m)!}{(\ell-m)!} : \quad \bar{P}_{\ell m} = A_{\ell m}^{-\frac{1}{2}} P_{\ell m}.$$

The geodetically normalized surface spherical harmonics of degree l and order m can now be defined as

$$\{Y^c_{\ell m}, Y^s_{\ell m}\}_{\ell,m} = \left\{\bar{P}_{\ell m}(\cos(\theta))\cos(m\phi), \bar{P}_{\ell m}(\cos(\theta))\sin(m\phi)\right\}_{\ell,m} \quad 0 \le m \le \ell. \tag{G.2}$$

This set of functions $\{Y^c_{\ell m}, Y^s_{\ell m}\}_{\ell,m}$ is orthonormal and complete on the surface of a sphere.

For order $m = 0$, the spherical harmonics $Y^c_{\ell m}$ are independent of longitude ϕ and therefore they are named zonal spherical harmonics. In $0 \le \theta \le \pi$, there are ℓ zero crossings. For $m \neq 0$, the number of zero crossings in $0 < \theta < \pi$ is reduced to $\ell - m$. These spherical harmonic functions are dependent of longitude ϕ via $\sin(m\phi)$ and $\cos(m\phi)$ and are called tesseral spherical harmonics. For $m = \ell$, the dependency on θ vanishes and sectoral spherical harmonics are obtained. See e.g. Torge (2003) for illustration of the geometry.

G.2 Kaulas rule of thumb

William M. Kaula developed an empirical formula for the decrease of the spherical harmonic coefficients with increasing degree (Kaula, 1966). The degree variances for degree ℓ given by

$$\sigma_\ell^2 = 10^{-10}\frac{2\ell+1}{\ell^4} \tag{G.3}$$

describe the signal content per degree of the gravity potential (of the $2\ell+1$ spherical harmonic coefficients for degree ℓ). Therefore the standard deviation for a coefficient m of degree ℓ follows as:

$$\sigma_{\ell m} = \sqrt{\frac{\sigma_\ell^2}{2\ell+1}} = \sqrt{\frac{10^{-10}}{\ell^4}} = \frac{10^{-5}}{\ell^2.} \tag{G.4}$$

Appendix N

Numerics

N.1 Optimization algorithm

The Broyden-Fletcher-Goldfarb-Shanno (BFGS) method (basics to be found e.g. in Broyden, 1970) one of the most famous and most efficient quasi-Newton algorithms for solving nonlinear unconstrained optimization problems (Dai, 2002). A stationary point of a function where the gradient is zero is sought. The method assumes that the function can be locally approximated as a quadratic function in the region around the optimum, and uses the first and second derivatives to find the stationary point. The Hessian matrix of second derivatives of the function to be minimized does not need to be computed. The Hessian is updated by analysing successive gradient vectors instead.

When $f(\mathbf{x})$ denotes the objective function to be minimized, the following steps are repeated from $k = 0$, an initial guess $\mathbf{x}_0$ and an approximate Hessian matrix $\mathbb{B}_0$ (Nocedal and Wright, 2006):

- Obtain a direction $\mathbf{p}_k$ by solving: $\mathbb{B}_k \mathbf{p}_k = -\nabla f(\mathbf{x}_k)$.
- Perform a line search to find an acceptable stepsize α_k in the direction $\mathbf{p}_k$, then update $\mathbf{x}_{k+1} = \mathbf{x}_k + \alpha_k \mathbf{p}_k$.
- Set $\Delta\mathbf{x}_k = \alpha_k \mathbf{p}_k$ and $\Delta\mathbf{g}_k = \nabla f(\mathbf{x}_{k+1}) - \nabla f(\mathbf{x}_k)$.
- Update the approximate Hessian $\mathbb{B}_{k+1} = \mathbb{B}_k + \frac{\Delta\mathbf{g}_k \Delta\mathbf{g}_k^{\mathrm{T}}}{\Delta\mathbf{g}_k^{\mathrm{T}} \Delta\mathbf{x}_k} - \frac{\mathbb{B}_k \Delta\mathbf{x}_k \Delta\mathbf{x}_k^{\mathrm{T}} \mathbb{B}_k}{\Delta\mathbf{x}_k^{\mathrm{T}} \mathbb{B}_k \Delta\mathbf{x}_k}$.

The BFGS update is reasonably robust when the line searches are sloppy, however, the algorithm usually does not converge for nonquadratic problems (Chong and Żak, 2001).

N.2 Moore-Penrose pseudoinverse

The pseudoinverse $\mathbb{A}^+$ of a matrix $\mathbb{A}$ is a generalization of the inverse matrix and is used in several computational situations when an inverse is required but not existing (see e.g. Golub and Van Loan, 1996). The pseudoinverse is defined and unique for all matrices whose entries are real or complex numbers. The Moore-Penrose pseudoinverse was first described by E.H. Moore, A. Bjerhammar and R. Penrose and is defined by the following properties:

- $\mathbb{A}\mathbb{A}^+\mathbb{A} = \mathbb{A}$
- $\mathbb{A}^+\mathbb{A}\mathbb{A}^+ = \mathbb{A}^+$
- $(\mathbb{A}\mathbb{A}^+)^* = \mathbb{A}\mathbb{A}^+$ and
- $(\mathbb{A}^+\mathbb{A})^* = \mathbb{A}^+\mathbb{A}$, where $\mathbb{A}^*$ denotes the conjugate transpose of $\mathbb{A}$.

The Moore-Penrose pseudoinverse can be computed using the singular value decomposition (SVD): If $\mathbb{A} = \mathbb{U}\mathbf{\Sigma}\mathbb{V}^*$ is the singular value decomposition of $\mathbb{A}$, then $\mathbb{A}^+ = \mathbb{V}\mathbf{\Sigma}^+\mathbb{U}^*$. For calculating the pseudoinverse $\mathbf{\Sigma}^+$ of the diagonal matrix $\mathbf{\Sigma}$, the reciprocal of each non-zero element on the diagonal is taken, leaving the zeros unchanged, and transposing the resulting matrix. In numerical computation, only singular values larger than some small tolerance are taken to be nonzero, and the others are replaced by zeros.

N.3 Formal error computation

When a quadratic cost function is used for optimization of the model (as in FEMSECT or IFEOM), the matrix of second derivatives of this quadratic function, the Hessian matrix, is of particular importance. It can be interpreted as the inverse of the error covariance matrix of the control parameters (Thacker, 1989). For any linear function v of the control parameters x:

$$v = \mathbb{L}^T x,$$

the error covariance of v can be obtained from the Hessian matrix $\mathbb{H}$ as:

$$\mathrm{cov}(v) = \mathbb{L}^T \mathbb{H}^{-1} \mathbb{L}.$$

In the FEMSECT model, this method is used for the computation of linearized posterior volume and heat transport errors. In the IFEOM model, the computation of the Hessian is not implemented yet, let alone its inversion.

List of figures

List of tables

References

Achen, C., 1982. Interpreting and Using Regression. Sage, Beverly Hills.

Albertella, A., Rummel, R., 2009. On the spectral consistency of the altimetric ocean and geoid surface: a one-dimensional example. Journal of Geodesy 83 (9), 805–815, DOI 10.1007/s00190-008-0299-5.

Albertella, A., Savcenko, R., Bosch, W., Rummel, R., 2008. Dynamic Ocean Topography - The Geodetic Approach. Tech. rep., Institut für Astronomische und Physikalische Geodäsie (IAPG), Deutsches Geodätisches Forschungsinstitut (DGFI), TU München, DGFI Report No. 82 / IAPG FESG Report No. 27.

Andersen, O., Knudsen, P., 2009. DNSC08 mean sea surface and mean dynamic topography models. Journal of Geophysical Research 114 (C11001), doi:10.1029/2008JC005179.

Anderson, D., Sheinbaum, J., Haines, K., 1996. Data assimilation in ocean models. Reports on Progress in Physics 59, 1209–1266, `http://iopscience.iop.org/0034-4885/59/10/001` (6 August 2012).

Bacon, S., 1997. Circulation and Fluxes in the North Atlantic between Greenland and Ireland. Journal of Physical Oceanography 27, 1420–1435.

Barker, D., Diana, L., 1974. Simple method for fitting data when both variables have uncertainties. American Journal of Physics 42, 224–227.

Becker, S., Freiwald, G., Losch, M., Schuh, W.-D., 2012. Rigorous Fusion of Gravity Field into Stationary Ocean Models. Journal of Geodynamics 59–60, 99–110, doi:10.1016/j.jog.2011.07.006.

Bennett, A., 2002. Inverse Modeling of the Ocean and Atmosphere. Cambridge University Press.

Bingham, R., Haines, K., Hughes, C., 2008. Calculating the Ocean's Mean Dynamic Topography from a Mean Sea Surface and a Geoid. Journal of Atmospheric and Oceanic Technology 25, doi:10.1175/2008JTECHO568.1.

Bingham, R., Knudsen, P., Andersen, O., Pail, R., 2011. An initial estimate of the North Atlantic steady-state geostrophic circulation from GOCE. Geophysical Research Letters 38 (L01606), doi:10.1029/2010GL045633.

Birol, F., Brankart, J., Lemoine, J., Brasseur, P., Verron, J., 2005. Assimilation of satellite altimetry referenced to the new GRACE geoid estimate. Geophysical Research Letters 32 (L06601), doi:10.1029/2004GL021329.

Bosch, W., Savcenko, R., 2009. Absolute dynamic ocean topography profiles. OST Science Team Meeting 22-24 June 2009, Seattle, Poster.

Bosch, W., Savcenko, R., 2010. On Estimating the Dynamic Ocean Topography – A Profile Approach. In: Mertikas, S., Sideris, M. (Eds.), Gravity, Geoid and Earth Observation. Vol. 135 of International Association of Geodesy Symposia. Springer Berlin Heidelberg, pp. 263–269, doi: 10.1007/978-3-642-10634-7_34.

Broecker, W., 1991. The great ocean conveyor. Oceanography 4, 79–89.

Broyden, C., 1970. The Convergence of a Class of Double-rank Minimization Algorithms 1. General Considerations. IMA Journal of Applied Mathematics 6, 76–90.

Bruinsma, S., Lemoine, J., Biancale, R., Valès, N., 2010. CNES/GRGS 10–day gravity field models (release 2) and their evaluation. Advances in Space Research 45, 587–601, doi:10.1016/j.asr.2009.10.012.

Bruzzone, H., Moreno, C., 1998. When errors in both coordinates make a difference in the fitting of straight lines by least squares. Measurement Science and Technology 9, 2007–2011.

Bryden, H., Imawaki, S., 2001. Ocean Heat Transport. In: Siedler, G., Church, J., Gould, J. (Eds.), Ocean Circulation and Climate: Observing and Modelling the Global Ocean. Vol. 77 of International Geophysics Series. Academic Press, pp. 455–474.

Bryden, H., Longworth, H., Cunningham, S., 2005. Slowing of The Atlantic Meridional Overturning Circulation at 25°N. Nature 438, 655–657.

Caldeira, K., Duffy, P., 2000. The Role of the Southern Ocean in Uptake and Storage of Anthropogenic Carbon Dioxide. Science 287, 620–622.

Castruccio, F., Verron, J., Gourdeau, L., Brankart, J.-M., Brasseur, P., 2008. Joint altimetric and in-situ data assimilation using the GRACE mean dynamic topography: a 1993–1998 hindcast experiment in the Tropical Pacific Ocean. Ocean Dynamics 58, 43–63, DOI: 10.1007/s10236-007-0131-4.

Chassignet, E., Verron, J. (Eds.), 1998. Ocean Modeling and Parameterization. Vol. 516 of NATO Science Series C: Mathematical and Physical Sciences. Kluwer Academic Publishers.

Chong, E., Żak, S., 2001. An Introduction to Optimization, 2nd Edition. Interscience Series in Discrete Mathematics and Optimization. Wiley.

Cunningham, S., Kanzow, T., Rayner, D., Baringer, M., Johns, W., Marotzke, J. Longworth, H., Grant, E., Hirschi, J.-M., Beal, L., Meinen, C., Bryden, H., 2007. Temporal Variability of the Atlantic Meridional Overturning Circulation at 26.5°N. Science 317, 935–938.

Dai, Y.-H., 2002. Convergence properties of the BFGS algorithm. SIAM Journal on Optimization 13 (3), 693–701.

Danilov, S., Kivman, G., Schröter, J., 2004. A finite-element ocean model: principles and evaluation. Ocean Modelling 6, 125–150.

Danilov, S., Kivman, G., Schröter, J., 2005. Evaluatin of an eddy-permitting finite-element ocean model in the North Atlantic. Ocean Modelling 10, 35–49.

de Brauwere, A., De Ridder, F., Elskens, M., Schoukens, J., Pintelon, R., Baeyens, W., 2005. Refined parameter and uncertainty estimation when both variables are subject to error. Case study: estimation of Si consumption and regeneration rates in a marine environment. Journal of Marine Systems 55, 205–221.

de Freitas Assad, L., Torres Junior, A., Zumpichiatti Arruda, W., da Silveira Mascarenhas Junior, A., Landau, L., 2009. Volume and heat transports in the world oceans from an ocean general circulation model. Revista Brasileira de Geofísica 27, 181–194.

Dijkstra, H., 2008. Dynamical Oceanography. Springer.

Disatnik, D., Benninga, S., 2007. Shrinking the Covariance Matrix–Simpler is Better. Journal of Portfolio Management 33 (4), 56–63.

Draper, N., Smith, H., 1981. Applied Regression Analysis. John Wiley & Sons.

Egbert, G., Erofeeva, S., 2002. Efficient Inverse Modelling of Barotropic Ocean Tides. J. Atmos. Oceanic Technol. 19, 183–204, doi: 10.1175/1520-0426(2002)019<0183:EIMOBO>2.0.CO;2.

Emery, W., Thomson, R., 2001. Data Analysis Methods in Physical Oceanography. Elevier.

Evangelinos, C., Forget, G., Heimbach, P., Mazloff, M., Wunsch, C., Ponte, R., Vinogradov, S., 2006. ECCOc: The ECCO-GODAE Ocean State Estimation Effort at MIT/AER. Presentation at the CLIVAR/GSOP workshop, ECMWF, August 2006, `http://www.docstoc.com/docs/28391408/ECCOc-The-ECCO-GODAE-Ocean-State-Estimation-Effort-at-MITAER` (6 August 2012).

Evensen, G., 1994. Inverse methods and data assimilation in nonlinear ocean models. Physica D 77, 108–129.

Farrell, S., McAdoo, D., Laxon, S., Zwally, H., Yi, D., Ridout, A., Giles, K., 2012. Mean dynamic topography of the Arctic Ocean. Geophysical Research Letters 39 (L01601), doi:10.1029/2011GL050052.

Fowler, C., 2003. Polar Pathfinder Daily 25 km EASE-Grid Sea Ice Motion Vectors. Digital media, updated 2007. Boulder, Colorado USA: National Snow and Ice Data Center.

Friedrichs, M., Hall, M., 1993. Deep circulation in the tropical North Atlantic. Journal of Marine Research 51 (4), 697–736.

Ganachaud, A., Wunsch, C., 2000. Improved estimates of global ocean circulation, heat transport and mixing from hydrographic data. Nature 408, 453–457.

Ganachaud, A., Wunsch, C., 2003. Large-Scale Ocean Heat and Freshwater Transports during the World Ocean Circulation Experiment. Journal of Climate 16, 696–705.

GeoForschungsZentrum, 2006. THE GRACE SATELLITE TANDEM: High-Precision Earth Monitoring for a Better Understanding of Climate. `www.csr.utexas.edu/grace/publications/flyer/GRACEflyer0612a.pdf` (6 August 2012), GFZ Potsdam.

Georgi, S., Toole, J., 1982. The Antarctic Circumpolar Current and the oceanic heat and freshwater budgets. Journal of Marine Research 40, 183–197.

Gilbert, J.-C., Lemarécha, C., 1995. The Modules M1QN3 and N1QN3. Tech. rep., INRIA.

Gleick, P. H., 1996. Water resources. In: Schneider, S. (Ed.), Encyclopedia of Climate and Weather. Vol. 2. Oxford University Press, pp. 817–823.

Golub, G., Van Loan, C., 1996. Matrix computations. The Johns Hopkins University Press.

Gouretski, V., Koltermann, K., 2004. WOCE Global Hydrographic Climatology. Tech. rep., Bundesamt für Seeschifffahrt und Hydrographie Hamburg und Rostock, Germany.

Greybush, S., Kalnay, E., Miyoshi, T., Ide, K., Hunt, B., 2011. Balance and Ensemble Kalman Filter Localization Techniques. Monthly Weather Review 139, 511–522, doi: 10.1175/2010MWR3328.1.

Griesel, A., Gille, S., Mazloff, M., Cornuelle, B., 2010. Using Dynamic Ocean Topography To Probe Southern Ocean Circulation. Poster presentation at EGU 2010, Scripps Institution of Oceanography, University of California.

Griesel, A., Mazloff, M., Gille, S., 2012. Mean Dynamic Topography in the Southern Ocean: Evaluating Antarctic Circumpolar Current Transport. Journal of Geophysical Research 117 (C01020), doi:10.1029/2011JC007573.

Griffies, S., Biastoch, A., Böning, C., Bryan, F., Danabasoglu, G., Chassignet, E., England, M., Gerdes, R., Haak, H., Hallberg, R., Hazeleger, W., Jungclaus, J., Large, W., Madec, G., Pirani, A., B.L., S., Scheinert, M., Gupta, A., Severijns, C., Simmons, H., Treguier, A., Winton, M., Yeager, S., Yin, J., 2009. Coordinated Ocean-ice Reference Experiments (COREs). Ocean Modelling 26, 1–46.

Haines, K., Johannessen, J., Knudsen, P., Lea, D., Rio, M.-H., Bertino, L., Davidson, F., Hernandez, F., 2011. An ocean modelling and assimilation guide to using GOCE geoid products. Ocean Science 7, 151–164, doi:10.5194/os-7-151-2011.

Häkkinen, S., Rhines, P., 2004. Decline of Subpolar North Atlantic Circulation During the 1990s. Science 304, 555–559, DOI: 10.1126/science.1094917.

Hall, M., Bryden, H., 1982. Direct estimates and mechanisms of ocean heat transport. Deep-Sea Research 29 (3A), 339–359.

Hamill, T., Whitaker, J., Snyder, C., 2001. Distance-Dependent Filtering of Background Error Covariance Estimates in an Ensemble Kalman Filter. Monthly Weather Review 129, 2776–2790, doi: 10.1175/1520-0493(2001)129<2776:DDFOBE>2.0.CO;2.

Hanke, M., 1996. Limitations of the L-curve method in ill-posed problems. BIT Numerical Mathematics 36 (2), 287–301.

Hansen, B., Østerhus, S., 2000. North Atlantic - Nordic Seas exchanges. Progress in Oceanography 45, 109–208.

Hansen, P., 2005. The L-curve and its use in the numerical treatment of inverse problems. online at `http://www.sintef.no/project/eVITAmeeting/2005/Lcurve.pdf` (6 August 2012), suggested reading for Fifth Winter School in Computational Mathematics, Geilo, February 20-25, 2005.

Hansen, P., O'Leary, D., 1993. The use of the L-curve in the regularization of discrete ill-posed problems. SIAM Journal on Scientific Computing 14 (6), 1487–1503.

Hernandez, F., et al., 2001. Surface Moyenne Oceanique: Support Scientifique à la mission altimétrique Jason-1, et à une mission micro-satellite altimétrique. Contrat SSALTO 2945 - Lot2 - A.1. Rapp. final cls/dosnt/00.341, CLS, Ramonville, France.

Hogg, N., Pickart, R., Hendry, R., Smethie, Jr, W., 1986. The Northern Recirculation Gyre of the Gulf Stream. Deep-Sea Research 33 (9), 1139–1165.

Hollands, T., Dierking, W., 2011. Performance of a multiscale correlation algorithm for the estimation of sea ice drift from sar images: initial results. Annals of Glaciology 52 (57), 311–317, official URL: `http://www.igsoc.org/annals/v52/57/x57A037.pdf`.

Hopkins, T., 1991. The GIN Sea - A synthesis of its physical oceanography and literature review 1972-1985. Earth-Science Reviews 30, 175–318.

Hu, A., Meehl, G., Otte-Bliesner, B., Waelbroeck, C., Han, W., Loutre, M.-F., Lambeck, K., Mitrovica, J., Rosenbloom, N., 2010. Influence of Bering Strait flow and North Atlantic circulation on glacial sea-level changes. nature geoscience 3, 118–121, doi: 10.1038/NGEO729.

Hughes, C., Bingham, R., 2008. An Oceanographer's Guide to GOCE and the Geoid. Ocean Science, 15–29.

Hwang, C., 1991. Orthogonal Functions Over the Oceans and Applications to the Determination of Orbit Error, Geoid and Sea Surface Topography from Satellite Altimetry. Report 414, Department of Geodetic Science and Surveying, The Ohio State University.

Ilk, K., Flury, J., Rummel, R., Schwintzer, P., Bosch, W., Haas, C., Schröter, J., Stammer, D., Zahel, W., Miller, H., Dietrich, R., Huybrechts, P., Schmeling, H., Wolf, D., Götze, H., Riegger, J., Bardossy, A., Güntner, A., Gruber, T., 2005. Mass Transport and Mass Distribution in the Earth System. Proposal for a German Priority Research Program, Institut für Theoretische Geodäsie, Bonn; Institut für Astronomische und Physikalische Geodäsie, München; GeoForschungsZentrum, Potsdam; Deutsches Geodätisches Forschungsinstitut, München; Alfred Wegener Institut für Polar- und Meeresforschung, Bremerhaven; Institut für Meereskunde, Hamburg; Institut für Planetare Geodäsie, Dresden; Institut für Meteorologie und Geophysik, Frankfurt am Main; Institut für Geowissenschaften, Kiel; Institut für Wasserbau, Stuttgart, GOCE-Projektbüro Deutschland.

Irvine, P., Sriver, R., Keller, K., 2012. Tension between reducing sea-level rise and global warming through solar-radiation management. nature climate change. Published online, DOI:10.1038/NCLIMATE1351.

Ishikawa, Y., Awaji, T., Akitomo, K., 1997. Global Surface Circulation and Its Kinetic Energy Distribution Derived from Drifting Buoys. Journal of Oceanography 53, 489–516.

Janjić, T., Schröter, J., Albertella, A., Bosch, W., Rummel, R., Savcenko, R., Schwabe, J., Scheinert, M., 2011. Assimilation of geodetic dynamic ocean topography using ensemble based Kalman filter. Journal of Geodynamics. In press, doi:10.1016/j.jog.2011.07.001.

Janjić, T., Schröter, J., Savcenko, R., Bosch, W., Albertella, A., Rummel, R. ., Klatt, O., 2012. Impact of combining GRACE and GOCE gravity data on ocean circulation estimates. Ocean Science 8, 65–79, doi:10.5194/os-8-65-2012.

Jayne, S., 2006. Circulation of the North Atlantic Ocean from altimetry and the Gravity Recovery and Climate Experiment geoid. Journal of Geophysical Research 111 (C03005), doi:10.1029/2005JC003128.

Jekeli, C., 1981. Alternative methods to smooth the Earth's gravity field. Reports of the Department of Geodetic Science 327, Ohio State University (OSU).

Johannessen, J., Balmino, G., Le Provost, C., Rummel, R., Sabadini, R., Sünkel, H., Tscherning, C., Visser, P., Woodworth, P., Hughes, C., LeGrand, P., Sneeuw, N., Perosanz, F., Aguirre-Martinez, M., Rebhan, H., Drinkwater, M., 2003. The European Gravity Field and Steady-State Ocean Circulation Explorer Satellite Mission: Impact in Geophysics. Survey in Geophysics 24, 339–386.

Johns, W., Shay, T., Bane, J., Watts, D., 1995. Gulf Stream structure, transport, and recirculation near 68°W. Journal of Geophysical Research 100, 817–838.

Johnson, G., 2008. Quantifying Antarctic Bottom Water and North Atlantic Deep Water volumes. Journal of Geophysical Research 113 (C05027), doi:10.1029/2007JC004477.

Kaula, W., 1966. Theory of Satellite Geodesy. Blaisdell Publ. Comp., Massachusetts-Toronto-London.

Kelley, C., 1999. Iterative Methods for Optimization. Vol. 18 of Frontiers in Applied Mathematics. Society for Industrial Mathematics.

Kern, M., Schwarz, K., Sneeuw, N., 2003. A study on the combination of satellite, airborne, and terrestrial gravity data. Journal of Geodesy 77 (3–4), 217–225.

Kimura, N., 2004. Sea Ice Motion in Response to Surface Wind and Ocean Current in the Southern Ocean. Journal of the Meteorological Society of Japan 82, 1223–1231.

Kimura, N., Wakatsuchi, M., 2000. Relationship between sea-ice motion and geostrophic wind in the Northern Hemisphere. Geophysical Research Letters 27 (22), 3735–3738.

Kivman, G., Kurapov, A., Guessen, A., 2001. An Entropy Approach to Tuning Weights and Smoothing in the Generalized Inversion. Journal of Atmospheric and Oceanic Technology 18, 266–276.

Klein, B., Molinari, R., Müller, T., Siedler, G., 1995. A transatlantic section at 14.5N: Meridional volume and heat fluxes. Journal of Marine Research 53, 929–957.

Knudsen, P., 2010. GOCINO: GOCE in Ocean Modelling. Final Activity Report, DTU Space, Contract No SSA5-CT-2006-030756, Specific Support Action.

Knudsen, P., Bingham, R., Anderson, O., Rio, M.-H., 2011. A global mean dynamic topography and ocean circulation estimation using a preliminary GOCE gravity field model. Journal of Geodesy. Published online, DOI 10.1007/s00190-011-0485-8.

Köhl, A., Stammer, D., 2008. Variability of the Meridional Overturning in the North Atlantic from the 50-Year GECCO State Estimate. Journal of Physical Oceanography 38, 1913–1930.

Koltermann, K., Sokov, A., Tereschenkov, V., Dobroliubov, S., Lorbacher, K., Sy, A., 1999. Decadal changes in the thermohaline circulation in the North Atlantic. Deep-Sea Research 2 (46), 109–138.

Krauss, W., Fahrbach, E., Aitsam, A., Elken, J., Koske, P., 1987. The North Atlantic Current and its associated eddy field southeast of Flemish Cap. Deep-Sea Research 34 (7), 1163–1185.

Kuhlbrodt, T., Griesel, A., Montoya, M., Levermann, A., Hofmann, M., Rahmstorf, S., 2007. On the driving processes of the Atlantic meridional overturning circulation. Review of Geophysics 45 (2004RG000166), doi:10.1029/2004RG000166.

Kusche, J., 2007. Approximate decorrelation and non-isotropic smoothing of time-variable GRACE-type gravity field models. Journal of Geodesy 81, 733–749.

Lavín, A., Bryden, H., Parrilla, G., 2003. Mechanisms of heat, freshwater, oxygen and nutrient transports and budgets at 24°N in the Subtropical North Atlantic. Deep-Sea Research 1 (50), 1099–1128.

Ledoit, O., Wolf, M., 2004. Honey, I Shrunk the Sample Covariance Matrix. Journal of Portfolio Management 30 (4), 110–119, DOI: 10.3905/jpm.2004.110.

Lemoine, F., Smith, D., Kunz, L., Smith, R., Pavlis, E., Pavlis, N., Klosko, S., Chinn, D., Torrence, M., Williamson, R., Cox, C., Rachlin, K., Wang, Y., Kenyon, S., Salman, R., Trimmer, R., Rapp, R., Nerem, R., 1997. The development of the NASA GSFC and NIMA joint geopotential model. In: Segawa, J., Fujimoto, H., Okubo, S. (Eds.), Gravity, Geoid and Marine Geodesy. Vol. 117. International Association of Geodesy Symposia.

Levitus, S., Antonov, J., Boyer, T., Stephens, C., 2001. World ocean database 1998. National Oceanic and Atmospheric Administration (NOAA), Silver Spring, Md.

Levitus, S., Boyer, T., 1994. World ocean atlas 1994, Volume 4: Temperature. National Ocean and Atmosphere Administration USA, NOAA Atlas NESDIS 4, 117 pp.

Lorbacher, K., Koltermann, K., 2000. Subinertial variability of transport estimates across "48°N" in the North Atlantic. International WOCE Newsletter (40), 3–5.

Losch, M., 2001. Analyse hydrographischer Schnitte mit Satellitenaltimetrie. Ph.D. thesis, Alfred-Wegener-Institut für Polar- und Meeresforschung, Berichte zur Polar- und Meeresforschung.

Losch, M., Redler, R., Schröter, J., 2002a. Estimating a Mean Ocean State from Hydrography and Sea-Surface Height Data with a Non-linear Inverse Section Model: Twin Experiments with a Synthetic Data Set. Journal of Physical Oceanography 32, 2096–2112.

Losch, M., Schröter, J., 2004. Estimating the circulation from hydrography and satellite altimetry in the Southern Ocean: limitations imposed by current geoid models. Deep-Sea Research I 51 (9), 1131–1143.

Losch, M., Sidorenko, D., Beszczynska-Möller, A., 2005. FEMSECT: An inverse section model based on the finite element method. Journal of Geophysical Research 110 (C12023), doi:10.1029/2005JC002910.

Losch, M., Sloyan, B., Schröter, J., Sneeuw, N., 2002b. Box inverse models, altimetry and the geoid: Problems with the omission error. Journal of Geophysical Research 107 (C7), 15–1–15–13.

Lumpkin, R., Speer, K., 2003. Large-Scale Vertical and Horizontal Circulation in the North Atlantic Ocean. Journal of Physical Oceanography 33, 1902–1920.

Lumpkin, R., Speer, K., 2007. Global Ocean Meridional Overturning. Journal of Physical Oceanography 37, 2550–2562.

Lumpkin, R., Speer, K., Koltermann, K., 2008. Transport across 48°N in the Atlantic Ocean. Journal of Physical Oceanography 38, 733–752.

Macdonald, A., 1998. The global ocean circulation: a hydrographic estimate and regional analysis. Progress in Oceanography 41, 281–382.

Macdonald, A., Wunsch, C., 1996. An estimate of global ocean circulation and heat fluxes. Nature 382, 436–439.

Malanotte-Rizzoli, P., Tziperman, E., 1996. The Oceanographic Data Assimilation Problem: Overview, Motivation and Purposes. In: Malanotte-Rizzoli, P. (Ed.), Modern Approaches to Data Assimilation in Ocean Modelling. Elsevier Science.

Mann, C., 1967. The termination of the Gulf Stream and the beginning of the North Atlantic Current. Deep-Sea Research 14, 337–359.

Marshall, J., Plumb, R., 2008. Atmosphere, Ocean, and Climate Dynamics: An Introductory Text. Elsevier.

Maximenko, N., Niiler, P., Rio, M.-H., Melnichenko, O., Centurioni, L., Chambers, D., Zlotnicki, V., Galperin, B., 2009. Mean dynamic topography of the ocean derived from satellite and drifting buoy data using three different techniques. Journal of Atmospheric and Oceanic Technology 26 (9), 1910–1919.

Mayer-Gürr, T., 2007. ITG03s: The latest GRACE gravity field solution computed in Bonn. Joint International GSTM and DFG SPP Symposium, 15 October 2007, Potsdam, http://www.igg.uni-bonn.de/apmg/fileadmin/DatenModelle/media/mayer-guerr_gstm_potsdam_2007.pdf (6 August 2012).

Mayer-Gürr, T., Kurtenbach, E., Eicker, A., 2010. The static solution ITG-Grace2010s. http://www.igg.uni-bonn.de/apmg/index.php?id=itg-grace2010 (6 August 2012).

Mellor, G., Ezer, T., 1991. A Gulf Stream Model and an Altimetry Assimilation Scheme. Journal of Geophysical Research 96 (C5), 8779–8795.

Menemenlis, D., Hill, C., Adcroft, A., Campin, J.-M., Cheng, B., Ciotti, B., Fukumori, I., Heimbach, P., Henze, C., Köhl, A., Lee, T., Stammer, D., Taft, J., Zhang, J., 2005. NASA Supercomputer Improves Prospects for Ocean Climate Research. EOS Trans. AGU 86, 95–96.

Minster, J.-F., 1995. Monitoring of the climate evolution of the ocean and ice sheets using satellite techniques. In: Hempel, G. (Ed.), The Ocean and the Poles. Gustav Fischer Verlag, pp. 59–63.

Msadek, R., Dixon, K., Delworth, T., Hurlin, W., 2010. Assessing the predictability of the Atlantic meridional overturning circulation and associated fingerprints. Geophysical Research Letters 37 (19), l19608, http://dx.doi.org/10.1029/2010GL044517.

Müller, J., Sneeuw, N., Flechtner, F., 2009. Future Satellite Gravity Missions: Activities in Germany. Presentation at the workshop Towards a Roadmap for Future Satellite Gravity Missions, Graz, September 2009, http://www.igcp565.org/workshops/Graz/pdfs/P1_07_Mueller_FutureMissions_Germany_Graz09_f.pdf (6 August 2012).

Munk, W., Palmen, E., 1951. A note on the dynamics of the Antarctic Circumpolar Current. Tellus 3, 53–55.

National Research Council, 1998. Satellite Gravity and the Geosphere: Contributions to the Study of the Solid Earth and Its Fluid Envelope. National Academy Press.

Nechaev, D., Yaremchuk, M., 1995. Application of the adjoint technique to processing of a standard section data set: World Ocean Circulation Experiment section S4 along 67°S in the Pacific Ocean. Journal of Geophysical Research 100 (C1), 865–879.

Nocedal, J., 1980. Updating Quasi-Newton Matrices with Limited Storage. Mathematics of Computation 35 (151), 773–782.

Nocedal, J., Wright, S., 2006. Numerical Optimization, 2nd Edition. Springer series in operations research. Springer.

Nowlin Jr., W., Klinck, J., 1986. The Physics of the Antarctic Circumpolar Current. Reviews of Geophysics 24 (3), 469–491.

Oka, A., Hasumi, H., 2006. Effects of model resolution on salt transport through northern high-latitude passages and Atlantic meridional overturning circulation. Ocean Modelling 13, 126–147.

Oke, P., Brassington, G., Griffin, D., Schiller, A., 2008. The Bluelink ocean data assimilation system (BODAS). Ocean Modelling 21, 46–70.

Olbers, D., 1988. Die Rolle des Ozeans für das Klima. Physik in unserer Zeit, 19. Jahrg. (6), 161–171.

Olbers, D., 1989. A Geometrical Interpretation of Inverse Problems. In: Anderson, D., Willebrand, J. (Eds.), Oceanic Circulation Models: Combining Data and Dynamics. Vol. 284 of NATO ASI Series C: Mathematical and Physical Sciences. Kluwer Academic Publishers, pp. 79–93.

Olbers, D., 1998. Comments on "On the Obscurantist Physics of 'Form Drag' in Theorizing about the Circumpolar Current". Journal of Physical Oceanography 28, 1647–1654.

Orsi, A., Whitworth III, T., Nowlin Jr, W., 1995. On the meridional extent and fronts of the Antarctic Circumpolar Current. Deep-Sea Research I 42 (5), 641–673.

Pail, R., Goiginger, H., Mayrhofer, R., 2010. Goce Gravity Field Model Derived from Orbit and Gradiometry Data Applying the Time-Wise Method. In: Lacoste Francis, H. (Ed.), Proceedings of ESA Living Planet Symposium. SP-686. Held on 28 June - 2 July 2010 at Bergen in Norway.

Parry, M., Canziani, O., Palutikof, J., van der Linden, P., Hanson, C. (Eds.), 2007. Contribution of Working Group II to the Fourth Assessment Report of the Intergovernmental Panel on Climate Change. Cambridge University Press.

Pavlis, N., Holmes, S., Kenyon, S., Factor, J., 2008. An Earth Gravitational Model to Degree 2160: EGM2008. Presented at the General Assembly of the European Geosciences Union, April 13-18 2008, Vienna, Austria.

Pedlosky, J., 1987. Geophysical Fluid Dynamics. Springer-Verlag.

Peng, D., Wu, B., 2009. Precise orbit determination for Jason-1 satellite using onboard GPS data with cm-level accuracy. Chinese Science Bulletin 54, 196–202, doi: 10.1007/s11434-008-0513-0.

Phillips, H., Rintoul, S., 2000. A Mean Synoptic View of the Subantarctic Front South of Australia. Journal of Physical Oceanography 32.

Pinet, P., 1998. Invitation to Oceanography. Jones and Bartlett.

Press, W., Teukolsky, S., Vetterling, W., Flannery, B., 2002. Numerical Recipes in C: The Art of Scientific Computing. Cambridge University Press.

Primeau, F., 2005. Characterizing Transport between the Surface Mixed Layer and the Ocean Interior with a Forward and Adjoint Global Ocean Transport Model. Journal of Physical Oceanography 35, 545–564.

Rahmstorf, S., 2003. The current climate. Nature 421, 699.

Rayner, D., Hirschi, J.-M., Kanzow, T., Johns, W., Wright, P., Frajka-Williams, E., Bryden, H., Meinen, C., Baringer, M., Marotzke, J., Beal, L., Cunningham, S., 2011. Montoring the Atlantic meridional overturning circulation. Deep-Sea Research II 58, 1744–1753.

Reigber, C., et al., 2003. The CHAMP-only Earth Gravity Field Model EIGEN-2. Advances in Space Research 31, 1883–1888.

Richardson, P., 1983. Eddy Kinetic Energy in the North Atlantic From Surface Drifters. Journal of Geophysical Research 88 (C7), 4355–4367.

Richardson, P., 1993. A census of eddies observed in North Atlantic SOFAR float data. Prog. Oceanog. 31, 1–50.

Richter, F., 2010. Nutzung von Argo-Driftern und Satellitenaltimetriedaten zur Ableitung der Zirkulation im Nordatlantik. Ph.D. thesis, Universität Bremen.

Rintoul, S., Bullister, J., 1999. A late winter hydrographic section from Tasmania to Antarctica. Deep-Sea Research I 46, 1417–1454.

Rintoul, S., Hughes, C., Olbers, D., 2001. The Antarctic Circumpolar Current System. In: Siedler, G., Church, J., Gould, J. (Eds.), Ocean Circulation and Climate: Observing and Modelling the Global Ocean. Vol. 77 of International Geophysics Series. Academic Press, pp. 271–302.

Rintoul, S., Sokolov, S., 2001. Baroclinic transport variability of the Antarctic Circumpolar Current south of Australia (WOCE repeat section SR3). Journal of Geophysical Research 106, 2815–2832.

Rintoul, S., Sokolov, S., Church, J., 2002. A 6 year record of baroclinic transport variability of the Antarctic Circumpolar Current at 140°E derived from expendable bathythermograph and altimeter measurements. Journal of Geophysical Research 107 (C10), 19–1–19–22, doi:10.1029/2001JC000787.

Rio, M., Guinehut, S., Larnicol, G., 2011. New CNES-CLS09 global mean dynamic topography computed from the combination of GRACE data, altimetry, and in situ measurements. Journal of Geophysical Research 116 (C07018), doi:10.1029/2010JC006505.

Rio, M.-H., 2010. Absolute Dynamic Topography from Altimetry: Status and Prospects in the Upcoming GOCE Era. In: Barale, V., Gower, J., Alberotanza, L. (Eds.), Oceanography from Space. Springer Science+Business Media B.V.

Rio, M.-H., Hernandez, F., 2004. A mean dynamic topography computed over the world ocean from altimetry, in situ measurements, and a geoid model. Journal of Geophysical Research 109 (C12032), doi:10.1029/2003JC002226.

Robinson, I., 2010. Discovering the Ocean from Space: The Unique Applications of Satellite Oceanography. Springer.

Rummel, R., 2003. How to climb the gravity wall. Space Science Reviews 108, 1–14.

Rummel, R., Gruber, T., 2010. Gravity and Steady-State Ocean Circulation Explorer GOCE. Advanced Technologies in Earth Sciences, Part 3. Springer, pp. 203–212, DOI:10.1007/978-3-642-10228-8_16.

Sabine, C., Feely, R., Gruber, N., Key, R., Lee, K., Bullister, J., Wanninkhof, R., Wong, C., Wallace, D., Tilbrook, B., Millero, F. J., Peng, T.-H., Kozyr, A., Ono, T., Rios, A., 2004. The Oceanic Sink for Anthropogenic CO_2. Science 305, 367–371.

Sato, O., Rossby, T., 2000. Seasonal and Low-Frequency Variability of the Meridional Heat Flux at 36°N in the North Atlantic. Journal of Physical Oceanography 30, 606–621.

Saunders, P., Thompson, S., 1993. Transport, Heat, and Freshwater Fluxes within a Diagnostic Numerical Model (FRAM). Journal of Physical Oceanography 23, 452–464.

Scales, J., Snieder, R., 2000. The anatomy of Inverse Problems. Geophysics 65, 1708–1719.

Schuh, W., Becker, S., 2008. Consistent integration of global gravity field information into Earth process models (INTERMOD). Poster presentation at DFG-SPP 1257 Colloquium "Mass transport and mass distribution in the Earth system", Munich.

Schuh, W., Becker, S., 2010. Potential field and smoothness conditions. In: Contadakis, M., Kaltsikis, C., Spatalas, S., Tokmakidis, K., Tziavos, I. (Eds.), The apple of knowledge - In honour of Prof. N. Arabelos. University of Thessaloniki. AUTH - Faculty of rural and surveying engineering., pp. 237–250.

Shum, C., Plag, H.-P., Bender, P., Braun, A., Cazenave, A., Chamber, D., Emery, W., Fotopoulos, G., Gouretski, V., Gross, R., Miller, L., Hughes, C., Ishii, M., Jayne, S., Kuo, C.-Y., Leuliette, E., Levitus, S., Maximenko, N., Morison, J., Rothacher, M., Rummel, R., Schröter, J., Shibuya, K., Sideris, M., Song, T., Willis, J., Woodworth, P., Zlotnicki, V., 2011. Geodetic observations of the ocean surface topography, geoid, currents, and changes in ocean mass and volume. In: Sustained Ocean Observations and Information for Society. Vol. 2 of Ocean Obs 09. ESA Publication WPP-306, 21-25 September 2009, Venice, Italy, pp. 169–188, `http://bprc.osu.edu/~rashid/publications/Shum%20et%20al.2011.pdf` (6 August 2012).

Sidorenko, D., 2004. The North Atlantic circulation derived from inverse models. Ph.D. thesis, Universität Bremen.

Sloyan, B., Rintoul, S., 2000. Estimates of Area-Averaged Diapycnal Fluxes from Basin-Scale Budgets. Journal of Physical Oceanography 30, 2320–2341, doi: 10.1175/1520-0485(2000)030<2320:EOAADF>2.0.CO;2.

Sloyan, B., Rintoul, S., 2001. The Southern Ocean Limb of the Global Deep Overturning Circulation. Journal of Physical Oceanography 31, 143–173.

Smirnov, O., Anselin, L., 2001. Fast maximum likelihood estimation of very large spatial autoregressive models: a characteristic polynomial approach. Computational Statistics & Data Analysis 35, 301–319.

Sneeuw, N., van Gelderen, M., 1997. The polar gap. In: Sansó, F., Rummel, R. (Eds.), Geodetic Boundary Value Problems in View of the One Centimeter Geoid. Vol. 65 of Lecture Notes in Earth Sciences. Springer Berlin/Heidelberg, pp. 559–568, doi:10.1007/BFb0011717.

Sokolov, S., Rintoul, S., 2002. Structure of Southern Ocean fronts at 140°E. Journal of Marine Systems 37 (1–3), 151–184, doi:10.1016/S0924-7963(02)00200-2.

Stammer, D., Köhl, A., Wunsch, C., 2007. Impact of Accurate Geoid Fields on Estimates of the Ocean Circulation. Journal of Atmospheric and Oceanic Technology 24, 1464–1478.

Stammer, D., Wunsch, C., Giering, R., Eckert, C., Heimbach, P., Marotzke, J., Adcroft, A., Hill, C., Marshall, J., 2002. Global ocean circulation during 1992-1997, estimated from ocean observations and a general circulation model. Journal of Geophysical Research 107 (C9), doi:10.1029/2001JC000888.

Stammer, D., Wunsch, C., Giering, R., Eckert, C., Heimbach, P., Marotzke, J., Adcroft, A., Hill, C., Marshall, J., 2003. Volume, heat, and freshwater transports of the global ocean circulation 1993-2000, estimated from a general circulation model constrained by World Ocean Circulation Experiment (WOCE) data. Journal of Geophysical Research 108 (C1), doi:10.1029/2001JC001115.

Steiger, C., Floberghagen, R., Fehringer, M., 2010. Flight Operations for GOCE, ESA's Gravity Mission. In: Lacoste Francis, H. (Ed.), Proceedings of ESA Living Planet Symposium. SP-686. Held on 28 June - 2 July 2010 at Bergen in Norway.

Steinkamp, O., 2011. Datenanalyse (PHY231). `http://www.physik.uzh.ch/lectures/datenanalyse/11/vorlesung/da11ls.pdf` (6 August 2012), Lecture given Herbstsemester 2011, Universität Zürich.

Stewart, R., 2008. Introduction to Physical Oceanography. Published digitally on `http://oceanworld.tamu.edu/resources/ocng_textbook/PDF_files/book.pdf` (6 August 2012).

Swenson, S., Wahr, J., 2006. Post-processing removal of correlated errors in GRACE data. Geophysical research letters 33 (L08402), doi:10.1029/2005GL025285.

Talley, L., Reid, J., Robbins, P., 2003. Data-Based Meridional Overturning Streamfunctions for the Global Ocean. Journal of Climate 16, 3213–3226.

Tapley, B., Chambers, D., Bettadpur, S., Ries, J., 2003. Large scale ocean circulation from the GRACE GGM01 Geoid. Geophysical Research Letters 30, doi:10.1029/2003GL018622.

Thacker, W., 1989. The Role of the Hessian Matrix in Fitting Models to Measurements. Journal of Geophysical Research 94 (C5), 6177–6196.

Thacker, W., Long, B., 1988. Fitting Dynamics to Data. Journal of Geophysical Research 93 (C2), 1227–1240.

Thorndike, A., Colony, R., 1982. Sea Ice Motion in Response to Geostrophic Winds. Journal of Geophysical Research 87, 5845–5852.

Tomczak, M., Godfrey, S., 1994. Regional Oceanography: An Introduction. Elsevier Science Ltd.

Torge, W., 2003. Geodäsie. de Gruyter.

Treguier, A., Theetten, S., Chassignet, E., Penduff, T., Smith, R., Talley, L., Beismann, J., Böning, C., 2005. The North Atlantic Subpolar Gyre in Four High-Resolution Models. Journal of Physical Oceanography 35, 757–774.

Tziperman, E., Thacker, W., 1989. An Optimal-Control/Adjoint-Equations approach to Studying the Oceanic General Circulation. Journal of Physical Oceanography 19, 1471–1485.

Tziperman, E., Thacker, W., Long, R., Hwang, S.-M., 1992a. Oceanic Data Analysis Using a General Circulation Model. Part I: Simulations. Journal of Physical Oceanography 22, 1434–1457.

Tziperman, E., Thacker, W., Long, R., Hwang, S.-M., Rintoul, S., 1992b. Oceanic Data Analysis Using a General Circulation Model. Part II: A North Atlantic Model. Journal of Physical Oceanography 22, 1458–1485.

Vidard, A., Balmaseda, M., Anderson, D., 2009. Assimilation of Altimeter Data in the ECMWF Ocean Analysis System 3. Monthly Weather Review 137, 1393–1408, DOI: 10.1175/2008MWR2668.1.

Vossepoel, F., 2007. Uncertainties in the mean ocean dynamic topography before the launch of the Gravity Field and Steady-State Ocean Circulation Explorer (GOCE). Journal of Geophysical Research 112 (C05010), doi:10.1029/2006JC003891.

Wahr, J., 1996. Geodesy and Gravity. `http://samizdat.mines.edu/geodesy/geodesy.pdf` (6 August 2012), Class notes, Department of Physics, University of Colorado.

Wahr, J., Swenson, S., Velicogna, I., 2006. Accuracy of GRACE mass estimates. Geophysical Research Letters 33 (L06401), doi:10.1029/2005GL025305.

Wekerle, C., Wang, Q., Schröter, J., Danilov, S., 2011. High resolution sea ice-ocean modeling of the Canadian Arctic Archipelago. Poster presentation at the General Assembly of the European Geosciences Union, April 03-08 2011, Vienna, Austria.

Wenzel, H.-G., 1985. Hochauflösende Kugelfunktionsmodelle für das Gravitationspotential der Erde. Wissenschaftliche Arbeiten der Fachrichtung Vermessungswesen der Universität Hannover 137.

Whitworth, T., Petersen, R., 1985. Volume transport of the Antarctic Circumpolar Current from bottom pressure measurements. Journal of Physical Oceanography 15, 810–816.

Wunsch, C., 1977. Determining the General Circulation of the Oceans: A Preliminary Discussion. Science 196, 871–875.

Wunsch, C., 1978. The North Atlantic General Circulation West of 50°W Determined by Inverse Methods. Review of Geophysics and Space Physics 16 (4), 583–620.

Wunsch, C., 1996. The Ocean Circulation Inverse Problem. Cambridge University Press.

Wunsch, C., 2001. Global Problems and Global Observations. In: Siedler, G., Church, J., Gould, J. (Eds.), Ocean Circulation and Climate: Observing and Modelling the Global Ocean. Vol. 77 of International Geophysics Series. Academic Press, pp. 47–58.

Wunsch, C., 2002. What Is the Thermohaline Circulation? Science 298, 1179–1181.

Wunsch, C., Grant, B., 1982. Towards the general circulation of the North Atlantic ocean. Progress In Oceanography 11, 1–59.

Wunsch, C., Heimbach, P., 2006. Estimated Decadal Changes in the North Atlantic Meridional Overturning Circulation and Heat Flux 1993-2004. Journal of Physical Oceanography 36, 2012–2024.

Wunsch, C., Heimbach, P., 2009. The Global Zonally Integrated Ocean Circulation, 1992-2006: Seasonal and Decadal Variability. Journal of Physical Oceanography 39, 351–368, DOI: 10.1175/2008JPO4012.1.

Wunsch, C., Heimbach, P., Ponte, R., Fukumori, I., the ECCO-GODAE consortium members, 2009. The Global General Circulation of the Ocean estimated by the ECCO-consortium. Oceanography 22 (2), 88–102, NOPP Special Issue »Data/ Information/ Product Development.

Wunsch, C., Stammer, D., 1998. Satellite altimetry, the marine geoid, and the oceanic general circulation. Annual Review of Earth and Planetary Science 26, 219–253.

Yaremchuk, M., Bindoff, N., Schröter, J., Nechaev, D., Rintoul, S., 2001. On the zonal and meridional circulation and ocean transports between Tasmania and Antarctica. Journal of Geophysical Research 106, 2795–2814.

Yaremchuk, M., Nechaev, D., 2001. Simulations of Quasigeostrophic Currents Derived from Satellite Altimetry and Acoustic Tomography of an Open Ocean Region. Journal of Atmospheric and Oceanic Technology 18, 1894–1910.

Danksagung

Zuallererst möchte ich den Urhebern des Projekts “Rifugio”, Herrn Dr. Martin Losch und Herrn Professor Dr. Wolf-Dieter Schuh, danken. Sie haben so die Voraussetzungen für meine Arbeit am Alfred-Wegener-Institut für Polar- und Meeresforschung und für das Entstehen dieser Dissertation geschaffen. Gemeinsam haben wir unermüdlich die Schnittstellen zwischen Ozeanographie und Geodäsie diskutiert. Mein ganz besonderer Dank gebührt hierbei Martin, der für alle Fragen stets ein offenes Ohr hatte, mich in schwierigen Phasen unterstützt und mir viele weise Ratschläge gegeben hat.

Den Gutachtern meiner Arbeit, Herrn Professor Dr. Peter Lemke und Herrn Professor Dr. Thomas Jung, möchte ich sehr herzlich danken, nicht nur für die aufwendige Begutachtung, sondern viel mehr noch für das sorgfältige Korrekturlesen meiner Arbeit. Letztere hat sich hierdurch beträchtlich verbessert und ich konnte sehr viel lernen!

Es gibt unzählige Kollegen am AWI, die meine Zeit hier familiär gestaltet, erleichtert und erheitert haben. Die Mitarbeiter der Graduiertenschule POLMAR haben uns Doktoranden erfolgreich zusammengeführt, weitergebildet, beraten und ermutigt. Meine ehemaligen Kollegen Thomas und Olaf haben immer für gute Laune gesorgt. Silvia hat mir die Anfangszeit erleichtert und in technischen Fragen geholfen, Corinna die mathematischen Verwirrungen diskutiert und Teile der Arbeit Korrektur gelesen. Und all die anderen Ungenannten, die immer für mich da waren oder es noch sind, immer hilfsbereit, immer voller Ideen, ich danke euch!

Many thanks of course also go to Dr Bernadette Sloyan who spent so much time and energy on our teamwork. She not only tought me a lot, but also made me feel even more than welcome in Tasmania, as did Andrew and Scott. Thank you so much, mates!

Und natürlich bedanke ich mich bei all meinen Freunden, die mich trotz der teilweise großen Entfernung nicht vergessen haben. Roman und Steffen danke ich besonders für das schlussendliche Identifizieren so vieler kleiner Fehlerchen. Ein großes Dankeschön auch an meine Freunde in Bremerhaven für die vielen schönen Stunden, die Unterstützung und die Motivation!

Ganz am Ende möchte ich demjenigen danken, der mich ermutigt hat, den Schritt zum AWI nach Bremerhaven zu gehen. Demjenigen, der viel zu viele Bilder nachbearbeitet hat und mit Motivation und Geduld immer zur Stelle war. Micha, ich möchte dir danken für die Leichtigkeit und den Halt, für dein Lachen und diese unglaubliche Selbstverständlichkeit!